UNIVERSITÉ DE STRASBOURG

ÉCOLE DOCTORALE Sciences de la Terre et de l'Environnement

Institut de Physique du Globe de Strasbourg

THÈSE présentée par :

[Jon Alm ERIKSEN]

soutenue le : **7 Septembre 2015**

pour obtenir le grade de : **Docteur de l'université de Strasbourg**

Discipline/Spécialité : **Géophysique**

Morphogénèse dans les fluides granulaires

THÈSE dirigée par :

M. FLEKKØY Eirik	Professeur de l'Université d'Oslo
M. TOUSSAINT Renaud	Directeur de Recherche CNRS, HDR, Université de Strasbourg

RAPPORTEURS :

Mme. BOUCHAUD Elisabeth	Directrice de Recherche CEA, HDR, École Supérieure de Physique et Chimie Industrielles
M. CLAUDIN Philippe	Directeur de Recherche CNRS, HDR, École Supérieure de Physique et Chimie Industrielles

AUTRES MEMBRES DU JURY:

M. EINEVOLL Gaute	Professeur de l'Université d'Oslo

Jon Alm ERIKSEN

Morphogénèse dans les fluides granulaires

Résumé

Cette thèse traite des propriétés de systèmes d'écoulements biphasiques immiscibles en géométrie confinée, en présence de matériaux granulaires immergés. En particulier, elle traite des propriétés des expériences rapportées par B. Sandnes et al., Patterns and flow in frictional fluid dynamics (Nat. Commun, 2, 288, 2011). Le résultat principal est un article qui introduit l'application de ces systèmes à la formation d'intrusions magmatiques. D'autres résultats consistent en deux schémas numériques qui peuvent simuler différents aspects de la dynamique, et en un ensemble de résultats théoriques qui permettent des prédictions quantitatives quand aux modes d'écoulement et de déformation de système bi-fluides/grains.

Résumé en anglais

This thesis is about properties of a two-phase flow system in a confined geometry, containing submerged granular material. In particular, it investigates properties of experiments reported in B. Sandnes et al., Patterns and flow in frictional fluid dynamics (Nat. Commun, 2, 288, 2011). The main result is a paper which introduces the application of these systems to the formation of magmatic intrusions. Other results are two numerical schemes which can be used to simulate different aspects of the dynamics, and a number of theoretical considerations which give quantitative predictions regarding features of the flow behavior.

THESE EN COTUTELLE

présentée pour obtenir le grade de

Docteur de l'Université de Oslo

et de l'Université de Strasbourg

par

Jon Alm Eriksen

Morphogénèse dans les fluides granulaires

Ecole Doctorale: Sciences de la Terre et de l'Evironnement
Spécialité: Géophysique

Rapporteur externe: M. Philippe Claudin, Directeur de Recherche CNRS, HDR, École Supérieure de Physique et Chimie Industrielles
Rapporteur externe: Mme. Elisabeth Bouchaud, Directrice de Recherche CEA, HDR, École Supérieure de Physique et Chimie Industrielles
Examinateur: M. Gaute Einevoll, Professeur de l'Université de Oslo
Directeur de thèse: M. Eirik Flekkøy, Professeur de l'Université d'Oslo
Invité: M. Knut Jørgen Måløy, Professeur de l'Université d'Oslo
Directeur de thèse: M. Renaud Toussaint, Directeur de Recherche CNRS, HDR, Université de Strasbourg

2015

Résumé des contributions scientifiques

Ma thèse débute par une introduction générale de la problématique. Les chapitres suivants correspondent à des articles publiés ou soumis dans des revues internationales de rang A.

Ci-dessous suivent les résumés des articles scientifiques qui constituent cette thèse. Des commentaires sur ma propre participation à ces différents projets sont en italique.

Article 1/ Chapitre 1: Numerical approach to frictional fingers
J.A. Eriksen, R. Toussaint, K.J. Måløy, E.G. Flekkøy, et B. Sandnes,
en cours de review, Phys. Rev. E

Cet article présente une nouvelle stratégie pour simuler des doigts frictionnels dans la dynamique d'interfaces dans des systèmes granulaires/bifluides. Il se fonde sur une approche précédente développée par Henning Knudsen [32], mais surmonte une limitation inhérente en représentant le front granulaire comme un champ de densité en deux dimensions, plutôt que comme une quantité co-mobile avec l'interface. La stratégie de simulation permet de simuler les doigts à un niveau supérieur de fraction solide, ce qui est essentiel pour les simulations présentées dans l'article 2. En outre, le document comprend une description claire et détaillée de la la géométrie de l'état d'équilibre d'un front le long d'un doigt isolé . Bien que cet argument soit parallèle à l'argument présenté dans [32], il contient une correction à l'état stable de la relation entre l'épaisseur du front et la courbure à l'extrémité du doigt. Le document considère comme loi de frottement statique un comportement qui varie linéairement avec l'épaisseur du front, plutôt que la loi de frottement plus compliquée sur la base de l'hypothèse utilisée par Janssen [32]. La loi linéaire peut être considérée comme une linéarisation d'un comportement plus compliqué de la contrainte par rapport à l'épaisseur du front (voir par exemple [3] ou l'article 3), et est validée par la comparaison entre la prédiction théorique de la largeur de doigt et les observations expérimentales, pour les gammes de paramètres qui sont considérées. Cette comparaison permet également la détermination du coefficient linéaire nécessaire dans la loi de frottement.

Je suis le principal contributeur au développement et à la mise en œuvre du schéma numérique, aux arguments théoriques sur l'état d'équilibre et la croissance du doigt et à l'écriture de cet article, tout en bénéficiant des commentaires et corrections des co-auteurs.

Article 2 / Chapitre 2: Model of finger formation at the tip of propagating dykes
J.A. Eriksen, R. Toussaint, K.J. Måløy, E.G. Flekkøy et B. Sandnes,
soumis

Dans cet article, nous présentons des expériences et des simulations de croissance de digitation frictionnelle sous gravité dans une cellule inclinée. Nous élaborons des mesures expérimentales, simulations et théories sur la façon dont ce système explique les motifs qui se émergent naturellement dans les premiers stades de la formation de dykes, lorsque le magma déplace la roche en fusion et accumule des grains de minéraux solides grains à l'interface. Comme l'air est plus léger que le liquide dans les expériences, la gravitation agit pour stabiliser la frontière air-liquide se déplaçant vers le bas, l'air étant au dessus. Les doigts ont tendance à s'aligner et à croître en parallèle, et un diagramme de phase du comportement observé expérimentalement et numériquement est tracé, en fonction de l'angle d'inclinaison et du remplissage solide. Nous identifions une transition d'un alignement vertical vers un alignement horizontal des doigts, à savoir un passage de croissance parallèle à une croissance transversale par rapport à l'écoulement moyen. Nous donnons en outre une argumentation théorique sur la base des variations de la limite plastique du front, ce qui explique qualitativement la transition.

On note que l'argument théorique de la transition du comportement d'alignement repose sur un calcul de la largeur d'un doigt qui dévie de celle utilisée dans le Chapitre 1. Bien que l'argument du Chapitre 1 soit plus détaillée en termes de la géométrie du doigt, les hypothèses sous-jacentes ne sont pas nécessairement valable pour les doigts en compétition dans un champ gravitationnel. L'argumentation présentée ici est plus simple, et ne sert qu'à donner à la largeur du doigt la dépendance fonctionnelle sur la fraction de remplissage. Il est basé sur une hypothèse de minimisation du travail effectué plutôt que sur une croissance du doigt à l'état d'équilibre des forces. Les deux résultats sont en accord en ce qui concerne la forme fonctionnelle de la fraction solide à l'ordre dominant (comparer les équations. 15 et 16 de l'article 1, avec l'Eq. 5 de l'article 2).

Ma principale contribution à cet article est le travail qui sous-tend les simulations, et l'argument théorique qui donne l'explication qualitative pour la transition. Je suis aussi le principal contributeur à la rédaction du document.

Article 3 / Chapitre 3: Bubbles breaking the wall: Two-dimensional stress and stability analysis
J.A. Eriksen, B. Marks, B. et R. Sandnes Toussaint,
Physical Review E 91, 052204 (2015), sélectionné comme "Editor's suggestion"

Cet article propose une extension à deux dimensions du modèle de frottement du front introduit dans [32]. Le modèle étendu comprend les effets des contraintes dirigées tangentiellement par rapport à l'interface, ce qui est nécessaire pour la cohérence logique du cadre théorique, en particulier lorsque l'on décrit les contraintes dans les segments de fronts fortement courbés. Nous discutons les aspects du comportement de frottement qui sont potentiellement importants pour les oscillations en « stick-slip » lors du comportement des bulles (voir le diagramme de phase en Fig. 1.7), en particulier en montrant comment le coefficient de Janssen - qui donne la relation linéaire entre les

contraintes dans la direction normale et tangentielle par rapport à l'interface - peut dépendre de la courbure. Nous soutenons que ces effets sont importants pour les segments de fronts très courbes qui relient les différentes bulles.

Nous décrivons aussi la présence d'ondulations le long de l'interface des bulles en stick-slip. Nous montrons que la longueur caractéristique de ces ondulations est compatible avec les longueurs d'onde les plus instables d'une analyse linéaire de la stabilité du modèle de friction.

L'extension du modèle théorique a été développée par moi-même en étroite collaboration avec Renaud Toussaint. J'ai développé l'analyse de stabilité linéaire, et fut le principal contributeur à l'écriture de cet article.

Chapitre 4 / Article 4: article en cours d'écriture : Phase field approach to viscous fronts

J.A. Eriksen, L. Cueto-Felgueroso and R. Juanes,
Manuscrit non encore soumis

Cet article présente un modèle de champ de phase du front visqueux qui capture la tension de surface effective de l'interface, le comportement visqueux du front et la croissance du front due à l'accumulation de nouveaux grains. Le modèle cherche à décrire les éléments du comportement observé dans les structures en coraux représentées sur le diagramme de phase de la figure 1.7 (front visqueux), où des instabilités de digitation se développent à l'intérieur du front mobile.
Nous présentons également une simulation préliminaire de modèle de champ de phase, qui fournit une démonstration de faisabilité (une validation de concept). Je n'ai malheureusement pas trouvé le temps d'amener les résultats de cet article sous la forme d'un article prêt à être soumis durant le cours de mes recherches. Cependant, la version actuelle de cet article présente un medèle théorique complet des fronts visqueux, et donc un résultat que je souhaite présenter dans cette thèse. Une étude numérique complète des équations du modèle sont laissées pour des travaux futurs.

Le modèle a été développé par moi même, en étroite collaboration avec Luis Cueto-Felgueroso et Ruben Juanes.

Bibliographie

[1] RL Chuoke, P Van Meurs, C van der Poel, et al. The instability of slow immiscible viscous liquid-liquid displacements in permeable media. Petroleum Transactions, 216:188{194, 1959.
[2] Henning Arendt Knudsen, Bj_rnar Sandnes, Eirik Grude Flekkøy, Knut Jørgen Måløy. Granular labyrinth structures in confined geometries. Phys. Rev. E, 77:021301, Feb 2008.
[3] José A. Miranda, Michael Widom. Weakly nonlinear investigation of the Saffman-Taylor problem in a rectangular Hele-Shaw cell. International Journal of Modern Physics B, 12(09): 931-949, 1998.
[4] B. Sandnes, HA Knudsen, KJ Måløy, EG Flekkøy. Labyrinth patterns in confined granular-fluid systems. Phys. Rev. Lett., 99:038001, Jul 2007.

Articles de rang A:

Publiés :
1. B. Sandnes, E.G. Flekkøy, K.J. Måløy and J.A. Eriksen, The shifting shapes of frictional fingers
Rev. Cub. Fis. 29, 1E, (2012).
2. J.A. Eriksen, B. Marks, B. et R. Sandnes Toussaint, Bubbles breaking the wall: Two-dimensional stress and stability analysis, accepté pour publication, Phys. Rev. E (2015).
3. B. Marks, B. Sandnes, G. Dumazer, J.A. Eriksen et K.J. Måløy Compaction of granular material inside confined geometries, accepté à Frontiers in Physics.

Soumis :
4. J.A. Eriksen, R. Toussaint, K.J. Måløy, E.G. Flekkøy, et B. Sandnes, Numerical approach to frictional fingers
en cours de review, Phys. Rev. E.
5. J.A. Eriksen, R. Toussaint, K.J. Måløy, E.G. Flekkøy et B. Sandnes, Model of finger formation at the tip of propagating dykes, soumis à Science.

A soumettre :
6. J.A. Eriksen, L. Cueto-Felgueroso et R. Juanes, Weakly non-linear stability properties of accumulating viscous fronts, à soumettre à Phys. Rev E.

Présentations dans des Conferences Internationales :
1. J.A. Eriksen, B. Sandnes, R. Toussaint, K.J. Måløy and E.G. Flekkøy, Gravity Induced Ordering
of Frictional Fingers (Poster), EGU General Assembly, Vienna, Austria, (2014).
2. J.A. Eriksen, B. Sandnes, L. Cueto-Felgueroso and R. Juanes, Stability of Flow in Dense Suspensions (Poster), AGU Fall Meeting, San Fransisco, USA, (2013).
3. J.A. Eriksen, B. Sandnes, R. Toussaint, K.J. Måløy and E.G. Flekkøy, Numerical Approach to Frictional Fluids (Poster), EGU General Assembly, Vienna, Austria, (2013).
4. J.A. Eriksen, B. Sandnes, K.J. Måløy and E.G. Flekkøy, A Numerical Approach to Stick-Slip Dynamics in Granular Fluids (Talk and Poster), March COMmeeting 12, Havanna, Cuba, (2012).
5. J.A. Eriksen, B. Sandnes, K.J. Måløy and E.G. Flekkøy, A Numerical Approach to Stick-Slip Dynamics in Granular Fluids (Talk and Poster), 2nd International Workshop on Complex Physical Phenomena in Materials, Porto de Galiñhas, Brazil, (2012).

Preface

This thesis is about properties of a two-phase flow system in a confined geometry, containing submerged granular material. In particular, it investigates properties of experiments reported in B. Sandnes et al., *Patterns and flow in frictional fluid dynamics* [1]. The main result is a paper which introduces the application of these systems to the formation of magmatic intrusions. Other results are two numerical schemes which can be used to simulate different aspects of the dynamics, and a number of theoretical considerations which give quantitative predictions regarding features of the flow behavior.

The underlying work was done between 2011 and 2015, at various institutions. Most of the work was done at the AMCS group at the University of Oslo (UiO). I spent the year of 2013 at Juanes Research Group at Massachusetts Institute of Technology (MIT), and ten months of 2014 at the Institut de Physique du Globe de Strasbourg, at Université de Strasbourg (Unistra).

Eirik Grude Flekkøy and Knut Jørgen Måløy were my supervisors at UiO, and Renaud Toussaint was my supervisor at Unistra. Bjørnar Sandnes (Swansea University), Benjy Marks (UiO), Luis Cueto-Felgueroso (MIT) and Ruben Juanes (MIT) have also contributed to various parts of the scientific work.

The research was funded by the Norwegian Research Council through Climit Project No. 200041, with some additional funding from the AMCS group and the Department of Physics at UiO. The time at Unistra was funded by Campus France through the Eiffel Grant.

In addition to the scientific papers which compromise this thesis, I have also contributed to two other papers during my PhD studies. Both these papers discuss aspects of the experimental system in question. First, B. Sandnes et al., *The shifting shapes of frictional fluids* [2], gives a general discussion of the observed flow morphologies in the experimental setup. Second, B. Marks et al., *Compaction of granular material inside confined geometries* [3], discusses micro-mechanic aspects of a jammed plug of beads between two plates. I have, however, chosen not to include these papers, as I want to limit the scope of this thesis to the work in which I have been the main contributor.

The thesis is structured as follows: Chapter 1 provides an introduction to the thesis, in particular to the experimental system in question. Chapter 2 summarizes the scientific papers, and Chapter 3 highlights the main findings. Four scientific papers are included in Chapter 4.

Jon Alm Eriksen, June 2015

Acknowledgements

I have had the pleasure of having Prof. Eirik Flekkøy and Prof. Knut Jørgen Måløy as my supervisors at the University of Oslo, and Dr. Renaud Toussaint as my supervisor at Université de Strasbourg. Their suggestions, advice and efforts to guide me have been indispensable for this thesis. For this I am extremely grateful.

A very special thanks goes to Bjørnar Sandnes who designed and carried out the experiments which this thesis is built upon. This thesis could not have been written without his contributions, generous help and creative ideas.

The numerical method presented in Paper 1 and 2 is by and large a continuation of Henning Arendt Knudsen's previous work. I had the pleasure to discuss with and learn from him, until his unexpected tragic death. I sincerely hope that my contribution adds value to his original ideas.

I would like to thank all my colleagues at the AMCS/PGP group for help on all types of matters and for making a great social environment. In particular, I would like to thank Benjy Marks and Joakim Bergli for scientific discussions and suggestions.

During my PhD studies, I have had the opportunity to spend a year at MIT under the supervision of Prof. Ruben Juanes. I am very thankful for getting this opportunity, and for the fruitful collaboration with Luis Cueto-Felgueroso and Prof. Ruben Juanes. A big thanks to all the people at Juanes Research Group.

Finally, I would like to thank family and friends for backing and encouragement during the last four years. Especially, I would like to thank the two most important persons in the making of this thesis, my better half and language consultant, Nina, and our newborn son, Helmer. I would not have made it without your unconditional love and support. Thank you!

Jon Alm Eriksen, August 2015

Contents

List of papers

Paper 1: Numerical approach to frictional fingers
J.A. Eriksen, R. Toussaint, K.J. Måløy, E.G. Flekkøy, and B. Sandnes,
in review, Phys. Rev. E

Paper 2: Model of finger formation at the tip of propagating dykes
J.A. Eriksen, R. Toussaint, K.J. Måløy, E.G. Flekkøy, and B. Sandnes,
submitted

Paper 3: Bubbles breaking the wall: Two-dimensional stress and stability analysis
J.A. Eriksen, B. Marks, B. Sandnes and R. Toussaint,
Physical Review E 91, 052204 (2015)

Paper 4: Working paper: Phase field approach to viscous fronts
J.A. Eriksen, L. Cueto-Felgueroso and R. Juanes,
unpublished manuscript

Chapter 1

Introduction

A remarkable feature of many non-equilibrium systems, is their tendency to form patterns of regularity. These systems are driven towards an intermediate state, between perfect order and maximal disorder. Classical examples include the nucleation of supercooled droplets in clouds, which results in the intricate symmetrical shapes of snowflakes, and constantly replicating biological matter, which by the wonders of evolution, can form regular stripes on the back of a zebra. The patterns can manifest themselves in a multitude of different ways. Some patterns develop at a scale which is much bigger than the size of its individual components. A Tsunami wave can extend for thousands of kilometers, while its constituents–the water molecules–have an approximate diameter of a couple of Ångströms (a scale ratio of 10^{16}!). Yet, other patterns form without any definite scale, like the dendritic shape of river networks and the self-similar structures of lightning paths and mountain range profiles. Patterns in nature are abundant; they are wherever you look.

The pattern geometry and dynamics can often be described by mathematics. This may be done either by analytic means, or by numerical schemes if the equations are too intricate. By properly accounting for the relevant underlying physical mechanisms, we can make quantitative predictions about the emerging structures. Sometimes, the pattern forming process ceases to evolve, and the intermediate pattern geometry freezes in time. The mathematical models can be used to infer what physical mechanisms caused the frozen pattern to form, and thereby give a glimpse of a distant past. For example, a smooth wavy texture on a rock face found in the desert, can indicate the previous presence of flowing water.

Granular material are prone to form patterns, as exemplified by ripples on the beach and sand dunes. A reason for this is that the grains are too large to respond to thermal agitation. Frictional forces in a pile of grains prevent the packing configuration from reaching an energetic ground state; the packing can remain static in a large variety of meta-stable states.

This thesis explores patterns which can form in confined systems where grains are displaced by a fluid interface. As an immiscible fluid invades the system, the interface which separated the phases, is able to bulldoze a layer of beads which are submerged in the defending fluid. The interplay between the capillary forces of the interface, and the frictional forces of the compacted beads will result in a number of qualitatively different patterns, some of which share a

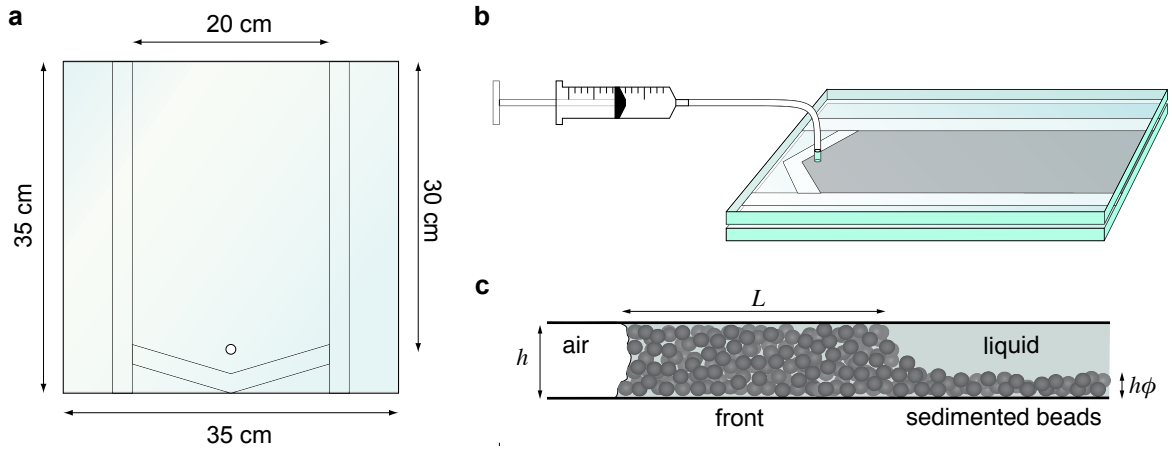

Figure 1.1: Schematic illustration of a rectangular Hele-Shaw cell setup. (a) Top view of the cell, illustrating the relevant dimensions. (b) Air is injected through an injection point at the short end of the cell at constant rate (q) by means of a syringe pump. The opposite end is open to the atmosphere. (c) Up-close view of a cross section of the cell at the air/liquid interface. The cell is initially filled with a layer of beads submerged in a viscous liquid. The height of the initial layer, relative to the cell gap (h) is denoted by ϕ. The cell gap is fixed at $h = 0.05$ cm, and the beads have an average diameter of $\simeq 100$ μm. The invading interface bulldozes up a region of packed grains in the gap between the plates. This packed region is referred to as the *front* and is characterized by a thickness L.

remarkable similarity with patterns found in geological settings. We seek to understand how these patterns come about. To this end, we will model the pattern behavior and characterize its features, in the scientific papers which compromise this thesis.

1.1 Quasi two-dimensional flow

The main scientific contribution presented in this thesis is in the form of theoretical considerations and numerical simulations, and not in the form of experimental results. Nevertheless, the common thread is patterns which do occur in a specific experimental setup. We will therefore spend some time explaining the historical development and the details of these experiments.

The Hele-Shaw cell, named in honor of Henry Selby Hele-Shaw (1854–1941), is an experimental setup for studying quasi two-dimensional fluid flow. It consists of two parallel glass plates, separated by a small distance (h), which confine the fluid. The transparency of the glass plates makes the cell an ideal setup for visualizing different flow phenomena. The cell is typically either rectangular or circular; an example of a rectangular cell with an injection point at the side is shown in Figs. 1.1a and 1.1b. When a liquid is flowing between the plates at a given average velocity, the Reynolds number which characterizes the flow[1] scales with the plate separation. The flow becomes creeping in the limit of small Reynolds number. In this limit, we can ne-

[1]The Reynolds number Re is defined to be the ratio between inertial and viscous forces in a flow system, $\mathrm{Re} = \rho V^2 L^2/(\mu V L) = \rho V L/\mu$, where V is the characteristic velocity, L is the characteristic linear size of the system, μ is the viscosity and ρ the density. Using these quantities, we can express the Navier-Stokes equation for

glect the non-linear advection term, and the time derivative in the Navier-Stokes equation. The governing simplified equation–the Stokes equation–is linear, and much simpler to handle. The flow in the Hele-Shaw cell can therefore be made creeping by choosing a sufficiently small cell spacing. Moreover, if we consider the height averaged velocity U of an incompressible fluid, the governing equations take a particularly simple form,

$$U = -\frac{h^2}{12\mu}\left(\nabla p - \rho \boldsymbol{g}\right), \tag{1.2}$$

$$0 = \nabla \cdot U, \tag{1.3}$$

where μ is the viscosity, p is the pressure, ρ is the density and $\boldsymbol{g}$ the gravitational acceleration vector. When the cell is placed in the horizontal plane we can neglect the $\rho \boldsymbol{g}$ term in Eq. (1.2). If we interpret U as a fluid discharge per unit area, and $h^2/12$ as the permeability of the cell, Eq. (1.2) is of the same form as Henry Darcy's phenomenological equation for describing flow in a porous media [4], and for that reason Eq. (1.2) is often referred to simply as Darcy's equation.

There is a long history of experiments done with this setup, following Hele-Shaw's own seminal work [5, 6]. A particularly interesting flow phenomena was investigated by Philip Geoffrey Saffman and Sir Geoffrey Ingram Taylor (1958). They studied how immiscible fluids–i.e. fluids that do not mix–behave in the cell. They identified an interfacial instability, the Saffman-Taylor instability, which occurs when one fluid displaces the other [7], such that the displacing–or invading–fluid has a lower viscosity than the displaced–or defending–fluid. In that case, the fluid interface becomes unstable, and the displacing fluid develops finger structures which penetrate into the high viscosity fluid. The fingers are often referred to as viscous fingers. The underlying instability has fostered an extensive literature of research papers; review papers can be found in Refs. [8, 9, 10, 11].

The Hele-Shaw cell has also proven to be an excellent setup for studying relevant aspects of flow behavior in porous media. If the Hele-Shaw cell is packed with beads, such that the beads are unable to move in between the plates, the cell becomes a model system of a porous medium. We will in the following discuss systems where the defending fluid are wetting the beads and the glass plates. Flow phenomena under these circumstances are referred to as *drainage*, as opposed to *imbibition* where the adhesive forces act to spread out the invading fluid onto the beads, i.e. the invading fluid is wetting the beads and the glass plates. The presence of beads during drainage modifies the viscous fingering behavior dramatically; the interface of the fingers turn out to have fractal properties[2] [15, 16, 17]. Moreover, the modification of the setup sets

an incompressible fluid in a non-dimensional form,

$$\mathrm{Re}\left[\frac{\partial u}{\partial t} + (u \cdot \nabla)u\right] = -\nabla p + \nabla^2 u, \quad \nabla \cdot u = 0, \tag{1.1}$$

where the pressure p is expressed in units of $\mu V/L$. Note that the second term on the left hand side is non-linear, and makes the equations very hard to solve in general. This term is referred to as the advection term.

[2]The interface of a viscous finger in a cell without beads can also develop fractal structures [12, 13, 14], but

the stage for a new two-phase flow phenomenon of flow dominated by capillary forces. If the invading fluid is injected slowly, the viscous forces can be neglected. The dynamics of the invasion are determined by the wetting properties of the beads, and the surface stresses at the air/liquid menisci in the void space between the beads. The resulting structures–the capillary fingers–have no well defined tip nor sense of direction. The invading flow follows the path of least resistance in terms of capillary forces and percolates through the porous matrix. The resulting patterns consist of connected clusters of the invading fluid and trapped pockets of the defending fluid [18, 19]. The evolving pattern can be stabilized [20] or destabilized [21] by gravity, depending on the density difference of the different fluids and the tilting angle of the Hele-Shaw cell. If we reduce the packing fraction of beads, and allow the beads to rearrange during the experiment, yet new phenomena are observed, for example fracturing in the granular matrix [1, 22, 23, 24, 25], fingers which develop as the grains are compacted [26] or decompacted [27, 28] and destabilized viscous fingers in suspensions with density matched beads [29, 30].

This line of research has motivated further studies of flow phenomena at low bead packing fraction. This would be systems where the displaced fluid contains mobile beads. Another motivation for considering this setup is the application of flow in sheet-like confinement in geological settings. Geological formations are often fractured; granular material and other heterogeneities are likely to be present in the crack openings. The flows of oil, groundwater, injected CO_2 and magma tend to concentrate in these confined spaces, as they have a much higher permeability than the surrounding host rock. The understanding of the flow in these systems have obvious industrial applications as well as academic interests. We will see below that the presence of heterogeneities in a Hele-Shaw cell, in the form of mobile granular particles, can have a profound impact on the flow properties. An application of this system to the formation of magmatic intrusions in fractures, is also presented later in this thesis (Paper 2).

1.2 Frictional fingers enter the stage

We will in the rest of this thesis focus on liquid mixtures containing wetting beads which are denser than the liquid, such that the beads make up a layer of sedimented–but mobile–beads at the bottom plate of the Hele-Shaw cell, as shown in Fig. 1.1c. This system was first studied by Bjørnar Sandnes, Henning Knudsen, Knut Jørgen Måløy and Eirik Flekkøy [31, 32]. The study revealed the development of granular labyrinth patterns which are shown in Figs. 1.2 and 1.3. The experimental setup they used deviates slightly from the one presented in Figs. 1.1a and 1.1b. Their cell was circular rather than rectangular, and the liquid was drained out of a central outlet point. The emerging structures are similar regardless of these differences.

The rate at which the liquid is drained is very low ($q = 0.01$ ml/min), and each experiment may last more than a day. The height of the initial layer of sedimented beads, relative to the cell gap will in the following be denoted by ϕ and referred to as the (normalized) filling fraction of

to the best of the author's knowledge, this has only been observed with carefully selected non-Newtonian fluids, i.e. fluids where the viscosity is a varying parameter.

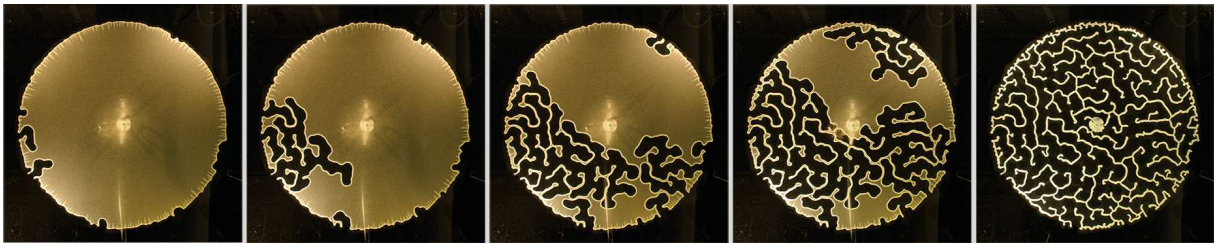

Figure 1.2: Time sequence of the evolution of the frictional fingers in a circular Hele-Shaw cell. The cell is drained from a central outlet, and air is invading from the sides. The cell is imaged on a black background, and the black structures are identified as the invading air. The dimensions of each picture frame are 40×40 cm, and the cell spacing is 0.4 mm. The figure is taken from Ref. [31].

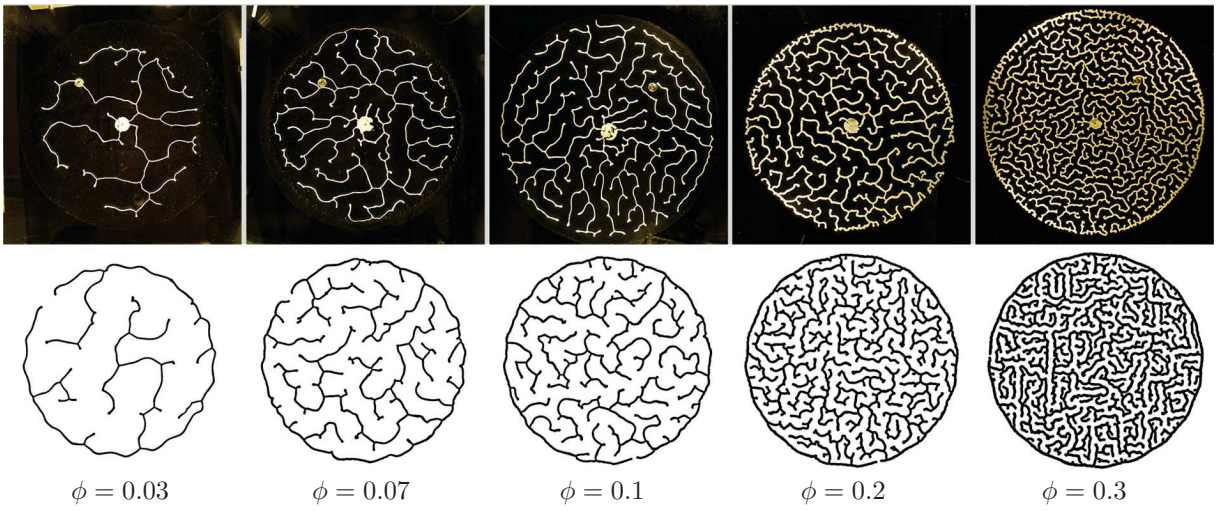

Figure 1.3: The fully developed labyrinth patterns of the evolution shown in Fig. 1.2, for different values of the initial filling fraction ϕ. The top row shows experimental results, which are compared to the simulations in the bottom row. The white regions of the simulations represent the air. The simulations reproduce the structures, in particular the reduced characteristic finger width for increasing values of ϕ. All experiments were conducted with a plate spacing of 0.4 mm. The figure was originally presented in Ref. [31].

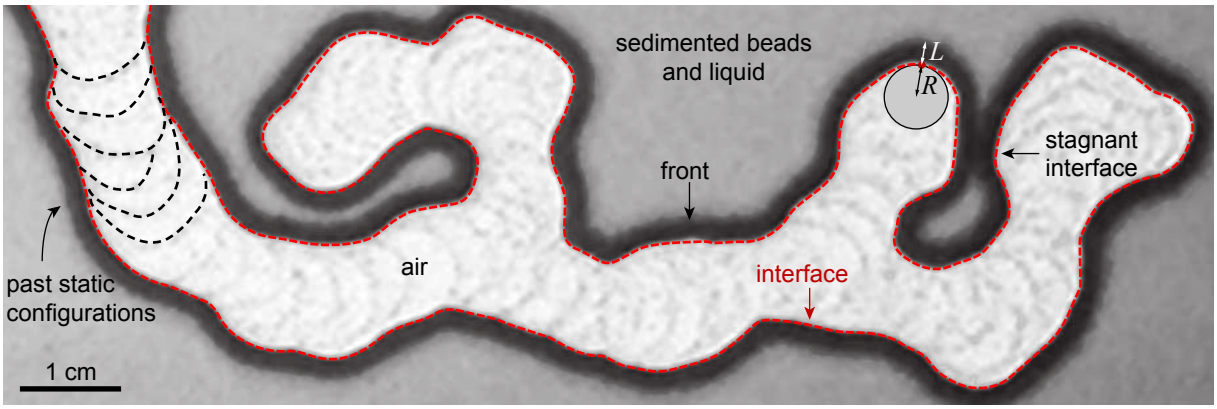

Figure 1.4: Close up image of a branching frictional finger which grows in the experimental setup shown in Fig. 1.1, as seen from the top of the cell. The red dashed line follows the air/liquid interface. Along this line we can identify a curvature, $\kappa = 1/R$, where R is the radius of curvature. The curvature (κ) takes negative values if the radius can be drawn towards the liquid phase. We can also identify a front thickness (L) along the interface, except where the interface is stagnant. The interface leaves a tiny layer of beads behind after each incremental displacement. These layers are seen as dark regions in the air phase, some of which are indicated by black dashed lines. The contrast within the air phase has been artificially enhanced to show these structures. The frictional fingers are similar to the fingers seen in the labyrinth structures (Fig. 1.2), but are here imaged with a white background.

the cell[3]. As air enters from the outer rim of the cell, the air/liquid interface bulldozes up the sedimented beads and forms an accumulated compacted layer of beads adjacent to the interface. This layer will in the following be referred to as the *front*, and it will be characterized by a thickness (L). The cross section shown in Fig. 1.1c illustrates this front as seen from the side. We can also characterize the air/liquid interface by an effective in-plane curvature (κ) averaged over a number of menisci along the interface. This curvature describes the large scale geometry, as the interface appears visually in Figs. 1.2 and 1.3. As the interface evolves, finger structures develop. These structures are labeled *frictional fingers* and depend on the static frictional forces in the front and the effective large scale surface forces, rather than the viscous forces of the displaced liquid or the capillary forces between the beads. The nature of these mechanisms will be described in the following paragraphs. An example of a frictional finger, as it grows in the experimental setup of Fig. 1.1, is shown in Fig. 1.4. When a finger moves towards the interface of a different section along the finger structures, the fronts combine into a stagnant region of beads, as illustrated in Fig. 1.4. As the cell is drained, neighboring fingers grow closer, and a larger fraction of the interface becomes stagnant. When the cell is fully drained, the stagnant residual front forms a pattern of labyrinth structures in the cell.

The dynamics of the system consist of incremental stick-slip displacements which are confined to small sections of the interface. The motion is always directed towards the liquid phase and

[3]Note that ϕ is also commonly used to denote the packing fraction of a granular material, which might cause some confusion. We will neglect variations in the packing fraction throughout this thesis; we assume that both the sedimented layer, and the front, have a constant packing fraction probably close to that of a poured random packing $\simeq 0.6$. This is verified in [3]. We will consistently use ϕ as the initial normalized filling fraction. If the cell is completely filled with beads, we have $\phi = 1$, and if the sedimented layer fills half the cell gap, we have $\phi = 0.5$, while the packing fraction takes a value close to 0.6 in both cases.

a moving section of the interface continues its motion over many consecutive stick-slip events, before it eventually stops and the motion continues at another section. When the whole interface remains static, the pressure drop over the menisci between the beads at the interface, i.e. the capillary pressure (Δp) is increasing steadily as the liquid is drained from the cell. The increasing capillary pressure is balanced by the frictional stresses in the bead packing of the front. We can assign a yield threshold to every section of the interface, above which a local section of the interface yields and moves an infinitesimal amount towards the liquid phase. This threshold is the sum of the yield stress of the bead packing, σ_Y, and the effective surface tension of the large scale features of the interface, $\gamma\kappa$, where γ is the effective surface tension, i.e.

$$\Delta p > \gamma\kappa + \sigma_Y . \tag{1.4}$$

As the interface slips, the capillary pressure decreases, and the motion stops after a tiny displacement. New beads are accumulated onto the front during the displacement; the front thickness changes by a combination of stretching of the interface and the accumulation of new beads. The deformation of the front and the interface, alters the local yield stress which may change the location of the next moving section.

We will elaborate on both terms on the right hand side of Eq. (1.4) in subsection 1.4. For now, we will simply note that the right hand side varies locally along the interface, whereas the left hand side is a global quantity. This means that we can identify the next moving section of the interface as the section which has local properties which minimize the right hand side. This is the basic principle that the simulations in Fig. 1.3 are based on. The frictional fingers grow with a characteristic width, as clearly seen in Fig. 1.4, which depends on the initial filling fraction of beads (ϕ), as shown in Fig. 1.3. The characteristic width can be understood by analyzing the interplay between σ_Y and $\gamma\kappa$ [32]. The effective surface tension acts to widen the curved finger tip, while the static friction opposes wide fingers since they accumulate a thicker granular front. The characteristic width represents a balance between these two opposing effects. The presence of a characteristic width, which is independent of the system size, is distinct from the usual behavior of viscous fingers. The Saffman-Taylor instability in a rectangular Hele-Shaw cell develops a steady-state finger with a width which depends on the width of the cell [7]. In a porous matrix, viscous fingers are known to be fractal, and hence without any characteristic size [15, 16].

1.3 A plethora of flow morphologies

The surprising structures revealed in the labyrinth experiment was only the tip of an iceberg in terms of unexpected intriguing flow morphologies. Bjørnar Sandnes continued the experimental study of the system in the setup shown in Fig. 1.1. As already discussed, the capillary pressure over a configuration of beads at an air/liquid interface similar to the one shown in Fig. 1.1c, can be increased either by decreasing the water pressure or by increasing the air pressure. This

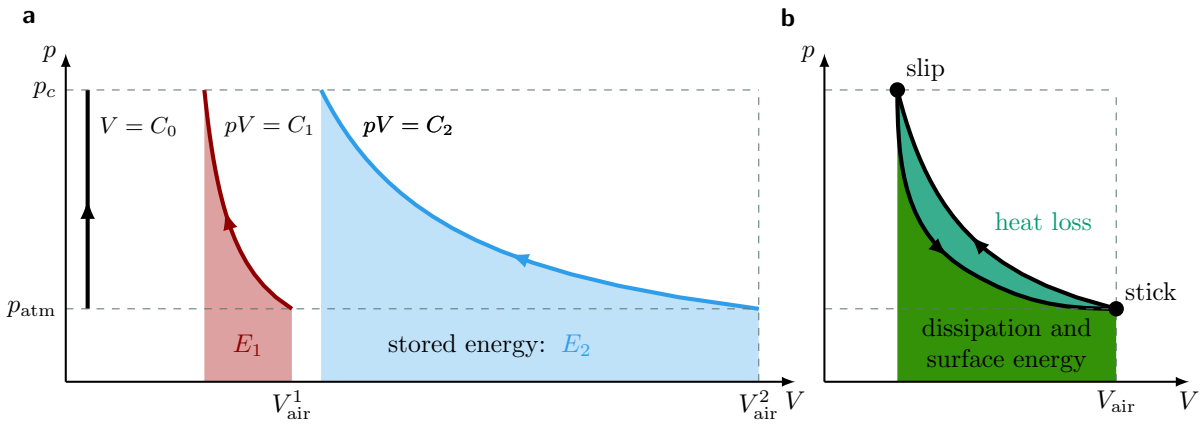

Figure 1.5: (a) A pV-diagram showing the isothermal compression paths of a gas starting at atmospheric pressure p_{atm} and volume V_{air}, and ending at a critical pressure p_c. The path is drawn for two initial values of the air volume, V^1_{air} in red and V^2_{air} in blue. The black path shows the analogous path for an incompressible fluid, following $V =$ constant. The free energy (Hermholtz) stored in the process, for each example, is indicated as the area under the path. (b) A schematic idealization of the stick-slip cycle in a pV-diagram. During the pressure build up, the path is following an isotherm. Directly after the slip, the volume is quickly expanding such that we can neglect the heat exchange with the environment. The path is therefore initially approximated by an adiabatic process, i.e. taking a steeper path than the isotherm. The area enclosed by the full cycle corresponds to the heat loss in the syringe. The area under the path, which follows the slip event, corresponds to the energy dissipated in the bead packing and the surface energy needed to deform the interface.

can be done by the drainage of the liquid or by air injection into the cell, respectively. The new experiments were carried out by the latter approach.

There is a subtle difference between the two procedures. Consider the compression of air in a syringe pump connected to the air phase in the cell as shown in Fig. 1.1b, when the interface remains stagnant. Let the air pressure be denoted by p, and the total air volume–in the cell and in the pump–by V. We will assume that the compression rate (q) is small, such that the air pressure will increase along an isotherm, i.e, along lines where $pV =$ constant, as shown in Fig. 1.5a. The pressure will increase until it reaches the critical threshold p_c, above which the weakest section of interface yields and moves towards the liquid phase. The critical pressure corresponds to the capillary pressure, $\Delta p = p_c - p_{liquid}$, when Eq. (1.4) is evaluated at equality for the weakest section of the interface. The free energy (Hermholtz), which is stored in the air phase as it is compressed, is increasing with the initial amount of air in the syringe pump. On the other hand, the equation of state of an incompressible fluid is essentially, $V =$ constant. No free energy can be stored by the expansion of the liquid phase during drainage, simply because the liquid does not expand. The injection of air, by the compression of a connected air reservoir, thereby allow us to control the free energy of the slip events.

For each slip event, the stored energy in the syringe pump is transformed into a combination of heat loss in the syringe, dissipation of energy in the deforming packing of beads and the surface energy due to the deformation of the interface, as indicated in Fig 1.5b. A larger amount of stored energy amplifies the stick-slip behavior of the frictional fingers. When we further

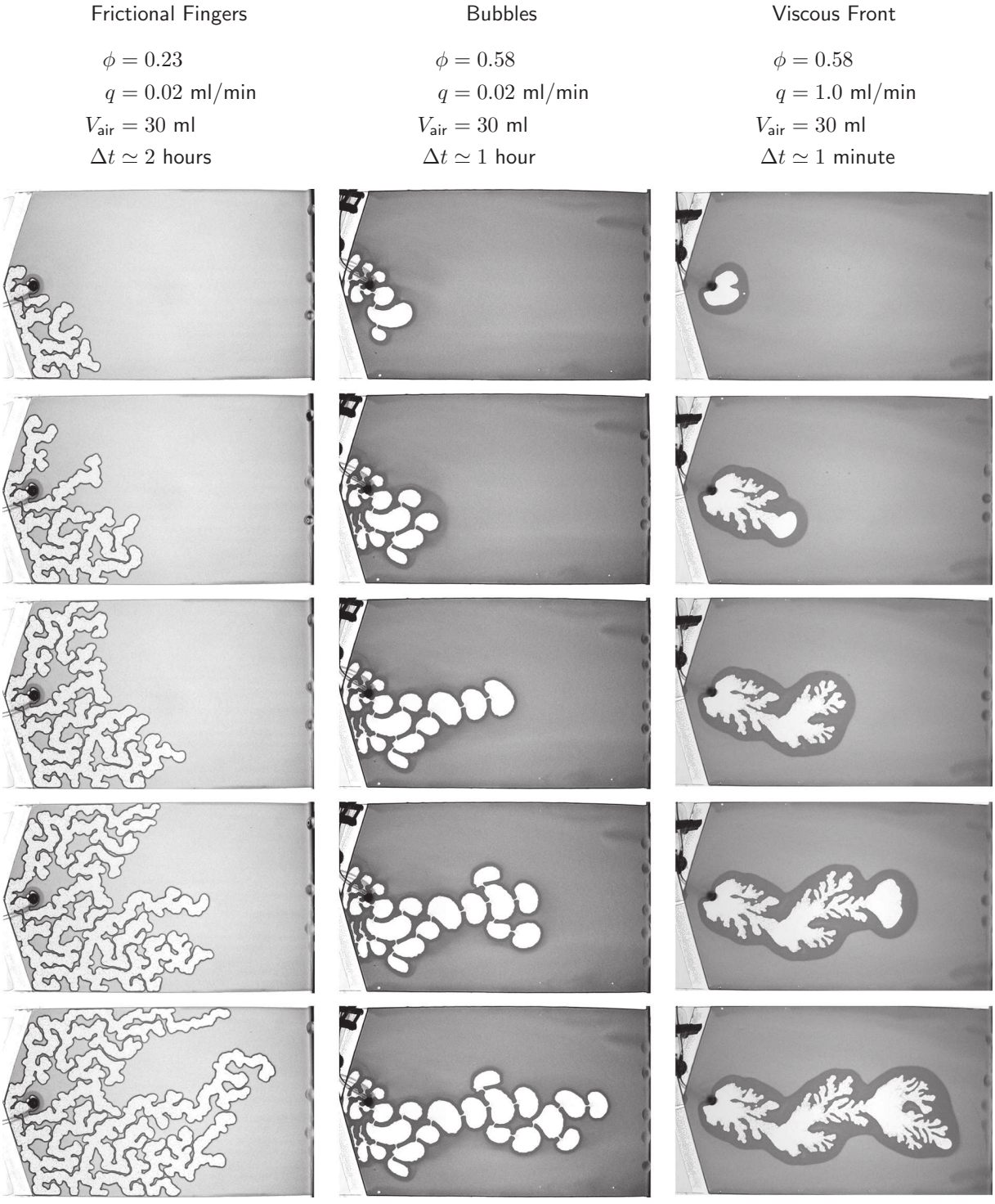

Figure 1.6: Each column shows a time series for a different mode of dynamics seen in the experimental setup shown in Fig. 1.1. The time step Δt indicates the time interval between each frame. The dynamical modes were originally introduced in Ref. [1].

increase the stored energy in the syringe, by either increasing the initial packing fraction of beads, which leads to a larger p_c, or the air volume in the syringe, we observe transition between the finger behavior to a bubble type of dynamics, where each bubble corresponds to a single slip event. The remaining pattern consists of a series of bubbles connected by thin channels of air. Time series of experiments showing both frictional fingers and the bubble behavior is shown in Fig. 1.6. The phase transition between the two modes of dynamics in the ϕV_{air}-plane, is described in [1].

By increasing the compression rate (q), it is possible to prevent the whole interface from sticking, such that a large but confined section of the front is mobilized and evolves at all times. In this mode of dynamics, the moving front behaves effectively as a dense suspension with a high viscosity, as the presence of beads increases the energy dissipation in the flowing liquid. The high viscosity contrast between the air and the fluidised front allows for viscous fingers of air to penetrate into the front. These structures are eventually frozen in the cell, when the front stagnates locally and enters a sticking state. Oscillations in the air pressure results in alternations in the branching behavior of the fingers. The process creates beautiful structures which almost resembles corals, or some type of under water plant organism, where each branch is a frozen viscous finger. A time series of the dynamics is also shown in Fig. 1.6.

The phase diagram shown in Fig. 1.7, illustrates where these structures fit into a larger landscape of dynamical modes in the ϕq-plane. The phase boundaries are, however, only intended to be 'guides to the eye'; further investigations may reveal more structures. As an example of other types of structures which can emerge in a similar experimental setup, consider the time series presented in Fig. 1.8. This pattern is made with a bead mixture of many different sizes, which apparently prevent the front from jamming. All the fingers in the periphery of the compact pattern are moving simultaneously, and each finger seems to undergo tip splitting at regular intervals. A finger will only stop its motion if it stagnates towards a neighboring finger. This experiment displays a dynamics which is somewhat similar to the behavior seen in the fluidised front, and develops also an organic looking pattern. This intriguing behavior further motivates the study of the dynamics of viscous fronts, which will be discussed further in Paper 4.

1.4 The focus of this thesis: Action at the front

This thesis is focused on expanding the understanding of the three flow morphologies shown in Fig. 1.6. Namely, the frictional fingers, the bubbles and the viscous front. The physics underlying these patterning processes is largely confined to the front; the most important effects can be identified as:

- The effective surface tension
- The friction properties of the front, either static or viscous
- The accumulation of new beads to the front

These effects deserve some more elaboration.

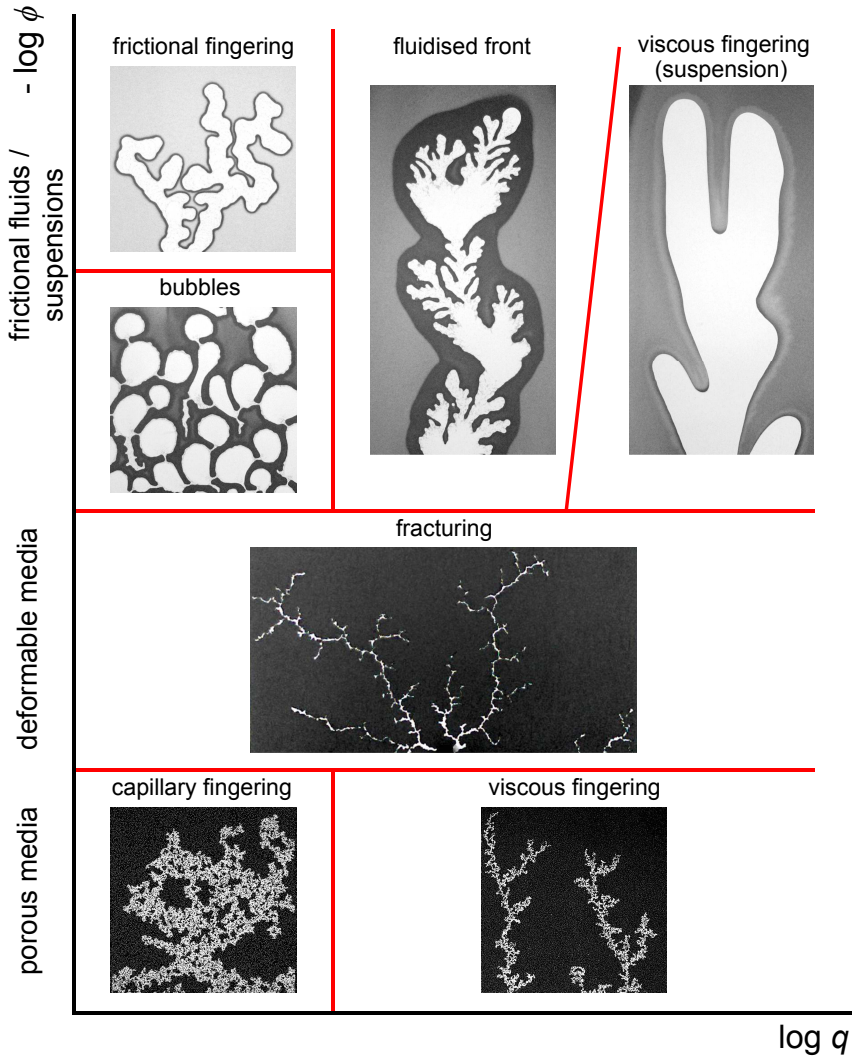

Figure 1.7: Tentative phase diagram of morphologies for varying filling fractions (ϕ) and injection rates (q). Fracturing occurs at $\phi > 0.9$. The bottom of the y-axis, where $-\log\phi$ takes its lowest value, corresponds to a close-packed porous medium, i.e. $\phi \simeq 1$. The scientific contribution of this thesis focuses on the upper left section of this diagram, i.e. frictional fingers, bubbles and viscous fronts. The phase diagram is presented and further discussed in Refs. [1, 2]. The picture of the capillary fingers, and the viscous fingers in the porous medium, is taken from previous work done at the AMCS group at UiO [19, 33].

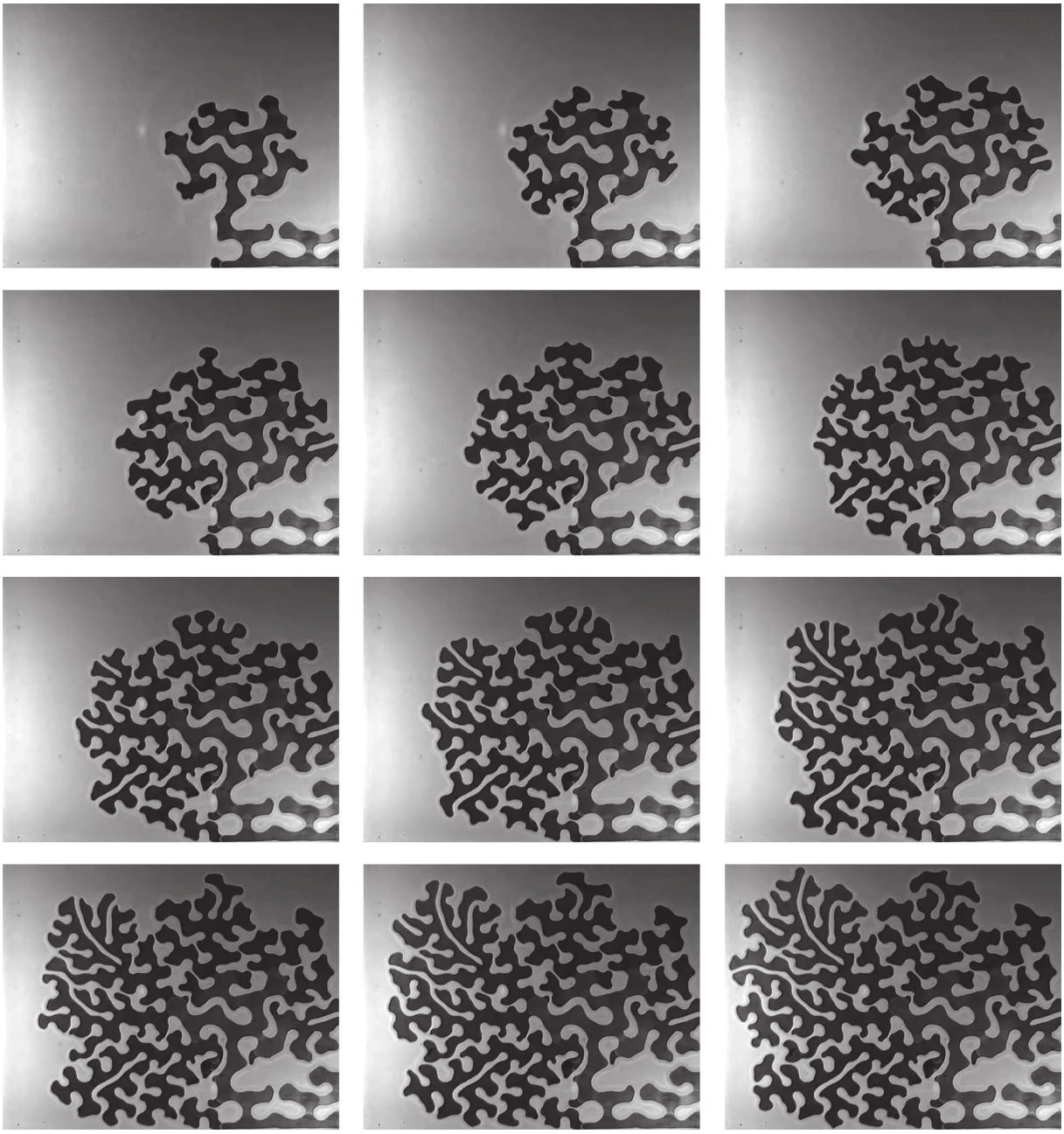

Figure 1.8: Time series of a previous unpublished experiment done by Bjørnar Sandnes in the experimental setup shown in Fig. 1.1. The cell is imaged on a black background; the black fingers correspond to air. There is a thin front along the air interface, which is hard to identify in the frames. The cell is initially filled with a mixture of beads of various sizes. The air injection rate is $q = 0.81$ ml/min. The fingers grow simultaneously, and the beads in the front do not jam. The height of each frame is 17 cm. The whole time series lasted approximately 10 minutes.

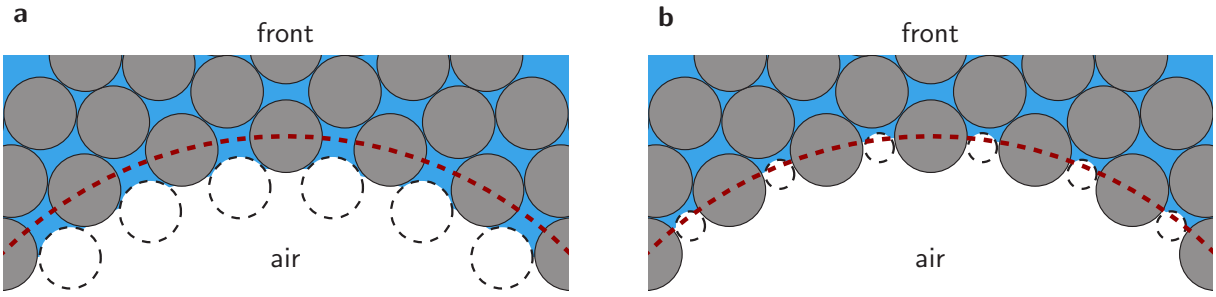

Figure 1.9: Schematic close up of the interface. The red dashed circle section indicates the average position of the interface; its radius corresponds to the reciprocal of the average curvature (κ). The air/liquid interface consists of menisci between the wetting beads, indicated by the black dashed circles. The capillary pressure (Δp) is proportional to the curvature of the menisci (i.e. inversely proportional to the radii of the black dashed circles), and independent of the large scale curvature. (a) Low capillary pressure, the radius of curvature of the menisci are relatively large. (b) High capillary pressure, the menisci are forced into the bead packing. The contact angle between the fluid and the beads is assumed to be negligible in both (a) and (b). The relative length scales between the radii of curvature and the bead diameters in the figure are enhanced for illustrative purposes.

First, the surface tension at the interface acts at two different scales. At the small scale, the interface makes bridges between wetting beads. Each point on a meniscus can be characterized by two principal radii of curvature. By the Young–Laplace equation, the pressure drop over a meniscus is proportional to the mean of the principal curvatures. This means that in a static configuration, each menisci has the exact same mean curvature, up to differences in the hydrostatic liquid potential, which we can ignore in a horizontally oriented cell. In the two-dimensional schematic illustration of the interface, as shown in Fig. 1.9, this means that each menisci has the same radius of curvature. For a frictional finger, there is no difference between the mean curvature of a meniscus at the finger tip, and a meniscus along the finger side.

At a larger scale, we can identify a curvature which is averaged over several neighboring beads. For our Hele-Shaw setup, the principle directions of the average curvature are the in-plane and the out-of-plane directions with respect to the cell plane. We will disregard the curvature component in the out-of-plane direction of the cell, i.e. the curvature of the interface as it is illustrated in the cross section in Fig. 1.1b. The surface stresses related to this component are constant along the in-plane direction of the interface, and does, at our level of description, only contribute to a constant global pressure drop.

The averaged, in-plane, curvature of the interface will be denoted by κ and appears to us as the apparent curvature of the air interface in the top view of the cell. When we average over many neighboring beads, we can also identify an average air/liquid surface area. This area scales with the number of menisci, and therefore linearly with the apparent area of the interface, i.e. apparent in the sense that we ignore the convoluted nature of the small scale menisci. Fluctuations in the capillary pressure may modify the the total area, as the total geometry of the menisci depend on the capillary pressure; compare the air/liquid interface in Fig. 1.9a and 1.9b. The changes in the surface area induced by an increasing capillary pressure, may, however, increase or decrease depending on the bead/liquid contact angle and the distance between neighboring

beads. The total change in area is, therefore, likely to be a sum of many small positive and negative contributions, and the net effect is assumed to be negligible. We will throughout this thesis ignore these variations, and assume that an average surface energy which scales with the apparent surface area, is an appropriate description of the interface.

The presence of an average surface energy can be characterized by an effective surface tension γ [32]. The effective tension acts against the increase of the apparent interface area, during the displacement process. This effect is incorporated in our model of the finger dynamics by including the effective pressure difference, $\gamma\kappa$, to the criteria for the yield pressure, which explains why we included the effective surface tension in Eq. (1.4).

Second, when we described the yield capillary threshold, for a static front configuration in Eq. (1.4), we also included the frictional properties of the front in terms of the bead stress σ_Y. To be precises, this is the yield treshold of the effective bead stress, acting normal to the plane which approximate the air/liquid interface. This quantity was, in the previous work of Henning Knudsen et al. [32], assumed to be an exponentially increasing function of the front thickness. This was justified by considering a model for stesses in packings of grains, namely the Janssen model which assumes a linear relationship between the principal stresses in the packing, in conjunction with the static Coloumb frictional stresses at the plate boundaries of the cell. In the following, we will describe this yield stress, σ_Y, in various levels of details, taking into account the local parameters such as L and κ, the effects of tangential stresses (Paper 3).

When a section of the front is mobilized, we will either assume that the interface moves an infinitesimal distance, in the case of the frictional fingers, or, in the case of the viscous front, assign an effective viscosity to the front, and thereby approximate the frictional behavior as a Newtonian fluid.

Third, the front accumulates new beads as the air phase displace the liquid. To illustrate the accumulation, consider a flat interface, with an initially constant front thickness, L. Let the whole interface move a distance Δ, towards the liquid phase. Mass conservation of the beads dictates that the front thickness changes as,

$$L \to L + \Delta \frac{\phi}{1-\phi}, \tag{1.5}$$

i.e. the accumulation rate can be described by the initial filling fraction ϕ. The behavior is, however, considerably more complicated if the interface is curved and stretching as it moves. The local front thickness of a moving interface can either increase or decrease depending on the geometry.

The three effects, which we have discussed above, are recurrent themes of this thesis. Any numerical scheme which aims at simulating the patterns, or theoretical model which seeks to describe the dynamics, need to faithfully account for all three effects. We will in the following, explore new numerical methods and make headway in the theoretical understanding of how the patterns are formed.

We will start off by introducing a numerical scheme for simulation of the frictional finger structures, in Paper 1. This paper will also provide new theoretical results. The numerical scheme will be crucial for Paper 2, where we investigate how frictional fingers grow under the influence of gravity, in particular how gravity can stabilize the finger growth. We will also use this system as a model system for finger structures which are found on certain remaining dyke walls[4] in the Israeli desert. In Paper 3, we switch gears, and investigate the static stresses in the front in the bubble regime, and the stability properties of the front. In Paper 4, we turn our focus to the viscous front regime. Motivated by the Viscous Front structures in Fig. 1.6, and the patterns in Fig. 1.8, we propose a numerical scheme for simulating the viscous front. Taken together we aim to expand the understanding of the patterns from the top left part of the phase diagram Fig. 1.7. By the end of this thesis, we hope to convince the reader that we have, indeed, made progress towards this goal.

[4] A (magmatic) *dyke* is what geologist call an approximately two-dimensional sheet like body of magma, which has penetrated a pre-existing body of rock in a direction which is perpendicular to the bedding planes (i.e. the planes of the sediments). If the geologist happens to be American she might call it a *dike* instead. Dykes (or dikes) grow with a vertical component, as opposed to intrusions which form in the horizontal plane, parallel to the bedding planes. They are called *sills*.

Chapter 2

A Guide to the Scientific Contributions

Below follows summaries of the scientific papers which constitute this thesis. Comments on my own involvement in the different projects are written in italics.

Paper 1: Numerical approach to frictional fingers

J.A. Eriksen, R. Toussaint, K.J. Måløy, E.G. Flekkøy, and B. Sandnes,
in review, Phys. Rev. E

This paper introduces a new strategy for simulating frictional fingers. It builds on a previous approach developed by Henning Knudsen [32], but overcomes an inherent limitation by representing the granular front as a two dimensional density field, rather than a co-moving quantity of the interface. The simulation strategy allows for simulating fingers at a higher filling fraction, which is essential for the simulations presented in Paper 2. Moreover, the paper includes a clear and detailed description of the steady state geometry of a front of the single finger. While this argument runs parallel to the argument presented in [32], it contains a correction to the steady state condition of the relationship between the front thickness and the curvature at the finger tip. The paper considers static friction behavior which scales linearly with the front thickness, rather than the more complicated friction law based on the Janssen assumption used in [32]. The linear law can be viewed as a linearization of a more complicated stress behavior with respect to the front thickness (see e.g. [3] or Papers 3), and is validated by the comparison between the theoretical prediction of the finger width and the experimental observations, for the ranges of parameters which are considered. This comparison also allows the determination of the linear coefficient needed in the friction law.

I was the main contributor to the development and the implementation of the numerical scheme, the theoretical arguments of the steady state finger growth and the writing of this paper, while benefiting from comments and corrections from the co-authors.

Paper 2: Model of finger formation at the tip of propagating dykes

J.A. Eriksen, R. Toussaint, K.J. Måløy, E.G. Flekkøy, and B. Sandnes,
submitted

In this paper we present experiments and simulations of downward frictional finger growth in a tilted cell. We elaborate on how this system explains patterns that emerge naturally in early stages of dyke formations, when magma displaces molten rocks and accumulates hard mineral grains at the interface. As the air is lighter than the liquid, the gravitational potential acts to stabilize the air-liquid boundary. The fingers tend to align and grow in parallel, and a phase diagram of the experimentally and numerically observed flow behavior is mapped out, as the tilting angle and the filling fraction is varied. We identify a transition from vertical to horizontal alignment of the fingers, i.e. a transition from parallel to transverse growth with respect to the average flow. We further give a theoretical argument based on the variations in the yield stress of the front, which qualitatively explains the transition.

Note that the theoretical argument about the transition of alignment behavior relies on a derivation of the finger width, which deviates from that used in Paper 1. While the argument of Paper 1, is more detailed in terms of the finger geometry, the underlying assumptions are not necessarily valid for competing fingers in a gravitational field. The argument presented here is simpler, and serves only to give the functional finger width dependence on the filling fraction. It is based on a minimal work assumption rather than a steady state finger growth. Both results agree with respect to the functional form of the filling fraction dependence to leading order (compare Eqs. 15 and 16 in Paper 1, with Eq. 5 in Paper 2).

My main contribution to this paper is the work underlying the simulations, and the theoretical argument which gives the qualitative explanation for the transition. I was also the main contributor in the writing of the paper.

Paper 3: Bubbles breaking the wall: Two-dimensional stress and stability analysis

J.A. Eriksen, B. Marks, B. Sandnes and R. Toussaint,
Physical Review E 91, 052204 (2015), selected as "Editors' Suggestion"

This paper proposes a two-dimensional extension of the friction model of the front, introduced in [32]. The extended model includes the effects of stresses directed tangentially to the interface, which is necessary for the logical consistency of the theoretical framework, especially when describing the stresses in curved front segments. We discuss aspects of the friction behavior which are potentially important for the stick-slip bubble behavior (see the phase diagram in Fig. 1.7), in particular how the Janssen coefficient–which gives the linear relationship between stresses in the normal and tangential direction relative to the interface–may depend on the curvature. We argue that these effects are important at the highly curved front segments which connect the different bubbles.

We also describe the presence of undulations along the interface of the stick-slip bubbles.

We show that the characteristic length of these undulations is consistent with the most unstable wavelengths of a linear stability analysis of the friction model.

The extension of the theoretical model was developed by myself in close collaboration with Renaud Toussaint. I developed the linear stability analysis, and was the main contributor to the writing of the paper.

Paper 4: Working paper: Phase field approach to viscous fronts

J.A. Eriksen, L. Cueto-Felgueroso and R. Juanes,
unpublished manuscript

This paper presents a phase field model of the viscous front, which captures the effective surface tension of the interface, the viscous behavior of the front and the front growth due to the accumulation of new beads. The model seeks to describe elements of the behavior seen in the coral structures shown in the phase diagram in Fig. 1.7 (viscous front), where a fingering instability develops within the moving front. We also present a preliminary simulation of the phase field model, which provides a proof of concept.

I have, regrettably, not found time to bring the results of this paper to a form of a publishable paper, during the course of my research. Yet, the current version of this paper presents a complete theoretical model for the viscous fronts, and therefore a result I wish to present in this thesis. A thorough numerical study of the model equations will be left for future work. The model has been developed by myself in close collaboration with Luis Cueto-Felgueroso and Ruben Juanes.

Chapter 3

Concluding remarks

It is easy to identify Paper 2 as a highlight among the scientific contributions presented in this thesis. Especially since the paper discusses a *real world* application of the experimental system which has been the common thread of thesis, and combines theory, experiments and simulations in a coherent description of the system. Novel scientific ideas can, however, be found in all the papers, and we can place the main results, in two categories.

First, we have introduced two methods for studying the system numerically:

- We have constructed a new numerical strategy for simulating the incremental displacements of a jammed front (Paper 1). This method couples the grain field to the interface, and was successfully utilized to simulate the behaviour of frictional fingers stabilized by gravity in a tilted cell (Paper 2).
- We have developed a phase field model which will allow for the simulation of the dynamics of viscous fronts (Paper 4).

Second, we have presented a number of new theoretical results:

- We have presented a new derivation of the characteristic finger width of a frictional finger (Paper 1), which improves upon previous work [32]. Using this theory, we have also shown that a linearization of the front length dependence in the yield threshold, is sufficient to account for the frictional finger behavior.
- We have developed a minimum work argument (Paper 2), which is complimentary to the result listed above, and agrees to first order.
- We have constructed an argument which explains the observed transition between vertically and horizontally aligned fingers (Paper 2).
- We have expanded the yield stress model of the front to account for the stresses in the tangential direction with respect to the interface (Paper 3).
- We have developed a stability analysis which predicts an unstable wave length along the interface of an air bubble [Fig. 1.7]. The predicted wave length is consistent with the experimental observation (Paper 3).

A path for future research, is to continue to investigate the numerical behavior of the phase field model, introduced in Paper 4. To what extent this model can describe the viscous front structures in Fig. 1.6 and the similar related patterns in Fig. 1.8, remains an open question, but the preliminary simulation presented at the end of Paper 4 is promising.

A more ambitious continuation of the results of this thesis, is to construct a model for simulating the bubble dynamics shown in Fig. 1.6. A natural starting point would be to combine the discretization scheme of Paper 1 and the stress model in Paper 3. A numerical approach to the bubble dynamics would, however, also need to describe the dynamic state at a higher level of detail. In the simulations of the frictional fingers, this is simply achieved by assuming a small but constant displacement at the weakest section of the interface. In the case of the bubble regime one would also need to account for the viscous dynamics during the expansion of a bubble, and to introduce a valid criterion for going from a slipping to a sticking state.

Bibliography

[1] B. Sandnes, E. G. Flekkøy, H. A. Knudsen, K. J. Måløy, and H. See, "Patterns and flow in frictional fluid dynamics," *Nature Communications*, vol. 2, p. 288, 2011.

[2] B. Sandnes, E. G. Flekkøy, K. J. Måløy, and J. A. Eriksen, "The shifting shapes of frictional fluids," *Revista Cubanade Fisica*, vol. 29, no. 1E23–1E26, 2012.

[3] B. Marks, B. Sandnes, G. Dumazer, J. A. Eriksen, and K. J. Måløy, "Compaction of granular material inside confined geometries," *Frontiers in Physics*, vol. 3, no. 41, 2015.

[4] H. Darcy, *Les fontaines publiques de la ville de Dijon*. Victor Dalmont, 1856.

[5] H. S. Hele-Shaw, "On the motion of a viscous fluid between two parallel plates," *Nature*, vol. 58, pp. 34–36, 1898.

[6] H. S. Hele-Shaw, "Flow of water," *Nature*, vol. 58, p. 520, 1898.

[7] P. G. Saffman and G. Taylor, "The penetration of a fluid into a porous medium or Hele-Shaw cell containing a more viscous liquid," *Proceedings of the Royal Society of London. Series A, Mathematical and Physical Sciences*, vol. 245, no. 1242, pp. pp. 312–329, 1958.

[8] P. Saffman, "Viscous fingering in Hele-Shaw cells," *Journal of Fluid Mechanics*, vol. 173, pp. 73–94, 1986.

[9] D. A. Kessler, J. Koplik, and H. Levine, "Pattern selection in fingered growth phenomena," *Advances in Physics*, vol. 37, no. 3, pp. 255–339, 1988.

[10] D. Bensimon, L. P. Kadanoff, S. Liang, B. I. Shraiman, and C. Tang, "Viscous flows in two dimensions," *Reviews of Modern Physics*, vol. 58, pp. 977–999, Oct 1986.

[11] G. M. Homsy, "Viscous fingering in porous media," *Annual Review of Fluid Mechanics*, vol. 19, no. 1, pp. 271–311, 1987.

[12] J. Nittman, G. Daccord, and M. Stanley, "Fractal growth of viscous fingers: Quantitative characterizations of a fluid instability phenomenon," *Nature*, vol. 314, p. 391, 1985.

[13] G. Daccord, J. Nittmann, and H. E. Stanley, "Radial viscous fingers and diffusion-limited aggregation: Fractal dimension and growth sites," *Physical Review Letters*, vol. 56, no. 4, p. 336, 1986.

[14] H. Van Damme, F. Obrecht, P. Levitz, L. Gatineau, and C. Laroche, "Fractal viscous fingering in clay slurries," *Nature*, vol. 320, pp. 331–733, 1986.

[15] K. J. Måløy, J. Feder, and T. Jøssang, "Viscous fingering fractals in porous media," *Physical Review Letters*, vol. 55, pp. 2688–2691, Dec 1985.

[16] J.-D. Chen and D. Wilkinson, "Pore-scale viscous fingering in porous media," *Physical Review Letters*, vol. 55, pp. 1892–1895, Oct 1985.

[17] K. J. Måløy, F. Boger, J. Feder, T. Jøssang, and P. Meakin, "Dynamics of viscous-fingering fractals in porous media," *Physical Review A*, vol. 36, no. 1, p. 318, 1987.

[18] R. Lenormand and C. Zarcone, "Invasion percolation in an etched network: Measurement of a fractal dimension," *Physical Review Letters*, vol. 54, pp. 2226–2229, May 1985.

[19] G. Løvoll, Y. Méheust, R. Toussaint, J. Schmittbuhl, and K. J. Måløy, "Growth activity during fingering in a porous Hele-Shaw cell," *Physical Review E*, vol. 70, p. 026301, Aug 2004.

[20] A. Birovljev, L. Furuberg, J. Feder, T. Jøssang, K. J. Måløy, and A. Aharony, "Gravity invasion percolation in two dimensions: Experiment and simulation," *Physical Review Letters*, vol. 67, pp. 584–587, Jul 1991.

[21] V. Frette, J. Feder, T. Jøssang, and P. Meakin, "Buoyancy-driven fluid migration in porous media," *Physical Review Letters*, vol. 68, pp. 3164–3167, May 1992.

[22] E. Lemaire, Y. O. M. Abdelhaye, J. Larue, R. Benoit, P. Levitz, and H. van Damme, "Pattern formation in noncohesive and cohesive granular media," *Fractals*, vol. 1, no. 04, pp. 968–976, 1993.

[23] M. J. Niebling, R. Toussaint, E. G. Flekkøy, and K. J. Måløy, "Dynamic aerofracture of dense granular packings," *Physical Review E*, vol. 86, p. 061315, 2012.

[24] M. J. Niebling, R. Toussaint, E. G. Flekkøy, and K. J. Måløy, "Numerical studies of aerofractures in porous media," *Revista Cubanade Fisica*, vol. 29, no. 1E66–1E70, 2012.

[25] R. Holtzman, M. L. Szulczewski, and R. Juanes, "Capillary fracturing in granular media," *Physical Review Letters*, vol. 108, p. 264504, Jun 2012.

[26] X. Cheng, L. Xu, A. Patterson, H. M. Jaeger, and S. R. Nagel, "Towards the zero-surface-tension limit in granular fingering instability," *Nature Physics*, vol. 4, no. 3, pp. 234–237, 2008.

[27] Ø. Johnsen, R. Toussaint, K. J. Måløy, and E. G. Flekkøy, "Pattern formation during air injection into granular materials confined in a circular Hele-Shaw cell," *Physical Review E*, vol. 74, p. 011301, Jul 2006.

[28] Ø. Johnsen, C. Chevalier, A. Lindner, R. Toussaint, E. Clément, K. Måløy, E. Flekkøy, and J. Schmittbuhl, "Decompaction and fluidization of a saturated and confined granular medium by injection of a viscous liquid or gas," *Physical Review E*, vol. 78, no. 5, p. 051302, 2008.

[29] C. Chevalier, A. Lindner, and E. Clement, "Destabilization of a Saffman–Taylor fingerlike pattern in a granular suspension," *Physical Review Letters*, vol. 99, no. 17, p. 174501, 2007.

[30] C. Chevalier, A. Lindner, M. Leroux, and E. Clement, "Morphodynamics during air injection into a confined granular suspension," *Journal of Non-Newtonian Fluid Mechanics*, vol. 158, no. 1, pp. 63–72, 2009.

[31] B. Sandnes, H. A. Knudsen, K. J. Måløy, and E. G. Flekkøy, "Labyrinth patterns in confined granular-fluid systems," *Physical Review Letters*, vol. 99, p. 038001, Jul 2007.

[32] H. A. Knudsen, B. Sandnes, E. G. Flekkøy, and K. J. Måløy, "Granular labyrinth structures in confined geometries," *Physical Review E*, vol. 77, p. 021301, Feb 2008.

[33] Y. Méheust, G. Løvoll, K. J. Måløy, and J. Schmittbuhl, "Interface scaling in a two-dimensional porous medium under combined viscous, gravity, and capillary effects," *Physical Review E*, vol. 66, p. 051603, Nov 2002.

Chapter 4

Papers

Numerical Approach to Frictional Fingers

Jon Alm Eriksen,[1,2] Renaud Toussaint,[2,1] Knut Jørgen Måløy,[1] Eirik Flekkøy,[1] and Bjørnar Sandnes[3]

[1] *Department of Physics, University of Oslo, P. O. Box 1048 Blindern, N-0316 Oslo, Norway*
[2] *Institut de Physique du Globe de Strasbourg, University of Strasbourg/EOST, CNRS, 5 rue Descartes, F-67084 Strasbourg Cedex, France*
[3] *College of Engineering, Swansea University, Singleton Park, SA2 8PP, Swansea, UK*

(Dated: July 24, 2015)

Experiments on confined two-phase flow systems, involving air and a dense suspension, have revealed a diverse set of flow morphologies. As the air displaces the suspension, the beads that make up the suspension can accumulate along the interface. The dynamics can generate "frictional fingers" of air coated by densely packed grains. We present here a simplified model for the dynamics together with a new numerical strategy for simulating the frictional finger behavior. The model is based on a yield stress criterion of the interface. The discretization scheme allows for simulating a larger range of structures than previous approaches. We further make theoretical predictions for the characteristic width associated to the frictional fingers, based on the yield stress criterion, and compare these to experimental results. The agreement between theory and experiments validates our model and allows us to estimate the unknown parameter in the yield stress criterion, which we use in the simulations.

I. INTRODUCTION

Petroleum reservoirs, aquifers and geological formations are often highly fractured. Flow of gas, oil, groundwater and magma tend to concentrate in the confined spaces of these fractures as they have much larger permeability than the porous matrix they are embedded in [1]. The permeable pathways can be of benefit to engineered processes; artificial stimulation of reservoirs by hydraulic fracturing is increasingly common as a means of increasing the production rate of low permeability hydrocarbon reservoirs [2, 3]. In other cases, high permeability fractures pose a problem as they contribute to increased groundwater contamination transport, leakage of buried radioactive wastes [1, 4, 5], and the escape of sequestered carbon dioxide from geologic storage sites [6, 7].

Flows in fractures and fractured media are difficult to characterize and predict, and this is especially so for multiphase flows where interactions at interfaces between gas, liquid or granular phases contribute to the fluid dynamics. Typically, when one fluid displaces another in a confined space, fluid instabilities and inherent disorder in the confining geometry result in an emerging patterning of the flow and a non-trivial mixing of the two fluids. Many of these flow phenomena, with applications to flow in fracture planes, have been studied in the idealized geometry of a Hele-Shaw cell. Examples includes viscous fingering in porous media [8–10] arising from the Saffman-Taylor instability [11, 12], destabilized viscous fingers in suspensions [13], capillary fingering in a porous matrix [14–17] and the transition to fracturing [18, 19]. Similar phenomena have also been observed with a single fluid displacing deformable porous media media in Hele-Shaw cells [20–24].

We investigate here a two-phase flow phenomenon in a Hele-Shaw cell, where granular particles are suspended in the receding liquid phase. This system is known to display a rich set of flow morphologies as an immiscible fluid displaces the liquid granular mixture [25], for example labyrinth patterns [26, 27] and bubble structures [19, 28]. In particular, we study the frictional finger formation, which develops as a layer of granular material accumulates at the fluid interface.

These finger structures are distinct from viscous fingers in several ways. First, the fingers are a result of static frictional forces in a local accumulated region of grains adjacent to the interface, rather than the global viscous pressure properties of the fluid phases. The frictional fingers develop in the quasi static limit, where we can neglect the viscous forces. Second, unlike viscous fingers in porous media which is known to display a fractal interface geometry [8, 9, 29, 30], we can for frictional fingers identify a characteristic length, the finger width. While crossover behavior from frictional to viscous fingers have been observed as the driving rate is increased [19], we will focus here on the quasi static limit where the static frictional forces dominate.

We present a new numerical scheme to simulate the frictional finger structures. This scheme builds on the strategy for simulating the labyrinth structures in [26, 27], and contains crucial improvements for simulating fingers when the width of the accumulated layer of beads is comparable to the radius of curvature of the interface. We also present experimental results together with a theoretical model for the dynamics, and predictions for how the characteristic finger width varies with the parameters. The theoretical comparison to experimental results validates our understanding, and fixes a parameter used in the simulation.

In order to set the stage for the numerical scheme, we will in Section II first describe the details of the experimental system that we want to simulate. We present our theoretical model in Section III, and we describe the numerical scheme in detail in Section IV. In section V, we present a derivation for the characteristic finger width, and compare this both to the experimental and the nu-

merical results. We finally sum up our findings in Section VI.

II. THE EXPERIMENT

A. Setup

Consider a Hele-Shaw cell, constructed as a rectangular channel, 20 cm wide, 30 cm long and with a gap of $h = 0.5$ mm (Fig. 1 a and b), filled with a suspension composed of a fluid mixture of glycerol and water, and glass beads (Fig. 1 c). The Hele-Shaw cell is fixed horizontally. The viscous fluid is a water-glycerol solution, 50% by volume. The viscosity of the liquid ensures that the beads are suspended during the filling of the cell, such that the beads are almost uniformly distributed in the cell plane. The beads are polydisperse with a mean diameter of 75 μm (Fig. 2 a), and are characterized by low granular friction (Fig. 2 b) due to the almost spherical shape of the grains (Fig. 2 c). The density of the glass beads and the liquid, are respectively $\rho_g = 2.4$ g/cm^3 and $\rho_l = 1.13$ g/cm^3. The density contrast, $\Delta\rho = \rho_b - \rho_l = 1.27$ g/cm^3, makes the beads sediment out of the liquid mixture and form a layer of granular material on the bottom plate of the Hele-Shaw cell, with a packing fraction which corresponds to a random loose packing fraction of spheres. The average thickness of this layer, relative to the gap of the cell, will be referred to as the normalized filling fraction ϕ. The Hele-Shaw cell is sealed along the long sides, and one of the short sides. The other short side is open to air at the ambient pressure.

The system is driven in one of two different ways, which leads to the same dynamics in the range of parameters we consider. Either, air is injected into the cell through an inlet nozzle located at the sealed short side, or liquid is sucked out from the same nozzle, and the air is entering the cell from the open short side. A syringe pump (Aladdin WPI) is used in both cases. The driving rate is varying in the range 0.01–0.03 ml/min. In the case of air injection, the syringe pump contains an air reservoir of 15 ml at atmospheric pressure, at the start of the experiment.

B. Experimental Results

As the air phase displaces the mixture, the interface bulldozes up the beads from the sedimented region, such that the beads accumulate along the air-liquid interface, and fill the whole cell gap in a region adjacent to the interface. We will refer to the region of accumulated beads as the *front* (see Fig. 1 c). After a short transient initial period, the entire interface develops a well defined front. In the subsequent evolution, only a small section of the interface moves at any given time. The motion consists

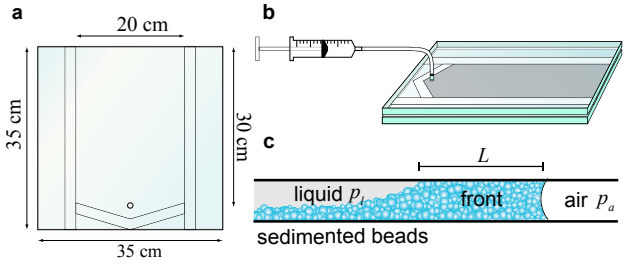

FIG. 1. (Color online) Experimental setup. a) Hele-Shaw cell dimensions. b) The system is fixed horizontally, and is filled with a fluid and sedimented beads, and driven either by air injection, or withdrawal of the liquid, through a syringe pump connected at nozzle at the sealed short side channel. c) The advancing gas phase accumulates a front of grains.

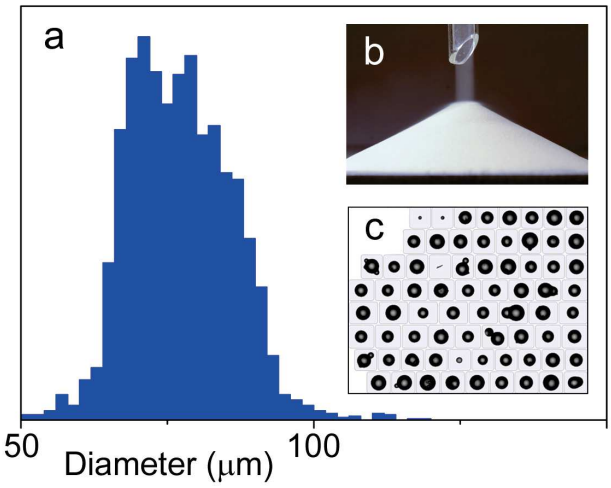

FIG. 2. (Color online) a) Bead size distribution. b) Cone of granular material poured through a funnel, angle of repose $\approx 27^\circ$, c) Microscopy images of beads (Malvern, Morphology G3) shows the approximate spherical shape of the beads.

of stick-slip like increments as the air phase fills an ever-increasing volume of the cell. The motion is always directed towards the liquid phase. A moving section of the interface tends to continue its motion over many consecutive stick-slip events, before it eventually stops and the motion continues at another section of the interface.

The friction from the accumulating front renders the advancing interface unstable, and the air phase develops finger-like structures. The fingers have a characteristic width which emerges as a result of a balance between interfacial tension and the friction of the front [19, 26, 27]. We refer to the pattern forming process as "frictional fingering", to highlight the frictional component which distinguish the patterning from viscous fingers resulting from the Saffman-Taylor instability [11]. Fig. 3 shows a series of images taken at 2 hour time intervals illustrating the pattern formation. The fingers branch out and

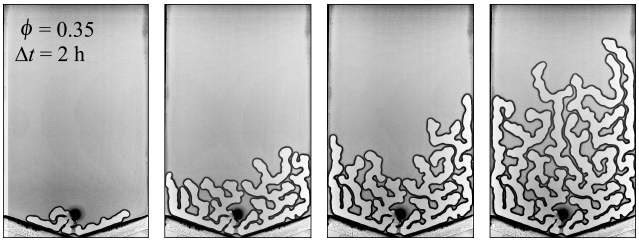

FIG. 3. The pattern formation process is documented over a 10 hour period, with 2 hour intervals between the individual images. Air is injected through the inlet at the bottom side. The cell is 20 by 30 cm.

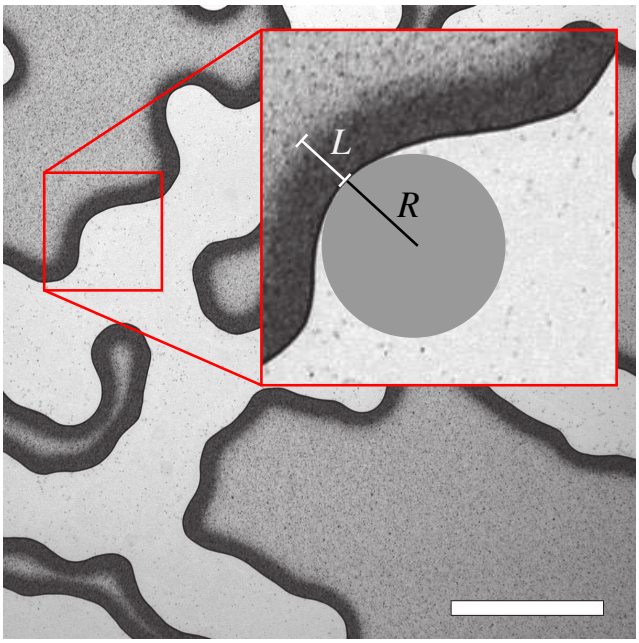

FIG. 4. (Color online) Close up of frictional finger pattern where the compacted front is visible as a dark band surrounding the air fingers. The inset shows the front thickness L, and the radius of curvature R, which are local parameters along the interface. The scale bar is 20 mm long.

grow in an isotropic, random fashion. Where two fingers meet or grow side by side, their fronts combine, and the motion of the interfaces stagnates. The fingers are prevented from merging by the beads in the front, and the gas phase thus constitutes a loop-less, simply-connected cluster, as does the residual granular-fluid phase. In the case of air injection, the evolution continues until a finger breaks through the outer boundary. In the case of liquid drainage, the evolution continues until the air phase reaches the inlet of the syringe pump. The final pattern of branching fingers is open with pockets of undisturbed settled granular suspension of varying sizes left behind. Fig. 4 shows a close up showing the air fingers surrounded by a dark front of accumulated grains.

As we increase ϕ, we observe a gradual decrease in the characteristic finger width, as shown in Fig. 5.

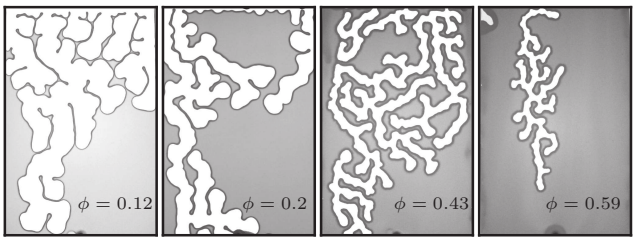

FIG. 5. Finger formation for increasing values of the filling fraction ϕ. Liquid is drained from the bottom side. The cell is 20 by 30 cm.

III. THEORETICAL MODEL

A. Stresses at the Interface

It is instructive to make an order of magnitude estimate of the capillary number for the system, $\mathrm{Ca} = \mu V/\gamma$, where μ is the viscosity, V is the typical velocity and γ is the surface tension. The typical velocity of the finger growth, when averaged over many stick-slip cycles, can be estimated from the compression rate, $q = 0.01$–0.03 ml/min. Assuming that the width, w, of a moving section is $w \simeq 1$ cm, we have $V = q/(hw) \simeq 10^{-4}$ m/s. For the water-glycerol mixture we have that $\mu \simeq 6$mPa s, and $\gamma = 60$ mN/m, which makes $\mathrm{Ca} \simeq 10^{-5}$. The small capillary number, tells us that we can neglect the viscous pressure drop in the fluids, the relevant physics is confined at the interface.

The front can be characterized by a thickness, L, at any point along the mobile parts of the interface, i.e. the parts of interface which have not yet stagnated due to the presence of a neighboring finger. This thickness is defined as the shortest distance from the air-liquid interface, through the accumulated beads, to a point where the beads no longer fill the whole cell gap (Fig. 1 c).

The beads are wetting and the interface consists of concave menisci between the layer of beads closest to the air phase at the length scale of a bead diameter, as sketched in Fig. 6. The large scale interface along the air side of the front region appears, however, smooth and we can assign a signed, in-plane curvature (κ) to every point along the interface, averaged over a number of neighboring beads. We define the curvature to be positive when the radius of curvature, $R = 1/|\kappa|$, can be drawn into the air phase (Fig. 4). The out-of-plane curvature component of the smoothed interface ($\kappa_\perp$) is constant along the interface.

We neglect the hydrostatic pressure difference over the height of the cell gap, and we approximate both the air pressure, p_a, and the liquid pressure, p_l, as uniform in their respective phases. The capillary pressure over the

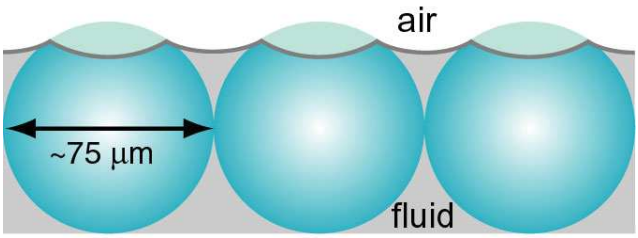

FIG. 6. (Color online) Sketch of the menisci around the beads at the air-liquid interface. The beads are wetting, resulting in concave menisci in the interspace between the beads.

menisci between the beads is,

$$\Delta p = p_a - p_l. \tag{1}$$

In the sticking state, the capillary pressure is steadily growing. In the case of air injection, the air pressure increases due to the compression. In the case of fluid withdrawal, the liquid pressure decreases. We assign a capillary pressure threshold to every point along the interface, above which the nearby front gets mobilized and advances a small step towards the liquid, i.e. a slip event occurs.

This threshold depends on two different effects. First, as the capillary pressure increases, the air-liquid menisci advances a small distance into the interspace between the beads, and the pull on the beads in the direction perpendicular to the smooth, large scale interface is increased. This induces an effective stress, σ_e, on the bead packing normal to the averaged interface. Once this solid stress grows above the yield threshold of the bead packing, $\sigma_e > \sigma_Y$, the static packing breaks and the corresponding section of the front slides. This yield threshold is a local property of the mobile parts of the front, and we will in the subsequent discussion approximate it by a linearly increasing function of the front thickness, L.

Second, when the front slips and moves a small step towards the fluid phase, the interface deforms and the surface energy changes. We assume that the changes in the total air-liquid surface, as the menisci advances into the interspace between the beads during the sticking state, is negligible. The total surface energy of the air-liquid interface is, under this assumption, insensitive to the fluctuations in the capillary pressure during the intermittent dynamics of the interface. The surface energy scales with the number of menisci along the interface, and therefore with the apparent area of the smoothed interface. We assign an effective surface tension, γ, to the smoothed interface, and the effective force which opposes an increase of surface area can be expressed according to Young's law as $\gamma(\kappa+\kappa_\perp)$. Note that the effective surface tension may deviate from the value of the surface tension of the liquid mixture. We will, however, not need its numerical value in the simulations described in the next Section.

The threshold criterion for a slip of a section of the interface, is given by,

$$\Delta p > \gamma(\kappa + \kappa_\perp) + \sigma_Y(L). \tag{2}$$

The next moving section of the interface is identified by having local parameters κ and L, which minimize the right hand side of Eq. (2). Note that $\kappa_\perp$ is constant along the interface, and plays no role in the identification.

During a slip, new beads from the sedimented region accumulate at the front. The interface deforms, which alters the curvature κ. The interface may increase or decrease depending on the curvature, and the combined effect of deformation of the interface and the accumulation of new beads will change the local value of L. The menisci between the beads will retract, and the solid stress relaxes. A new static configuration of beads is formed and the motion stops. The interface evolves in a series of such stick-slip events.

Note that the capillary pressure over the menisci, Δp, at mobile regions of the interface remains well below the capillary pressure threshold for the interface to penetrate into the bead packing. The interface drags the beads along.

B. Approximating the Yield Stress

The effective stress, σ_e, is carried from frictional contacts along the Hele-Shaw cell boundaries to the interface, predominantly via force chains in the bead packing. The exact yield threshold, σ_Y, of a section of the interface depends on the bead configuration in the front region associated with the interface section. We approximate the yield stress as the sum of a discrete set of consecutive force bearing arc chains, in the direction perpendicular to the interface, each contributing with an average tangential stress along each boundary plate, $\sigma_\xi/2$. The total force per unit area opposing the motion and transmitted from the two boundaries is therefore σ_ξ. These chains have an associated length, ξ, in the direction through the front, and the number of them corresponds to L/ξ. We have,

$$\sigma_Y = \sigma_\xi L/\xi. \tag{3}$$

The yield stress is thereby approximated as an increasing function of the front thickness.

Note that the linear L-dependence of the yield stress, can also be viewed as a linear approximation of a more complicated $\sigma_Y(L)$. Previous papers [26, 27, 31, 32], have modeled $\sigma_Y(L)$ by use of the Janssen effect [33], i.e. that the shear stress at the plate boundaries is proportional to the normal stress in the direction perpendicular to the interface, which results in a yield stress which grows exponentially with L. Ref. [31] also discuss how the curvature of the interface affects the bead stress. These models do, however, include extra unknown parameters which are hard to measure experimentally. We will estimate the only unknown parameter for the simulations, i.e. $\gamma\xi/\sigma_\xi$,

by experimental comparison to theoretical predictions in Section V. We will further show that the linear approximation is in agreement with the experiments for the ranges of parameters considered here.

By combining Eqs. (2) and (3), we can write the slip criterion as,

$$\Delta p > \gamma\kappa + \sigma_\xi L/\xi, \tag{4}$$

where we ignore the constant contribution of $\kappa_\perp$.

IV. SIMULATION

A. Numerical Representation

We reproduce the behavior observed in the experiments by numerical simulations. The numerical approach is to represent the interface by a chain of nodes. Each node, i, contains information about its coordinates (x_i, y_i), and its nearest neighbors, $i \pm 1$. The beads are represented by a two-dimensional bead concentration field, f, discretized into grid cells, $f_{n,m}$. The front is identified as all the grid cells of the bead concentration field with unit value, $f_{m,n} = 1$. The grid cells in the region which represents the sedimented layer of beads, take the value of the initial filling fraction, $f_{n,m} = \phi$. All the grid cells in the interior regions of the chain, i.e. the region corresponding to the air phase, are ignored. The discretization is illustrated in Fig. 7.

We need to identify a front thickness, L_i, to every mobile node. We do this by identifying a *link* to a cell in the bead concentration field with cell value less than one, i.e. the cells which represent the sedimented region. This link is defined by the cell which has the minimum distance from the cell center to the node coordinates. The link thereby establishes a connection between the node index i, and the field indices m and n, at the outer boundary of the front, and the length between the node and the cell center of the link cell, defines L_i. Note that the direction towards the link cell which defines the front thickness may deviate from the direction perpendicular to the interface.

We also need to define a reasonable criterion for deciding when a node is stagnant. We do this by identifying a set of candidate cells to every node. These candidate cells are limited by a circle sector centered around the node position, spanned symmetrically by an angle of β, around the direction perpendicular to the interface (see the green region in Fig. 7 b). The radius of the circle sector, $L_{\max}$, serves as a cutoff length, and needs to be set to a value much greater than the expected front thickness of a moving segment, but less than the finger width. We will in the following use the experimentally observed finger half width, $L_{\max} = \Lambda$ (see Fig. 11), and $\beta = 90°$. If a link cannot be established within these candidate cells, i.e. all the candidate cells take unit values or are in the interior of the chain, the node is considered stagnant.

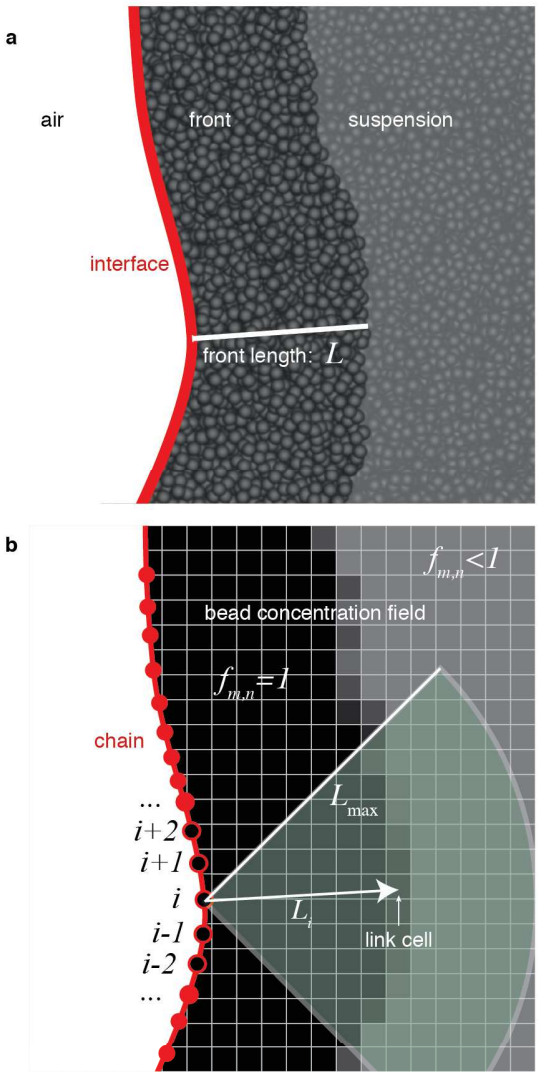

FIG. 7. (Color online) Discretization procedure. (a) The Hele-Shaw cell seen from above. The air phase on the left hand side. Adjacent to the air interface is the front, which is an accumulated region of beads. We can assign a front thickness, L, every mobile point along the interface. (b) The interface is discretized as a chain of nodes. The beads are discretized into a two-dimensional concentration field, which takes the value 1 in the front, and the initial filling fraction ϕ in the regions of not yet accumulated/sedimented beads. The size of the grid cells, and the node spacing is exaggerated for the purpose of the illustration. L_i is the shortest distance from node i through the accumulated regions, to a point in the bead field below 1. The grid cell candidates are limited to the shaded circle section of 90°, centered around the direction perpendicular to the interface.

It is convenient to define a ideal node separation length δ, and we can use this length scale as a basis unit for the other length scales in the simulation. We will set this length to $\delta = 0.4$ mm (i.e. a chain corresponding to an interface which spans the width of the Hele-Shaw cell is composed of approximately 500 nodes). Note that this length scale is slightly smaller than the Hele-Shaw cell gap, which is 0.5 mm. The grid cell spacing of the bead concentration field, δ_{grid}, is set to $\delta_{\text{grid}} = 2/3 \times \delta \simeq 0.27$ mm. Note that these lengths (δ and δ_{grid}) are both larger than the size of an individual grain (Fig. 2). The grid spacing of the bead concentration field will naturally limit the resolution of the front thickness. To mask the direction of the underlying grid structure, we need to modify the front thickness by an additional random number uniformly distributed in the interval $(-\delta_{\text{grid}}, \delta_{\text{grid}})$, which corresponding to the resolution of the grid. The front thickness is, however, ill-defined on this length scale; the random modification will not alter the large scale behavior.

The curvature, κ_i, is estimated by calculating derivatives of a spline approximation of the interface. We use a two dimensional B-spline [34], which is parameterized by the piece wise linear approximation to the arc-length parameter. The first derivative of the spline at the position of the central node, gives the unit tangent vector. The second derivative gives the curvature vector which points in the direction perpendicular to the interface. The FITPACK library [34], is used to efficiently calculate the spline, and its derivatives.

The curvature and the front thickness of the theoretical model relevant for the simulation, are local to the interface, and we can assign a threshold value, Δp_T^i, to every node. By discretizing Eq. (4), we have that this threshold value is given by,

$$\Delta p_T^i = \gamma\kappa_i + L_i\frac{\sigma_\xi}{\xi} = B\left(\frac{\xi\gamma}{\sigma_\xi}\kappa_i + L_i\right), \qquad (5)$$

where B is a multiplicative constant. The node corresponding to the minimal value of the right hand side will be insensitive to B. We use the numerical value of $\xi\gamma/\sigma_\xi = 0.0361$ cm^2. This value comes from the estimated by experimental observations of the characteristic length Λ, which we will discuss in the next Section (Fig. 11).

Before we go on describing the dynamics in the next subsection, we will spend a couple of paragraphs justifying the discretization scheme we have described. Using a chain of nodes, i.e. Lagrangian tracer particles to represent a moving interface, rather than e.g. countors of an indicator field, has certain problematic aspects [35]. The accuracy, and the stability of this chain representation are dependent on the node spacing, which will vary as some nodes moves together, while others separate. Redistribution and interpolation of nodes is therefore necessary to faithfully represent the interface, and we will describe this in detail in the following subsection. We also have to make sure that the topology of the interface remains simple, in the sense that a node is not allowed to move in-between others and thereby move into the interior of the interface. These are issues which are absent if the interface is represented as a contour. For our specific problem, however, the chain representation has a number of advantages, which outweighs the above-mentioned problems.

Only a small section of the total interface will move at any given time. Computation is therefore limited to a subset of easily identifiable active nodes. The chain representation permits us also to sort nodes by a lower bound for the threshold, which enables an efficient identification of the next moving node. The stress threshold of an inactive node, j, may change. This can happen if the displacement of active nodes adds mass to the region near the inactive node, such that L_j increases, or by the displacement of neighbouring nodes which alters the curvature κ_j. The stress threshold of an inactive node, separated from the active nodes by at least the number of neighbors used to estimate the curvature, can, however, never decrease. We can, therefore, store a lower threshold bound for these nodes.

The chain representation of the nodes is also convenient for calculating the area enclosed by the chain, as we can easily triangulate the enclosed domain.

B. Dynamics

We model the motion of the interface, by iteratively moving a small segment of the chain. Moving multiple nodes, rather than a single one, is necessary to keep the interface, and its curvature, smooth. A time-step constitutes the motion of a set of neighboring nodes, in the direction towards the suspension. As the air flux is constant, we can infer the true time from the displaced area.

In the following, we need to make some arbitrary choices regarding the number of moving nodes, etc. The numerical results seems to be insensitive to the specific rules, as long as the size of the displacement of the nodes at every time-step is sufficiently small, and that the curvature at the boundary nodes and its neighbours (see Fig. 8) varies sufficiently smooth.

The moving segment is limited to three neighbors on each side (7 nodes in total), and all of them need to be mobile. The center node, i, of the moving segment is, at every time-step, identified by the minimum of the pressure threshold, Eq. (5),

$$i = \text{argmin}_j \Delta p_T^j. \qquad (6)$$

The new positions of the interface is approximated by calculating a spline function, as shown in Fig. 8. This spline is calculated on the basis of the two non-moving next neighboring nodes on each side of the 7 moving nodes, and the point lying a distance $\delta_{\text{move}} = 0.1\delta$ from the previous coordinates of the central node, in the perpendicular direction outwards from the chain. To calculate the spline, we also need the arc-length parameter for the

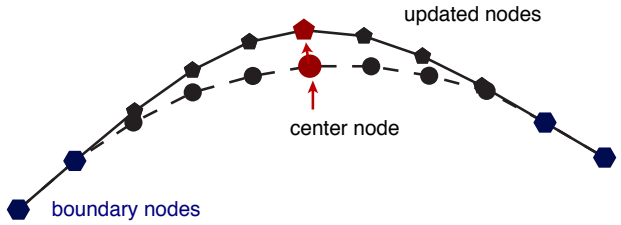

FIG. 8. (Color online) Schematic of the moving segment. 7 nodes are moving. Old configuration is marked by circles on a stapled line, new configureation is marked by pentagons on a solid line. The spline which determines the updated positions are based on the two neighboring nodes on each side of the interval (hexagons), and the center node moved a distance δ_{move} in the direction normal to the chain. The positions of the new nodes, are distributed along the spline function. Dimensions in the figure are exaggerated.

interface *after* the movement. To estimate this, we use the arc-length of segment before it moves, and modify it with a factor, s, corresponding to the stretch, or contraction, in accordance with the mean curvature along the moving segment. If a circle, with radius R expands, such that $R \to R + \delta_{\text{move}}$, the circumference, C, is modified by a factor, $C \to C(1 + \delta_{\text{move}}/R)$. By analogy, we approximate the expansion by,

$$s = 1 + \bar{\kappa}\delta, \tag{7}$$

where $\bar{\kappa}$ is the average curvature of the all the moving nodes. The positions of the new nodes are set by equidistantly distributing the moving node coordinates along this new spline. Note that the width of the moving section is fixed: 7 nodes moves at each time step. This width is smaller than the typical width of a slipping section event in the experiments, which can correspond to the finger width. When we iterate many time-steps, we recover behavior of the experiments.

At every time-step, we also need to accumulate beads in the concentration field, to ensure mass conservation. We can easily triangulate the displaced area, by considering the coordinates of the moving nodes, before and after the displacement. By calculating the area of the triangulation, we can associate an amount of displaced beads to every moving node. The beads corresponding to this area, will be added to its link grid cell. If the total of the new beads, and the existing bead mass at the closest grid cell exceeds 1, the grid cell value is set to 1 and the residual mass is added to the next link grid cell. This is repeated until either all the mass is displaced, or no link is found among the node's candidate grid cells, in which case the node is considered stagnant for the rest of the simulation. When two front segments merge together their nodes will naturally turn stagnant. It is therefore not necessary to control for overlapping segments.

Before we start a new time-step, we use the spline to interpolate the chain. We calculate the total arc-length, S, of the moving segment in between the first non-moving boundary nodes on both sides of the moving interval. We get the ideal number of nodes, N_{nodes}, to fill in between the boundary nodes, by $N_{\text{nodes}} = \text{round}(S/\delta) - 1$. If this number differs from 7 (the original number of moving nodes), we equidistantly redistribute N_{nodes} nodes along the spline, between the boundary nodes.

We can sum up the algorithm, by the following procedure. At each time-step we:

1. Identify the next moving node by Eq. (6), and its neighbors.
2. Estimate the spline function for the new configuration.
3. Iteratively move each node, accumulate to the bead concentration field according to the displaced area for every moved node.
4. Add or subtract and redistribute nodes if necessary.

To induce some random behavior which results in the fingering pattern, we add a random perturbation to the bead concentration field. This random perturbation is limited by $\pm 5\%$, and is correlated over $\simeq 50$ grid point, corresponding to the width of $\simeq 1$ cm. We generate this distribution by a bicubic interpolation of a field of uncorrelated variables, with 50 interpolated points between each uncorrelated value. This noise is needed to trigger the branching of the fingers.

A series of frames for the evolution of the finger structures generated by this numerical scheme is shown in Fig. 9.

This numerical scheme differs from the one used in [27], to simulate labyrinth patterns in a similar system, in two important ways. First, a set of neighboring nodes, rather than a single one, is moved at every time-step. This is done to assure that the curvature remains reasonably smooth, and allows us to use several neighboring nodes (more than 3) to approximate the derivatives of the path of the interface, which in turn is used to define the curvature and the perpendicular direction.

Second, the granular field is numerically represented as a two-dimensional field, rather than a local quantity which moves with the nodes of the interface. In the scheme presented in [27], each node contains a thickness vector in the direction perpendicular to the interface, which length equals the front thickness. Each pair of neighboring nodes span out a trapezoid, such that the corners correspond to the nodes' positions, and the positions of the thickness vectors. The front is thereby effectively represented as a chain of trapezoids (see Fig. 7 in [27]). This scheme works fine as long as the node separation, i.e. the resolution, needed to simulate the structures is approximately equal to the front thickness. If the node separation is small compared to the length of the thickness vectors, small deformations of the chain could lead to large displacements of the thickness vectors, which again leads to large errors in the mass conservation of the front.

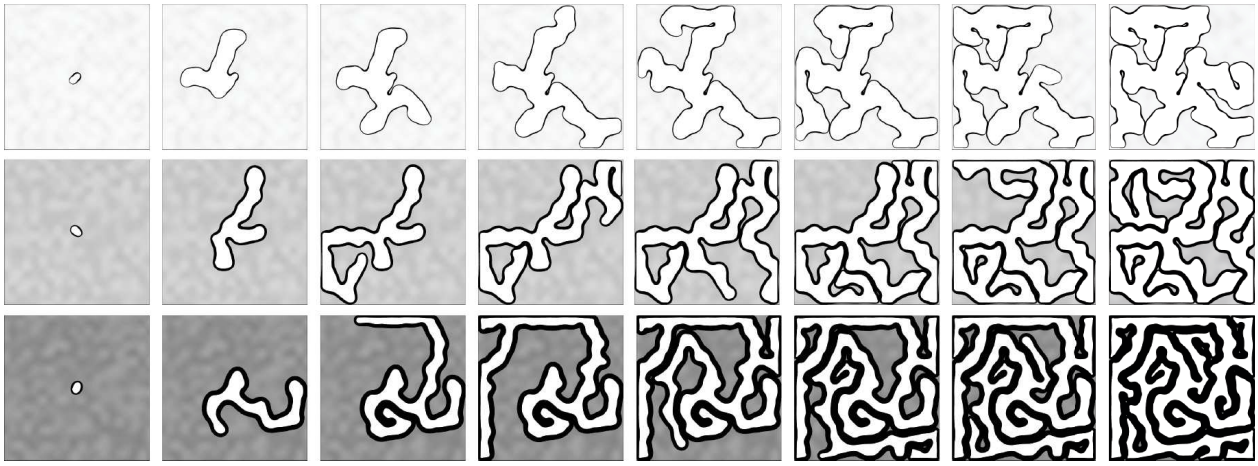

FIG. 9. Examples of the evolution of the numerical scheme with a central, circular injection point. The size of the geometry is 10×10 cm. Each row represents a time series of the evolution. Top row is $\phi = 0.1$, middle row $\phi = 0.3$ and bottom row $\phi = 0.5$. There is an additional noise field in the initial bead configuration, limited to $\phi \to \phi \pm 0.05$.

Moreover, neighboring thickness vectors could cross, and the front representation would be completely unphysical. A small node separation compared to the front thickness is indeed needed in order to faithfully discretize the system at $\phi > 0.35$, i.e. beyond the results for labyrinth structures presented in Ref. [27]. This is needed for the application of simulation aligned fingers in a tilted Hele-Shaw cell [36].

V. THE CHARACTERISTIC LENGTH

Consider a steadily growing finger as shown in Fig. 10. The curvature at the sides of the finger is 0, and $1/R$ at the finger tip. Let L_t and L_s be the front thickness at the tip and at the side of the finger respectively. In the quasi static approximation, we have that the pressure threshold over front at the side of the fingers equals that of the finger tip. By Eq. (4), we have,

$$\frac{\sigma_\xi}{\xi} L_s = \frac{\gamma}{R} + \frac{\sigma_\xi}{\xi} L_t. \tag{8}$$

The frictional fingers can be characterized by a width, and we will let Λ denote half this finger width as shown in Fig. 10. As the cell gap, h, is constant, we have that the air volume in the Hele-Shaw scell, scales with the apparent area of the air phase as seen from above, A_{air}, and that the surface area of the interface scales with the apparent circumference, C, of the air-liquid interface. The ratio between the enclosed area and the circumference of the air phase, $\Lambda = A_{\text{air}}/C$, will on average correspond to half of the finger width and serves as a natural definition of a characteristic length.

Consider now a single finger which moves into the suspension. An increment of the displacing air volume, $h\delta A_{\text{air}}$, where δA_{air} is the increased area of the air phase, will be accompanied by an increased volume of the front $h\delta A_{\text{front}}$, due to the accumulation of new beads. Mass conservation gives that,

$$\delta A_{\text{front}} = \frac{\phi}{1-\phi} \delta A_{\text{air}}. \tag{9}$$

The curvature (κ) varies smoothly along the interface, and will take its maximum value at the fingertip. We can approximate a small section around the fingertip by a circular shape, with a radius, R, equal to the reciprocal of the maximum curvature. We assume that the finger moves in a steady state, such that the fingertip retains its shape during the evolution. The area element of the front of the fingertip, can be approximated by a section of an annulus (Fig. 10). The area of this section is $A_{\text{front}} = \theta((R + L_t)^2 - R^2)$ where θ is a small angle which bounds the section on both sides of the fingertip. A small variation of this element, with respect to θ and L_t, is given by,

$$\delta A_{\text{front}} = 2\theta(R + L_t)\delta L_t + (2RL_t + L_t^2)\delta\theta. \tag{10}$$

When the tip of the finger moves forward by an infinitesimal distance, δx, the air volume associated with the front element increases by $\delta A_{\text{air}} = 2\theta R\delta x + O(\delta x^2)$. Note that the interface at θ, moves a distance $\delta x \cos\theta$ in the direction normal to the interface (along the longest cathetus of the white triangle in Fig. 10), to retain the circular shape. This perpendicular displacement stretches the original section of the interface. The projection of the displacement onto the circular interface gives $R\delta\theta = \delta x \sin\theta \simeq \delta x\theta$ (along the shortest cathetus of the white triangle in Fig. 10), where the last approximation is valid when $\theta \ll 1$. When we combine this with Eq. (9) and Eq. (10), we get,

$$\left(1 + \frac{L_t}{R}\right) \frac{\delta L_t}{\delta x} = \frac{\phi}{1-\phi} - \frac{L_t}{R}\left(1 + \frac{L_t}{2R}\right), \tag{11}$$

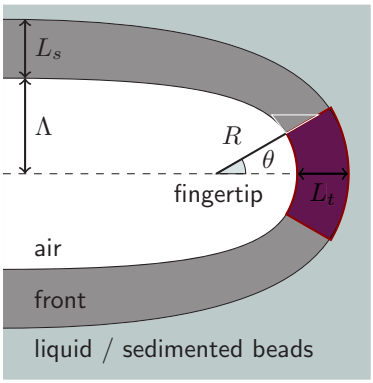

FIG. 10. (Color online) Schematic snapshot of a steadily growing finger. Λ is half the finger width, L_s is the front thickness at the sides of the finger, and L_t is the front thickness of the fingertip. The annulus section at the finger tip identifies a small region of the front at the fingertip, bounded by an angle θ. The maximum curvature of the fingertip is $\kappa = 1/R$.

In a steady state, we have $\delta L_t/\delta x = 0$, which leads to the following condition at the fingertip,

$$\frac{L_t}{R} = \sqrt{\frac{1+\phi}{1-\phi}} - 1. \tag{12}$$

Note that this expression provides a correction to Eq. (22) in Ref. [27]. We can rewrite the right hand side of the above equation as $(1 + 2\phi/(1-\phi))^{1/2} - 1$. In the limit where $\phi/(1-\phi)$ is small, we get that $L_t/R \simeq \phi/(1-\phi)$ to first order in $\phi/(1-\phi)$, which agrees with the expression in Ref. [27].

We assume that a steadily growing finger will grow in a way which minimizes the threshold pressure. When we use Eq. (12), to eliminate $\kappa = 1/R$ in the pressure threshold for the fingertip (Eq. (4) evaluated at equality), we get

$$\Delta p = \frac{\gamma}{L_t}\left(\sqrt{\frac{1+\phi}{1-\phi}} - 1\right) + \frac{\sigma_\xi}{\xi} L_t. \tag{13}$$

Minimizing the right hand side with respect to L_t gives,

$$L_t = \sqrt{\frac{\gamma\xi}{\sigma_\xi}\left(\sqrt{\frac{1+\phi}{1-\phi}} - 1\right)} \tag{14}$$

Mass conservation dictates that $L_s/\Lambda = \phi/(1-\phi)$. Using this with Eqs. (8), (12) and (14), gives

$$\Lambda = 2\sqrt{\frac{\gamma\xi}{\sigma_\xi}}\,\chi \tag{15}$$

where we have introduced,

$$\chi = \frac{1-\phi}{\phi}\sqrt{\sqrt{\frac{1+\phi}{1-\phi}} - 1}, \tag{16}$$

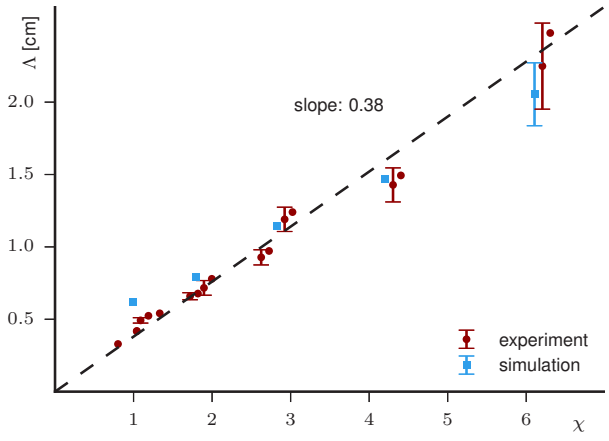

FIG. 11. (Color online) The characteristic length Λ is the ratio between the area of the finger structures and the finger structure circumference. Error bars correspond to one standard deviation, data points without error bars correspond to single observations. The stapled line corresponds to the best fit of the theoretical prediction in Eq. (15). The slope of 0.38 cm corresponds to the numerical value prefactor $2\sqrt{\gamma\,\xi/\sigma_\xi}$, which is used to infer the numerical value of $\xi\gamma/\sigma_\xi$.

to simplify the notation.

This relationship is clearly seen when we plot the experimentally observed Λ versus χ (Fig. 11). We use the linear coefficient to estimate $\gamma\xi/\sigma_\xi = (0.38/2)^2 = 0.0361$ cm^2, in the simulation, which again gives consistent results for Λ calculated for the resulting patterns of the simulations (Fig. 11), although the results of the simulations overpredicts Λ slightly for low values of χ, i.e. high values of ϕ. Note that if we expand χ in $\phi/(1-\phi)$, we have that $\chi \simeq \sqrt{(1-\phi)/\phi}$ to leading order.

A similar prediction for Λ can be made when a yield stress of the bead packing ($\sigma_Y(L)$) grows exponentially with L [27]. The good agreement between experiments, simulations and theory (Fig. 11), validates the linear approximation (Eq. (3)) for the ranges of parameters we consider here.

VI. CONCLUSION

In conclusion, we have presented a new numerical scheme for simulating frictional fingers. The scheme discretizes the interface as a chain of nodes, which is coupled to a two-dimensional mass field, needed to calculate the accumulated layer of beads along the interface. This numerical representation improves an earlier scheme [27], and enables us to simulate structures where the front thickness is large compared to the length scale at the details of the interface.

The dynamics is generated by a simplified threshold model, based on the effective surface tension of the interface and the bead stress in the front (Eq. (4)). The only

free parameters in the model is inferred from the comparison of the experimentally observed finger width, to the theoretically predicted value (Fig. 11). We successfully reproduce experimentally observed patterns (Figs. 9, 11).

The branching behavior of the finger growth is triggered by noise in the system. In the experimental setup there are multiple sources of noise, e.g. fluctuations in the force chains through the front which results in the static friction, variations in the static friction properties between the beads and the bounding glass plates, and variations in the height between the glass plates. The dominating source of noise in the simulation is the imposed fluctuations in the bead field. In addition, noise in the simulation arises from the discretization of the chain and the noise imposed on L_i, which is needed to mask the underlying grid. While the noise in the simulation is sufficient to generate patterns which share the same qualitative structures as the experimental result (compare Figs. 3, 5 and 9), exactly how the correlation in the different sources of noises affect the branching behavior remains an open question. This question lies outside the scope of this article, but we note that this might be studied by considering how the branching geometry is affected by the imposed correlation structure in the initial bead field.

Another line of future research is to use the discretization procedure to simulate bubble structures seen in the same experimental setup [19, 28]. As discussed in Subsection IV B, the discretization scheme does not rely on a small front thickness relative to the radius of curvature, as previous approaches did [27]. The numerical representation described here can in principle represent the highly curved front segments along the interface of a bubble. Such a simulation would, however, need a more sophisticated dynamical rule than Eq. 4 to account for the bubble expansion.

ACKNOWLEDGMENTS

We thank Benjy Marks for discussions at various stages of the project. J.A.E. acknowledges support from the Research Council of Norway through the CLIMIT Project No. 200041, and from Campus France through the Eiffel Grant. B.S. acknowledges support from the EPSRC grant EP/L013177/1. R.T., K.J. and E.G.F. acknowledges support from The European Unions Seventh Framework Programme for research, technological development and demonstration under grant agreement No. 316889-ITN FlowTrans. R.T. also acknowledges support from the University of Oslo and Université de Strasbourg.

[1] M. Sahimi, *Flow and Transport in Porous Media and Fractured Rock: From Classical Methods to Modern Approaches, 2nd Edition* (Wiley-VCH Verlag, Weinheim, Germany, 2011).
[2] R. Vidic, S. Brantley, J. Vandenbossche, D. Yoxtheimer, and J. Abad, Science **340** (2013), 10.1126/science.1235009.
[3] T. Patzek, F. Male, and M. Marder, PNAS **110**, 19731 (2013).
[4] B. Berkowitz, Adv. Water Resour. **25**, 861884 (2002).
[5] C.-F. Tsang and I. Neretnieks, Rev. Geophys. **36**, 275 (1998).
[6] A. Cavanagh, Int. J. Greenh. Gas Con. **21**, 101 (2014).
[7] J. Song and D. Zhang, Env. J. Sci. Tech. **47**, 9 (2013).
[8] K. J. Måløy, J. Feder, and T. Jøssang, Phys. Rev. Lett. **55**, 2688 (1985).
[9] J.-D. Chen and D. Wilkinson, Phys. Rev. Lett. **55**, 1892 (1985).
[10] G. M. Homsy, Annual Review of Fluid Mechanics **19**, 271 (1987).
[11] P. G. Saffman and G. Taylor, Proceedings of the Royal Society of London. Series A, Mathematical and Physical Sciences **245**, pp. 312 (1958).
[12] D. Bensimon, L. P. Kadanoff, S. Liang, B. I. Shraiman, and C. Tang, Rev. Mod. Phys. **58**, 977 (1986).
[13] C. Chevalier, A. Lindner, and E. Clement, Physical review letters **99**, 174501 (2007).
[14] R. Lenormand and C. Zarcone, Phys. Rev. Lett. **54**, 2226 (1985).
[15] R. Lenormand, E. Touboul, and C. Zarcone, Journal of Fluid Mechanics **189**, 165 (1988).
[16] A. Birovljev, L. Furuberg, J. Feder, T. Jøssang, K. J. Måløy, and A. Aharony, Phys. Rev. Lett. **67**, 584 (1991).
[17] V. Frette, J. Feder, T. Jøssang, and P. Meakin, Phys. Rev. Lett. **68**, 3164 (1992).
[18] R. Holtzman, M. L. Szulczewski, and R. Juanes, Phys. Rev. Lett. **108**, 264504 (2012).
[19] B. Sandnes, E. G. Flekkøy, H. A. Knudsen, K. J. Måløy, and H. See, Nat. Commun. **2**, 288 (2011).
[20] E. Lemaire, Y. O. M. Abdelhaye, J. Larue, R. Benoit, P. Levitz, and H. van Damme, Fractals **1**, 968 (1993).
[21] Ø. Johnsen, R. Toussaint, K. J. Måløy, and E. G. Flekkøy, Phys. Rev. E **74**, 011301 (2006).
[22] X. Cheng, L. Xu, A. Patterson, H. M. Jaeger, and S. R. Nagel, Nature Physics **4**, 234 (2008).
[23] M. J. Niebling, R. Toussaint, E. G. Flekkøy, and K. J. Måløy, Physical Review E **86**, 061315 (2012).
[24] M. J. Niebling, R. Toussaint, E. G. Flekkøy, and K. J. Måløy, Rev. Cub. Fis **29** (2012).
[25] B. Sandnes, E. G. Flekkøy, K. J. Måløy, and J. A. Eriksen, Rev. Cub. Fis **29** (2012).
[26] B. Sandnes, H. A. Knudsen, K. J. Måløy, and E. G. Flekkøy, Phys. Rev. Lett. **99**, 038001 (2007).
[27] H. A. Knudsen, B. Sandnes, E. G. Flekkøy, and K. J. Måløy, Phys. Rev. E **77**, 021301 (2008).
[28] B. Sandnes, E. Flekkøy, and K. Måløy, The European Physical Journal Special Topics **204**, 19 (2012).
[29] G. Løvoll, Y. Méheust, R. Toussaint, J. Schmittbuhl, and K. J. Måløy, Phys. Rev. E **70**, 026301 (2004).
[30] R. Toussaint, G. Løvoll, Y. Méheust, K. J. Måløy, and J. Schmittbuhl, EPL **71**, 583 (2005).
[31] J. A. Eriksen, B. Marks, B. Sandnes, and R. Toussaint,

Phys. Rev. E **91**, 052204 (2015).
[32] B. Marks, B. Sandnes, G. Dumazer, J. A. Eriksen, and K. J. Mly, Frontiers in Physics **3** (2015), 10.3389/fphy.2015.00041.
[33] H. Janssen, Zeitschr. d. Vereines deutscher Ingenieure **39**, 1045 (1895).
[34] P. Dierckx, *Curve and Surface Fitting with Splines* (Oxford University Press, Oxford, England, 1995).
[35] J. Sethian, *Level Set Methods and Fast Marching Methods Evolving Interfaces in Computational Geometry, Fluid Mechanics, Computer Vision, and Materials Science* (Cambridge University Press, Cambridge, England, 1999).
[36] J. A. Eriksen, R. Toussaint, E. G. Flekkøy, K. J. Måløy, and B. Sandnes, in preparation **0**, 0 (2015)

Model of finger formation at the tip of propagating dykes

Jon Alm Eriksen,[1,2] Renaud Toussaint,[2,1] Knut Jørgen Måløy,[1] Eirik Flekkøy,[1] and Bjørnar Sandnes[3]

[1] *Department of Physics, University of Oslo, P. O. Box 1048 Blindern, N-0316 Oslo, Norway*
[2] *Institut de Physique du Globe de Strasbourg, University of Strasbourg/EOST, CNRS, 5 rue Descartes, F-67084 Strasbourg Cedex, France*
[3] *College of Engineering, Swansea University, Singleton Park, SA2 8PP, Swansea, UK*

(Dated: June 8, 2015)

Sheet intrusions are the main conduits for magma in the Earth's crust. The intrusive mechanisms underlying the formation of these structures, in particular the small-scale flow properties at the tip of the intrusion, where the magma interacts with the host rock, is largely unknown [1]. Remaining patterns of aligned finger structures, found in the erosion resistant walls of the host rock in the Ramon Area in Israel [2, 3], provide evidence for a hitherto unexplored flow behaviour of magma displacing a fluidized sandstone containing quartz grains. We report here on a model system for the patterning properties of the flow, which generates aligned frictional fingers [4, 5] as an invading fluid displaces a granular mixture in a gravitational potential. We identify the characteristic features of remaining structures, in particular how the direction of the alignment changes as we vary the effect of gravity and the filling fraction of the grains. We can predict these features by the interplay between granular friction, surface tension and the accumulation of grains. Our results demonstrate the importance of friction forces acting at the interface where the solid granular material accumulates, and that observable residual morphologies in the host rock walls are manifestations of these local interactions rather than viscous forces as previously thought [3].

Multiphase flows in confined spaces are difficult to characterize. Typically, when one phase displaces another, fluid instabilities or inherent disorder result in emerging patterning and non-trivial mixing of the phases [4, 6–16]. The mechanism underlying the pattern formation is often hard to identify, especially for magmatic flow at the tip of dykes, i.e. vertically oriented intrusions. This dynamics is invisible to us; the remaining small-scale structures are only available for examination after erosion. Most existing models for propagating magmatic intrusions make a number of simplifications to obtain analytic predictions, like linearizing the behaviour of the associated deformations and ignoring the two-phase flow nature of the magma and the fluidized host rock [1, 17–23]. While simple models may be valuable for understanding large scale features of the dyke propagation [24–26], they fail to capture the two-phase flow properties at the boundary between the magma and the potentially fluidized host rock, in particular close to the propagating tip [1].

A peculiar example of dykes is found in the Inmar formation, of the Ramon area in Israel (N30°37'14" E34°56'57"). There, the igneous rock has eroded away, and the erosion resistant dyke walls, made by quartzitic sandstone, are exposed. These walls display a rich network of mould-like finger structures [2, 3]. The fingers are identified as grooves in the sandstone; outward bulging ridges separate the fingers from its neighbours. A finger is approximately 1-10 cm wide and 10-100 cm long, and the wall shows intermittent patches of finger alignment (Fig. 1 a and c). The walls are separated $\simeq$ 1 m apart, but mirror images of the structures remain on both walls, which suggests that the structures were made during the initial stages of the dyke formation.

The ridges contain a closely packed concentration of quartz grains (100-500 μm diameter) cemented by iron oxides and kaolinite, in contrast to the relatively low concentration of quartz grains in the rock near the grooves [3, Fig. 12]. Kaolinite obscures the original composition of the dyke [3], but the finger structures indicate that the sandstone was fluidized, and that the grains were accumulated onto stagnant regions adjacent to the interface of the invading magma, which filled the grooves. These structures have previously been attributed to viscous fingers, due to the Saffman-Taylor instability [6], between the fluidized host rock and a less viscous dyke-related fluid in front of the invading magma [3]. We hypothesize here, that intergranular frictional forces in these closely packed regions govern the formation of the patterns.

In order to understand these structures, we study a model system of a confined two-phase flow involving granular particles. Our experiments generate frictional fingers [4, 5, 15] of air coated by densely packed grains, which align under the influence of gravity in a tilted Hele-Shaw cell (Fig. 2). The dynamics is quasi-static; it depends on granular friction rather than viscosity. The finger formation mechanism is therefore independent of whether the invading fluid is magma, or a dyke-related fluid, as previously suggested [3], as long as the invading phase is immiscible with the fluidized rock. The relevance of this system to the structure in the Inmar formation is substantiated by the similarity in the features of the resulting pattern, in particular tip-splitting and termination (Fig. 1 a and b), and interception of fingers by a finger which grows perpendicular to the average flow direction (Fig. 1 c and d).

Consider a rectangular Hele-Shaw cell (Fig. 3), filled with a liquid. A layer of glass beads–which constitutes

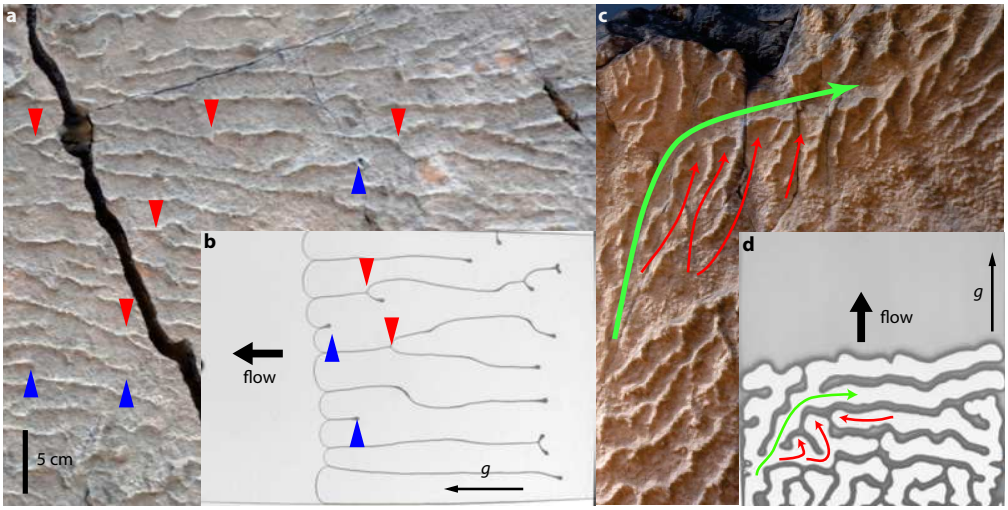

FIG. 1. Feature comparison between the remaining structures in dyke walls found in the Inmar formation (a, c) and the experimentally observed patterns (b, d). (a, b) Aligned finger structures with tip-splitting and termination, respectively marked by blue and red triangles. (c, d) Fingers (red arrows) are being intercepted by a finger (green arrows) which grows perpendicular to the average flow direction. Experimental parameters: (a) $\phi = 0.025$ and $\alpha = 4°$, (d) $\phi = 0.4$ and $\alpha = 4°$. The gravitational pull is indicated by g. The scale bar in (a) applies to all panels.

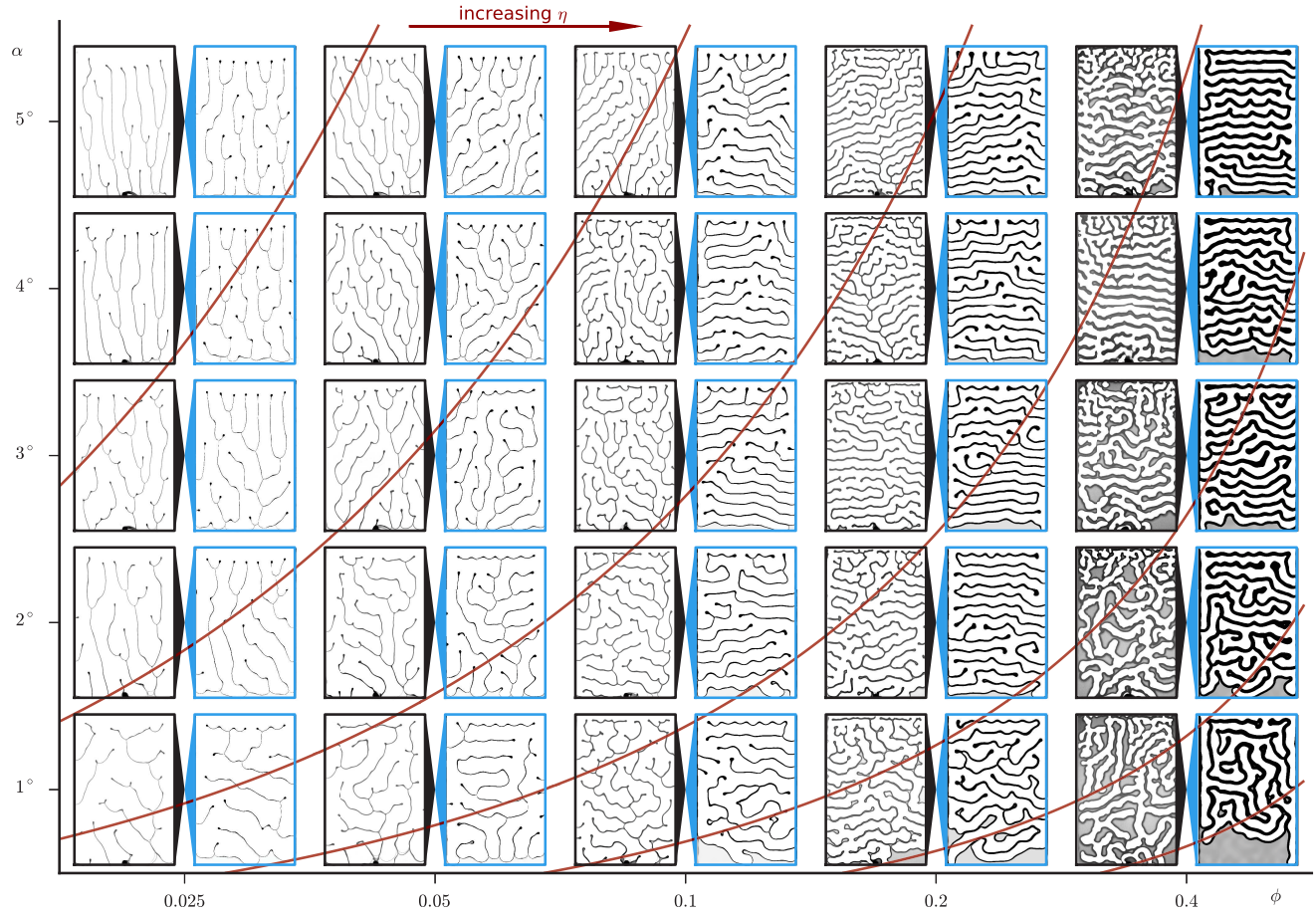

FIG. 2. Pairwise comparison of the final configuration of experiments (black/left frames) to simulations (blue/right frames), for different values of the filling fraction (ϕ), and the tilting angle (α). The gravitational pull is pointing downwards in every frame. The red lines indicate contours of constant η (Eq. (2)). As η increases, the vertical alignment turns into horizontal alignment, and then into no alignment. The value of η doubles for every contour.

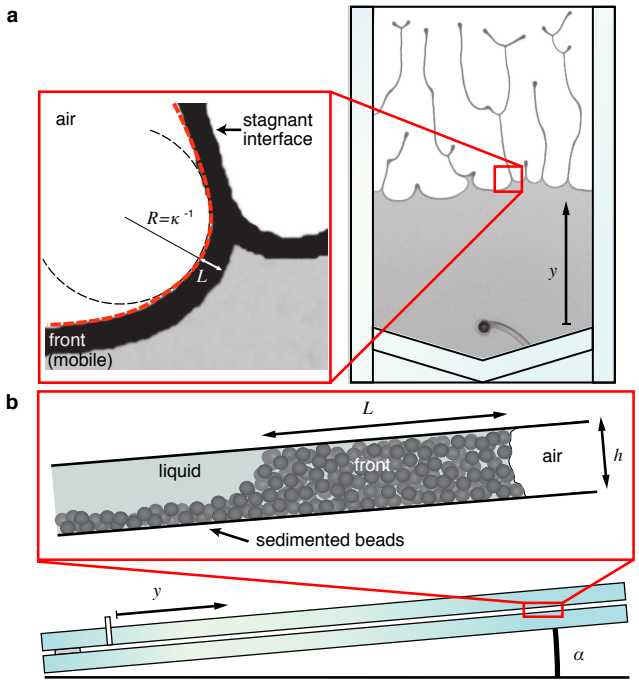

FIG. 3. Experimental setup. The cell is 20 by 30 cm. (a) Top view of the Hele-Shaw cell. The coordinate y is running from the outlet towards the upper edge of the cell, κ is the curvature (inverse of the in-plane radius of curvature R) along the interface (orange dashed line). The front is a region of accumulated grains along the air-liquid interface; L is the thickness of this front. (b) Side view close up. The cell is tilted by an angle α. The cell gap is $h = 0.5$ mm. The filling fraction ϕ is the height of the initial sedimented granular layer relative to h.

the granular material–is deposited on the bottom plate; the height of this layer, relative to the cell gap, is denoted ϕ. The long side of the cell is tilted by an angle α, to the horizontal plane. The channel is sealed along the sides and base; the upper end is open. The cell is slowly drained from an outlet at the base (Fig. 3), at constant rate. As the air displaces the liquid, grains accumulate along the air-liquid interface and fill the cell gap in a region adjacent to the interface, which we refer to as the *front* (Fig. 3). Only a small section of the interface moves at any given time, and the motion consists of incremental displacements, as the air fills an ever-increasing volume. A moving section tends to continue its motion over many consecutive increments before it stops and the motion continues at another section. The interface develops frictional fingers of air surrounded by a front [4, 5, 15], with a characteristic finger width. When different fingers move towards each other, their fronts combine, and their interfaces stagnate. The evolution continues until either the whole cell is filled with air and stagnant fronts, or the air reaches the outlet. When the cell is fixed horizontally ($\alpha = 0$), the finger directions are disordered and isotropic, and the resulting patterns are labyrinth structures of stagnant fronts [4, 5].

When the cell is tilted, the frictional fingers tend to align [27]. The direction of alignment changes as we vary α or ϕ. A phase diagram of the different patterning behaviour is shown in Fig. 2. In the low ϕ/high α range, hydrostatic height stabilization of the receding interface dominates the dynamics, the fingers advance side-by-side downwards, parallel to the gravitational field along the cell (Supplementary Video 1). Lateral growth is inhibited by the presence of neighbouring fingers on both sides; each finger is confined to downwards growth. Finger termination and tip-splitting occur at equal frequency.

As we increase ϕ and reduce α, we observe a gradual transition in the alignment; the fingers tend to grow with a directional component transverse to the hydrostatic pressure gradient. In the intermediate range of ϕ and α, hydrostatic stabilization of the front occurs, but local pressure fluctuations enables some fingers to get ahead. Sideways growth is preferred for a finger that extends beyond its neighbours due to the hydrostatic pressure gradient. The finger which manages to get ahead fills a larger fraction of the horizontal direction, and advances layer by layer, creating a pattern of horizontal lines (Supplementary Video 2). In the high ϕ/low α range the local pressure fluctuations dominate over the stabilizing effects, and alignment is lost.

The effect of tilting introduces a stabilizing potential in the experimenets. The finger directions varies between vertically downwards and horizontal; the average flow is always downwards. The fingers direction in the Inmar formation varies locally between vertically upwards and downwards, but are consistently pointing north [2]. Steps in the dyke structures indicate that the intrusion was following a propagating crack [3]. Variations in the crack opening will induce a stabilizing potential in the capillary pressure as the out-of-plane component of the magma interface curvature increases towards the crack tip. A combination of hydrostatic and capillary pressure variations, is therefore likely to act as the stabilizing potential in the dyke finger formation. Variations in the crack spacing also explain the local variations in the finger directions, and the presence of features from different parts of the phase diagram (Figs. 1, 2).

We can understand the dynamics by assigning a threshold pressure to every point along the interface. Let Δp be the difference between the air pressure, which is considered constant, and the liquid pressure at the outlet of the cell. We assume that a section of the interface is mobilized if,

$$\Delta p \geq \gamma\kappa + \sigma_\xi \frac{L}{\xi} - y\rho g \sin\alpha. \qquad (1)$$

The first term on the right hand side is the surface stress due to the locally averaged in-plane curvature of the interface, κ, and the effective surface tension, γ. The second term is the yield stress of the granular packing which constitutes the front, $\sigma_Y = \sigma_\xi L/\xi$, approximated as the

sum of a set of consecutive force bearing chains, of length $\xi < L$, each contributing with a frictional stress σ_ξ. This term can alternatively be understood as a linearization of a more complicated $\sigma_Y(L)$ [5]. The last term is the hydrostatic pressure relative to the base of the cell, y is a coordinate running along the cell from the outlet, g is the gravitational acceleration and ρ is the liquid density; κ, L and y are illustrated in Fig. 3. The pressure difference, Δp, will increase when the whole interface remains static and liquid is drained from the system. The next moving section, at any given time, is identified by local parameters κ, L and y, which minimizes the right hand side of Eq. (1). As the section yields and moves a small step towards the liquid, the local parameters are changed due to the deformation and the accumulation of new grains. In the experiments, it is sufficient to consider the in-plane component of the curvature; the out-of-plane component is constant along the interface and does not alter the identification of the moving section.

We reproduce the experimental behaviour by discretizing Eq. (1) in a numerical simulation. The similarity between the simulated and experimentally observed patterns validates our theoretical understanding. A noticeable difference is that liquid pathways in the front may break, resulting in isolated pockets of liquids in the experiments at high ϕ/low α. These effects are not included in the simulation.

We understand the transition from horizontal to vertical alignment by fluctuations in the yield stress. Let η be the ratio between the standard deviation of the granular stress, and the hydrostatic pressure corresponding to a finger width, $2\Lambda g\rho \sin\alpha$, where Λ is half the characteristic finger width. The granular yield stress, σ_Y, is approximated as the sum of a series of force bearing arc chains. We assume that these chains are uncorrelated, such that the variation in $\sigma_Y = \sigma_\xi L/\xi$ scales with the number of chains, $\mathrm{std}(\sigma_Y) \sim \sqrt{L}$. We have,

$$\eta \sim \frac{\sqrt{L}}{\Lambda \sin\alpha} \sim \frac{1}{\sin\alpha}\left(\frac{\phi}{1-\phi}\right)^{3/4}. \qquad (2)$$

The last step gives η as a function of ϕ and α (see the appendix for a derivation). The ratio indicates the behaviour of the alignment. When η is low, the fluctuations fail to disrupt the side-by-side finger growth. When the contribution of noise is comparable to the stabilizing pressure, i.e. η close to unity, a finger can get ahead of its neighbours and grow sideways, orthogonal to the direction of gravity. For large η, the fluctuations dominate over the stabilizing effect, and the alignment is lost. We can only estimate η up to a multiplicative constant, as the stress variations of σ_Y is hard to identify. Contours of constant η correspond to equal qualitative alignment behaviour (Fig. 2).

Our findings point to a rich dynamical behaviour where grains are accumulated by a moving interface between two fluids, and highlights the importance of static friction in the finger formation seen on dyke walls.

ACKNOWLEDGMENTS

This paper is dedicated to the memory of Henning Knudsen, who made important contributions to the understanding of frictional fingers. We thank Olivier Galland for comments on, and fruitful discussions about the manuscript. We also thank Benjy Marks for discussions at various stages of the project. J.A.E. acknowledges support from the Research Council of Norway through the NFR Project No. 200041/S60, and from Campus France through the Eiffel Grant. B.S. acknowledges support from the EPSRC Grant EP/L013177/1. R.T., K.J. and E.G.F. acknowledges support from The European Unions Seventh Framework Programme, Grant No. 316889-ITN FlowTrans. R.T. also acknowledges additional support from the University of Oslo and Université de Strasbourg.

1. Experimental Setup

The rectangular Hele-Shaw cell is 20×30 cm^2, with a gap spacing $h = 0.5$ mm (Fig. 3). The glass beads are polydisperse with mean diameter of 80 μm. The density of the glass beads and the water-glycerol mixture, is respectively $\rho_g = 2.4$ g/cm^3 and $\rho = 1.13$ g/cm^3. The cell was drained using a syringe pump set to a constant withdrawal rate of 0.07 ml/min. The system was imaged from underneath using PL-B742U, Pixelink camera, and illuminated by a white screen placed above.

2. Numerical simulations

The interface is represented by a one-dimensional chain of position nodes. The grains are represented by a two-dimensional mass field, and the front is identified as a region of the mass field above a threshold value. The front thickness, L, at a node is approximated as the shortest distance from the node to a cell in the mass field below the threshold. The curvature is calculated by a spline interpolation of neighbouring nodes. The dynamics are generated by iteratively moving the node according to the minimum value of the right hand side of Eq. (1). The chain is interpolated with new nodes as the interface grows. The dynamics is deterministic, and the random behaviour is a result of perturbed initial conditions, and imposed fluctuations in the mass field. We use $\sigma_\xi/\xi = 16$ kPa/m, which is an estimate based on comparison between experimental results and the theoretical expression for finger width. For the effective surface tension we use $\gamma = 60$ mN/m [5]. Details of the numerical scheme is presented in another paper (J.A.E. et al. under revision).

3. Derivation of η

We need to express L and Λ as functions of ϕ. Let A and C be respectively the area and the circumference of the air phase, as seen from above, and let h be the cell gap. The pattern is dominated by finger structures, such that $A = C\Lambda$. The work of a typical displacement, δw, has two contributions when we set $\alpha = 0$ for simplicity. First, the stretching of the interface contributes with $\gamma h\, \delta C$, where $\delta C = \delta A/\Lambda$, which follows from the assumption of constant Λ. Second, the work done against the granular stresses, σ, in the front, is $hs\, \delta x\, \sigma$, where s is the typical width of a moving segment and δx is the distance the interface advances such that $s\delta x = \delta A$. We can approximate σ, by the yield stress, σ_Y, i.e. the second term on the right hand side of Eq. (1). Putting the terms together, and dividing by the time of the displacement, gives the work rate,

$$\frac{\delta w}{\delta t} = \left(\frac{\gamma}{\Lambda} + L\frac{\sigma_\xi}{\xi}\right) h \frac{\delta A}{\delta t}, \tag{3}$$

where $h\delta A/\delta t$ equals the constant compression rate, when averaged over many stick-slip events. We assume that L is approximately constant along the interface, such that CL is the total area of the front. Mass conservation gives that $h(CL + A)\phi = hCL$, which implies that

$$L = \Lambda \frac{\phi}{1-\phi}, \tag{4}$$

where we have used $\Lambda = A/C$. Minimizing Eq. (3) with respect to Λ, under the condition of Eq. (4), which corresponds to the assumption that the pattern evolves in a way that minimizes the work, gives,

$$\Lambda \sim \sqrt{\frac{1-\phi}{\phi}}. \tag{5}$$

Using Eqs. (4) and (5) in the second step in Eq. (2) in the manuscript, gives,

$$\eta \sim \frac{1}{\sin\alpha}\left(\frac{\phi}{1-\phi}\right)^{3/4}. \tag{6}$$

[1] Rivalta, E., Taisne, B., Bunger, A. & Katz, R. A review of mechanical models of dike propagation: Schools of thought, results and future directions. *Tectonophysics* **638**, 1–42 (2015).

[2] Baer, G. & Reches, Z. Flow patterns of magma in dikes, makhtesh ramon, israel. *Geology* **15**, 569–572 (1987).

[3] Baer, G. Mechanisms of dike propagation in layered rocks and in massive, porous sedimentary rocks. *Journal of Geophysical Research: Solid Earth (1978–2012)* **96**, 11911–11929 (1991).

[4] Sandnes, B., Knudsen, H. A., Måløy, K. J. & Flekkøy, E. G. Labyrinth patterns in confined granular-fluid systems. *Phys. Rev. Lett.* **99**, 038001 (2007).

[5] Knudsen, H. A., Sandnes, B., Flekkøy, E. G. & Måløy, K. J. Granular labyrinth structures in confined geometries. *Phys. Rev. E* **77**, 021301 (2008).

[6] Saffman, P. G. & Taylor, G. The penetration of a fluid into a porous medium or hele-shaw cell containing a more viscous liquid. *Proceedings of the Royal Society of London. Series A, Mathematical and Physical Sciences* **245**, pp. 312–329 (1958).

[7] Måløy, K. J., Feder, J. & Jøssang, T. Viscous fingering fractals in porous media. *Phys. Rev. Lett.* **55**, 2688–2691 (1985).

[8] Chen, J.-D. & Wilkinson, D. Pore-scale viscous fingering in porous media. *Phys. Rev. Lett.* **55**, 1892–1895 (1985).

[9] Lenormand, R. & Zarcone, C. Invasion percolation in an etched network: Measurement of a fractal dimension. *Phys. Rev. Lett.* **54**, 2226–2229 (1985).

[10] Bensimon, D., Kadanoff, L. P., Liang, S., Shraiman, B. I. & Tang, C. Viscous flows in two dimensions. *Rev. Mod. Phys.* **58**, 977–999 (1986).

[11] Homsy, G. M. Viscous fingering in porous media. *Annual Review of Fluid Mechanics* **19**, 271–311 (1987).

[12] Lenormand, R., Touboul, E. & Zarcone, C. Numerical models and experiments on immiscible displacements in porous media. *Journal of Fluid Mechanics* **189**, 165–187 (1988).

[13] Birovljev, A. *et al.* Gravity invasion percolation in two dimensions: Experiment and simulation. *Phys. Rev. Lett.* **67**, 584–587 (1991).

[14] Frette, V., Feder, J., Jøssang, T. & Meakin, P. Buoyancy-driven fluid migration in porous media. *Phys. Rev. Lett.* **68**, 3164–3167 (1992).

[15] Sandnes, B., Flekkøy, E. G., Knudsen, H. A., Måløy, K. J. & See, H. Patterns and flow in frictional fluid dynamics. *Nat. Commun.* **2**, 288 (2011).

[16] Holtzman, R., Szulczewski, M. L. & Juanes, R. Capillary fracturing in granular media. *Phys. Rev. Lett.* **108**, 264504 (2012).

[17] Rubin, A. Propagation of magma-filled cracks. *Annual Review of Earth and Planetary Sciences* **23**, 287–336 (1995).

[18] Lister, J. R. & Kerr, R. C. Fluid-mechanical models of crack propagation and their application to magma transport in dykes. *Journal of Geophysical Research: Solid Earth (1978–2012)* **96**, 10049–10077 (1991).

[19] Spence, D. & Turcotte, D. Magma-driven propagation of cracks. *Journal of Geophysical Research: Solid Earth (1978–2012)* **90**, 575–580 (1985).

[20] Fialko, Y. A. & Rubin, A. M. Thermal and mechanical aspects of magma emplacement in giant dike swarms. *Journal of Geophysical Research: Solid Earth (1978–2012)* **104**, 23033–23049 (1999).

[21] Galland, O. & Scheibert, J. Analytical model of surface uplift above axisymmetric flat-lying magma intrusions: Implications for sill emplacement and geodesy. *Journal of Volcanology and Geothermal Research* **253**, 114–130

(2013).

[22] Michaut, C. Dynamics of magmatic intrusions in the upper crust: Theory and applications to laccoliths on earth and the moon. *J. Geophys. Res.* **116**, B05205 (2011).

[23] Bunger, A. P. & Cruden, A. R. Modeling the growth of laccoliths and large mafic sills: Role of magma body forces. *Journal of Geophysical Research* **116**, B02203 (2011).

[24] Wright, T. J. *et al.* Magma-maintained rift segmentation at continental rupture in the 2005 afar dyking episode. *Nature* **442**, 291–294 (2006). 10.1038/nature04978.

[25] Krumbholz, M. *et al.* Weibull-distributed dyke thickness reflects probabilistic character of host-rock strength. *Nature communications* **5** (2014).

[26] Sigmundsson, F. *et al.* Intrusion triggering of the 2010 eyjafjallaökull explosive eruption. *Nature* **468**, 426–430 (2010).

[27] Knudsen, H. A., Sandnes, B., G., F. E. & J., M. K. Labyrinth patterns in confined and tilted granular-fluid systems. In *Powders and Grains 2009: Proceedings of the 6 International Conference on Micromechanics of Granular Media*, 1043–1046 (Springer, 2009).

Additional material: Model of finger formation at the tip of propagating dykes

The following figures did not fit into the manuscript due to length limitations. Discussions of the figures are provided in the captions.

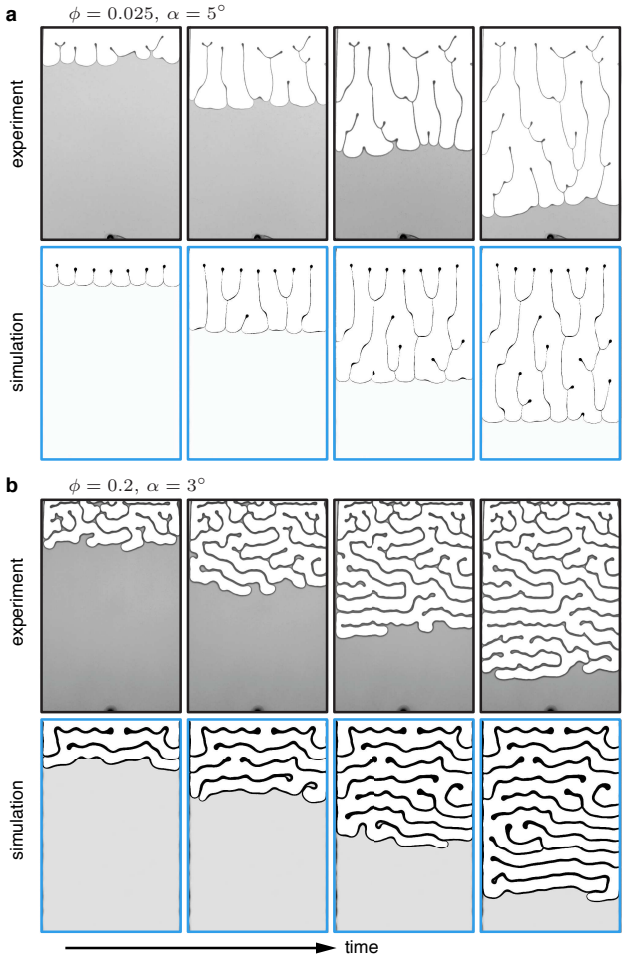

FIG. 1. Snapshots of the time evolution, experiments versus simulations. (a) The pattern is dominated by vertically aligned fingers at $\phi = 0.025$ and $\alpha = 5°$. (b) The pattern is dominated by horizontally aligned fingers at $\phi = 0.2$ and $\alpha = 3°$.

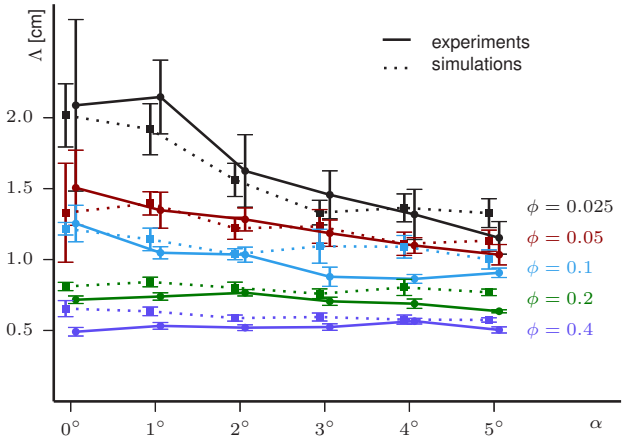

FIG. 2. The characteristic finger width Λ, i.e. the area of the air phase divided by the circumference of the interface, versus the tilting angle α, for the patterns presented in Fig. 2 in the manuscript. In the case of tilting, the characteristic width, Λ, has to be understood as an averaged quantity; the finger width depends on the growth direction of the fingers. Λ will be dominated by vertically growing fingers in the upper left corner of the phase diagram, and by the horizontally growing fingers at $\eta \simeq 1$ (Fig. 2 in the manuscript). Note that the stabilizing effect induced by gravity tends to decrease Λ at low ϕ. At $\phi > 0.1$, there is no significant α dependence on Λ. We have not been able to make an analytical prediction for Λ taking α into account, and we have ignored the α dependence in the derivation of η. However, the figure shows a good agreement between simulation and experimental results for Λ. The error bars correspond to one standard deviation of the uncertainty in the estimation.

PHYSICAL REVIEW E **91**, 052204 (2015)

Bubbles breaking the wall: Two-dimensional stress and stability analysis

Jon Alm Eriksen*
Department of Physics, University of Oslo, P. O. Box 1048 Blindern, N-0316 Oslo, Norway
and Institut de Physique du Globe de Strasbourg, University of Strasbourg/EOST, CNRS, 5 rue Descartes, F-67084 Strasbourg Cedex, France

Benjy Marks
Department of Physics, University of Oslo, P. O. Box 1048 Blindern, N-0316 Oslo, Norway
and College of Engineering, Swansea University, Singleton Park, SA2 8PP Swansea, United Kingdom

Bjørnar Sandnes
College of Engineering, Swansea University, Singleton Park, SA2 8PP Swansea, United Kingdom

Renaud Toussaint
Institut de Physique du Globe de Strasbourg, University of Strasbourg/EOST, CNRS, 5 rue Descartes, F-67084 Strasbourg Cedex, France
and Department of Physics, University of Oslo, P. O. Box 1048 Blindern, N-0316 Oslo, Norway
(Received 13 March 2015; published 26 May 2015)

Submerged granular material exhibits a wide range of behavior when the saturating fluid is slowly displaced by a gas phase. In confined systems, the moving interface between the invading gas and the fluid/grain mixture can cause beads to jam, and induce intermittency in the dynamics. Here, we study the stability of layers of saturated jammed beads around stuck air bubbles, and the deformation mechanism leading to air channel formations in these layers. We describe a two-dimensional extension of a previous model of the effective stress in the jammed packing. The effect of the tangential stress component on the yield stress is discussed, in particular how arching effects may impact the yield threshold. We further develop a linear stability analysis, to study undulations which develop under certain experimental conditions at the air-liquid interface. The linear analysis gives estimates for the most unstable wavelengths for the initial growth of the perturbations. The estimates correspond well with peak to peak length measurements of the experimentally observed undulations.

DOI: 10.1103/PhysRevE.91.052204 PACS number(s): 45.70.Vn, 47.56.+r, 46.32.+x

I. INTRODUCTION

Multiphase flow involving unconsolidated granular media and granular-fluid mixtures occur in a wide range of environmental and engineered processes. Examples include gas venting in sediments, volcanic eruptions, soil wetting and drying, oil and gas recovery, hydraulic fracturing, and carbon geosequestration [1–6]. Similar flow systems are also attracting an increasing scientific interest. A range of flow behaviors have been observed, including destabilized viscous fingers [7], granular decompaction fingers [8–10], channeling [1,11], gas expulsion of imbibated nanoparticle aggregates [12], aerofractures [13,14], and fractures involving immiscible fluids [15–19]. In particular, when a layer of granular material accumulates at the fluid interface, a rich set of flow morphologies have been observed [20], such as labyrinth patterns of frictional fingers [21,22], frictional fingers aligned by gravity [23], and bubble structures [15,24]. Examples of frictional fingers and bubble patterns are shown in Fig. 1.

Consider a horizontal Hele-Shaw cell, filled with a liquid mixture containing beads which sediment out of the liquid. Air is compressed into the cell. The compression rate is so slow (0.01–0.03 ml/min) that the process can be considered quasistatic. The air displaces the liquid mixture in small intermittent incremental steps. The invading air-liquid interface bulldozes up the beads from the sedimented region, and accumulates the beads into a compacted region adjacent to the air-liquid interface. This accumulated region will in the following be referred to as the *front*.

An important control parameter for the experiment is the normalized filling fraction, ϕ, i.e., the height of the sedimented region relative to the cell height. This parameter determines the rate of accumulation of new beads onto the front, as the air-liquid interface advances. As the pattern develops, most of the front is jammed, and only a small section of the interface evolves in intermittent, stick-slip-like increments. For $\phi < 0.4$, the system generates treelike structures of frictional fingers [see Fig. 1(a)], with a characteristic finger width [21,22]. When the filling fraction ϕ increases, the displaced volume per increment also increases, and the increment frequency decreases. The increments start to form bubbles, rather than small deformations at a finger tip, and the remaining pattern consists of a series of bubbles connected by thin channels of air [24] [see Figs. 1(b) and 1(c)]. After a bubble is formed, the front around the bubble settles down in a static configuration. As the pressure increases beyond a certain level, the front slowly deforms and undulations along the air-liquid interface develop. One of the peaks of these undulations gets ahead of the others and forms a narrow channel through the front. Once the channel approaches the sedimented region, it accelerates, and bursts into a new bubble. A closeup picture of the structure of the bubbles is shown in Fig. 2; videos of the dynamics are provided as Supplemental Material [25].

*Corresponding author: jonaerik@fys.uio.no

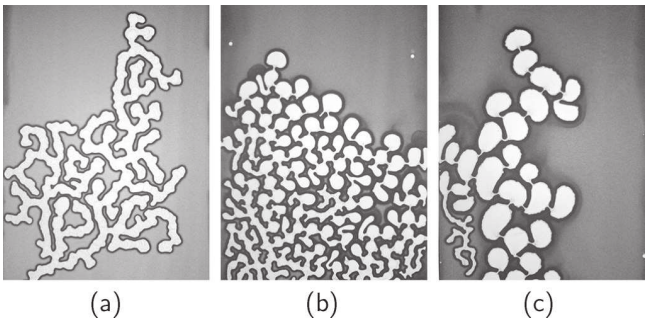

FIG. 1. The Hele-Shaw cell as seen from above (20 × 30 cm). Air (white region) is injected into a liquid mixture with a layer of sedimented beads on the bottom plate (gray region). The front is the accumulated region of beads along the air interface (the dark rim around the white regions). The different images correspond to different normalized filling fractions ϕ, i.e., the height of the sedimented layer relative to the cell gap. (a) $\phi = 0.35$, (b) $\phi = 0.49$, and (c) $\phi = 0.53$. We see a gradual transition from frictional fingers (a) to bubble dynamics (c) as ϕ increases.

The frictional finger behavior gradually transitions into the bubble behavior, either by increasing ϕ or the volume of the air in the syringe pump used to compress the air. The transition, and the experimental conditions, are described in detail in Ref. [15].

The dynamics of the finger behavior is understood, at least to the extent that the patterns can be reproduced by simulations. The patterns are simulated both for a horizontal cell [21,22], and for a tilted cell [23], where gravitational effects also are

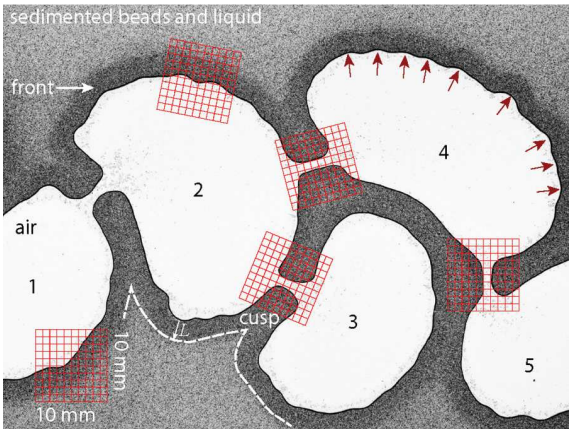

FIG. 2. (Color online) A closeup view of connected bubbles of air, which displace a liquid containing glass beads. The front is the accumulated region of beads adjacent to the air interface, and is identified as the dark region. The white dashed line indicates parts of the separation path between the front and the sedimented region. This path can develop cusps, as front segments from different bubbles merge. The front thickness (L) is only defined where this separation path runs parallel to the air-front interface. Grids of 1 mm spacing, are superposed on the image to reveal the scales. The front thickness (L) is $\simeq$3 mm thick. The channels that connect the bubbles are $\simeq$1 mm. The cell gap is 0.5 mm, and the bead diameter is 0.1 mm. The numbers refer to the order in which the bubbles are formed. The air-front interface of the bubble develops undulations. The arrows in bubble 4 points to peaks of these undulations.

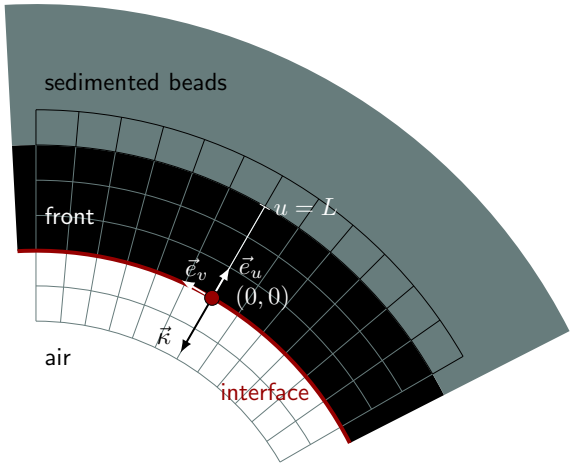

FIG. 3. (Color online) Schematics of a section of the interface, with the adjacent front, seen from above. At every point along the interface we introduce a coordinate system (u,v), such that the point is placed in the origin. The unit vectors $\vec{e}_u$ and $\vec{e}_v$ point respectively perpendicular and parallel to the interface.

present. Central to the theoretical understanding is a model of the effective stress in the front. In particular, the description of how the stress component normal to the air-liquid interface gives rise to frictional stresses along the plate boundaries. This model accounts for neither the curvature of the front in the expression for the effective stress nor the tangential stress component. It is, however, reasonable to assume that the tangential stress becomes important for highly curved interfaces, which indeed are present in the experimental observations of the bubble behavior, in particular around the channels which connect the bubbles (see Fig. 2).

The aim of this paper is twofold. First, we present a natural extension of the stress model, which also accounts for the curvature of the interface and the tangential stress component inside the packing. We will assume that the tangential and the normal stresses are linearly related. This assumption implies that the tangential stress can have a large impact on the yield stress of the interface. We will also discuss how arching effects are captured by the model, and how they may be important for describing the dynamics of the interface as it moves through the front of a bubble.

Second, we present a linear stability analysis of the deformations at the interface. This analysis gives predictions for the most unstable wavelength of the interface, which agrees well with the experimentally observed peak to peak distance of the undulations.

II. THEORETICAL CONSIDERATIONS

There are two local variables along the interface which are of special interest. One is the in-plane signed curvature of the air-liquid interface, $\kappa = \pm|\vec{\kappa}|$, where $\vec{\kappa}$ is the curvature vector, shown in Fig. 3. Note that, while the air-liquid interface may be convoluted at the scale of a single bead, we are here interested in the curvature of the averaged interface, at the scale of several neighboring beads. The absolute value of the curvature is reciprocal to the radius of curvature, $|\vec{\kappa}| = R^{-1}$,

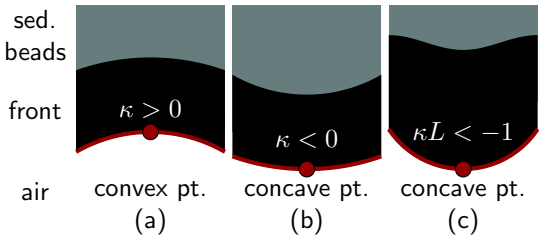

FIG. 4. (Color online) Schematic examples of different configurations. (a) Convex interface, positive curvature. (b) Concave interface, negative curvature. (c) Negative curvature with radius of curvature which is smaller than the front thickness.

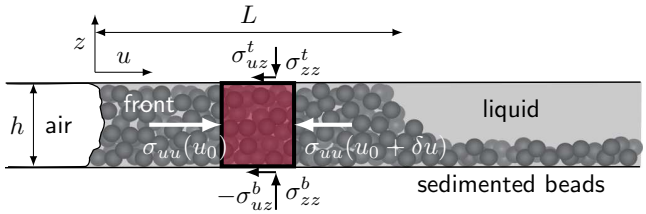

FIG. 5. (Color online) Schematic cross section of the cell at the front. The front thickness (L) is defined to be the length of the region of beads which fills the whole cell gap.

and its sign is defined to be positive if the radius of curvature can be drawn into the air phase, and negative otherwise. Examples of different configurations are shown in Fig. 4. The other variable of interest is the thickness of the front in the direction perpendicular to the interface, L, indicated in Figs. 2 and 3. This variable is, however, not applicable to every point along the interface. For example, if two front segments from different sections of the interface merge together, the corresponding sections of the interface stagnate, and remain inactive in the subsequent evolution of the interface (see for example the front enclosed between the bubbles labeled 3 and 4 in Fig. 2). Note also that the separation path between the front and the sedimented region (see the white dashed line in Fig. 2) may develop singular points (cusps), as it evolves, in contrast to the air-front interface which appears smooth everywhere due to the effective surface tension. The front thickness L is only defined where the separation path between the front and the sedimented region runs parallel to the air interface. We will, in the subsequent discussion, only consider points along the interface where L can be defined.

It is convenient to introduce a set of coordinates relative to the points along the interface. Let (u,v) be an orthogonal coordinate system, such that u runs in the direction perpendicular to the interface, and v runs parallel, as shown in Fig. 3. The interface in a small neighborhood around a given point is therefore approximated by $(0,v)$. The separation between the front and the sedimented region, if it exists at that point, is approximated by (L,v). The (u,v) coordinates will be Cartesian around straight segments and inflection points, i.e., points which correspond to $R \to \pm\infty$, or $\kappa \to 0$. For straight segments we have that $u = x$, and $v = y$ in the notation used in Ref. [22]. We can identify a polar coordinate system (r,θ), at curved segments, with origin at the center of the circle corresponding to the radius of curvature, such the interface, is located at $r = R$. The separation path between the front and the sedimented region is located at $r = R + L$ for positively curved segments, and at $r = R - L$ for negatively curved segments. We have the following transformations:

$$\begin{aligned} r &= \mathrm{sgn}(\kappa)\, u + R, \\ \theta &= \frac{\mathrm{sgn}(\kappa)\, v}{R}, \end{aligned} \tag{1}$$

where sgn is the sign function. Front lengths which are longer than the radius of curvature, $L > R$, when the interface curves negatively, are not properly accounted for [see Fig. 4(c)]. These points are rare, and we assume that they are immobile. We will also use z as the coordinate of the height direction, such that the bottom boundary is located at $z = 0$, and the top boundary at $z = h$; see Fig. 5.

A. Yield pressure at the interface without tangential stresses

We will in the following first review a simplified version of the stress model used in Refs. [21,22]. This derivation will naturally motivate the inclusion of the tangential stress, presented in the next subsection.

The yield pressure associated with a deformation of a section of the interface, i.e., the air pressure at which a section of the front transitions from a sticking to a slipping state, arises from two different effects. First, the air-liquid surface tension of the menisci between the beads will generate an effective surface energy at the scale of several neighboring beads. This surface energy generates a surface stress which acts to minimize the curvature, κ. The pressure difference which corresponds to the effective surface tension γ is given by $\gamma\kappa$.

Second, force chains in the front transmit stresses from the boundary of the cell to the beads at the interface, resulting in an effective normal stress at the interface of the bead packing. Let $\boldsymbol{\sigma}$ be the effective stress tensor field in the bead packing, which we assume to be smooth and continuous at the scale of several bead diameters. We employ a positive sign convention for compressive stresses, and we ignore the z dependence in the stress field, i.e., we consider height averaged stresses. We further assume that variations in the v dependence are negligible, such that $\boldsymbol{\sigma} = \boldsymbol{\sigma}(u)$. The normal stress at the interface is denoted $\sigma_{uu}(u = 0)$.

Previous papers [15,21,22] have, in the context of frictional fingers, successfully modeled the yield pressure at the interface by assigning an L-dependent yield threshold, $\sigma_Y(L)$, to the effective bead stress, such that a local section of the interface evolves if $\sigma_{uu}(u = 0) > \sigma_Y(L)$. The slip criterion for a section of the interface is

$$p > \gamma\kappa + \sigma_Y(L), \tag{2}$$

where p is the air pressure. Note that we have ignored the pressure drop associated with the curvature in the out-of-plane direction on the right hand side of the inequality. This pressure drop is, however, constant along the interface, and does not change the location of the weakest section. In order to describe how the threshold $\sigma_Y(L)$ depends on the front thickness L we

first describe how the effective stress field varies through the front.

Consider a straight segment of the front ($\kappa = 0$) such that the (u,v) coordinates are Cartesian. Imagine a representative elementary volume in the front which is bounded by $u_0 < u < u_0 + \delta u$ and $0 < v < \delta v$. The volume fills the height of the cell such that $0 < z < h$. A cross section of this volume is shown by the black square region in Fig. 5. The force balance of the u component of the force on this volume gives us a differential equation for $\sigma_{uu}(u)$,

$$\begin{aligned} &h\delta v\left[\sigma_{uu}(u_0) - \sigma_{uu}(u_0+\delta u)\right] \\ &\quad = \delta u \delta v\left[-\sigma^b_{uz}(u_0) + \sigma^t_{uz}(u_0)\right] \\ &\quad \Rightarrow \frac{\partial}{\partial u}\sigma_{uu}(u) = -\frac{1}{h}\left[-\sigma^b_{uz}(u) + \sigma^t_{uz}(u)\right] = -F, \end{aligned} \tag{3}$$

where σ^b_{uz} and σ^t_{uz} are the u components of the shear stresses acting on the bottom and the top cell boundaries respectively, as shown in Fig. 5. In the last equation we also introduce the force density F for later convenience.

To close the system, we need to approximate how these shear stresses change with u. We will, as [21,22], follow Janssen's analysis for stresses in a silo [26], which rests on the following two assumptions. First, we assume that the stresses in the z and the u directions are proportional,

$$\sigma^b_{zz} = K_1\sigma_{uu} \quad \text{and} \quad \sigma^t_{zz} = K_1\sigma_{uu}, \tag{4}$$

where K_1 is the Janssen parameter [27]. We ignore the contribution of the weight of the beads on the bottom plate, which induces an asymmetry in the comparison of the top and bottom boundaries. This contribution was accounted for in the expression developed in Ref. [22], but gives only a minor correction to the exponential L dependence of $\sigma_Y(L)$, described below. Second, we assume that the frictional stresses are proportional to the normal stresses acting on the plates (see Fig. 5), i.e., we assume Coulomb friction. The maximum frictional stresses at the plate boundaries are given by $\sigma^t_{uz} = \mu\sigma^t_{zz}$ and $\sigma^b_{uz} = -\mu\sigma^b_{zz}$, where μ is the static friction coefficient. The result of the above assumptions is that

$$F = \frac{2\mu K_1}{h}\sigma_{uu}. \tag{5}$$

Limitations of Janssen's assumtions [Eq. (4)] is discussed in [28,29]. The result of using a relation like Eq. (5) is, however, in accordance with experimental evidence in the context of frictional fingers [22], for aerofractures [8,13,14] and for the original application of the stresses in silo geometries [26,30].

We also assume that the maximum stress the beads at the end of the front (i.e., at $u = L$) can withstand before the front segment slips is a constant σ_T, i.e., the front slides if $\sigma_{uu}(u = L) > \sigma_T$. Note that this constant is assumed to be independent of the local parameters, κ and L, of the interface. Using σ_T as a boundary condition at $u = L$, we can integrate equation Eq. (3) and get

$$\sigma_{uu}(u) = \sigma_T e^{-2\mu K_1(u-L)/h}, \tag{6}$$

which corresponds to the normal stress profile through the front at the yield transition. It is convenient to introduce a characteristic length,

$$\xi = \frac{h}{2\mu K_1}. \tag{7}$$

If we evaluate Eq. (6) at the interface ($u = 0$), we get the final expression for the yield stress,

$$\sigma_Y(L) = \sigma_T e^{L/\xi}. \tag{8}$$

Inserting this into Eq. (2), gives

$$p > \gamma\kappa + \sigma_T e^{L/\xi}. \tag{9}$$

The weakest section along the interface is identified by having κ and L such that $\gamma\kappa + \sigma_T \exp(L/\xi)$ is minimal. This criterion is used to simulate fingering behavior in Refs. [21,22], with the exception of the correction term for the weight of the grains mentioned above. σ_T can be estimated from the friction of the weight of the grains at the transition between the front and the sedimented beads, assuming a wedgelike bead profile [22]. Note also that the numerical value of K_1 is hard to determine, as it only appears multiplied with the friction coefficient μ in Eq. (7). Approximate values for the different parameters are listed in Table I. In the context of fingers in a tilted cell [23], it was adequate for the level of detail in the simulation-experiment comparison, to linearize the exponential behavior, i.e., using the first order term from the L expansion of $\sigma_Y(L)$ in Eq. (2).

TABLE I. Approximate values of the parameters of the model.

Parameter		Value	Units
Effective surface tension	γ	60	mN/m[a]
Characteristic length	ξ	0.06	cm[b]
Threshold at end of front ($u = L$)	σ_T	10	Pa[c]

[a]This is lower than the table value of glycerol-water mixture (65–70 mN/m). Note that the complex geometry of the air-liquid interface, due to the menisci between the beads, may change the effective surface tension from that of a pure liquid value. This value has, however, been used to reproduce the finger structures in simulations [22,23].

[b]$\xi = h/(2\mu K_1)$. Assuming friction constant for glass beads, $\mu = 0.5$ and the Janssen parameter $K_1 = 0.8$ [22]. The cell height is $h = 0.05$ mm.

[c]Order of magnitude estimate based on the average over-pressure presented in [15].

B. Including the tangential stress component

Equation (8) is a reasonable approximation as long as the curvature is small relative to the front thickness $\kappa L \ll 1$. We therefore do not expect it to hold in the context of bubble formation, as the geometry of the front curves significantly, especially near the channels between the bubbles. A closer inspection will reveal that σ_Y in Eq. (8) also depends on the curvature, $\sigma_Y = \sigma_Y(L,\kappa)$.

We can write the mechanical equilibrium in Eq. (3) in a more general form,

$$\text{div}\,\boldsymbol{\sigma} = \nabla\cdot\boldsymbol{\sigma}^T = -F\vec{e}_u, \tag{10}$$

where F is defined in Eq. (3) and $\vec{e}_u$ is the unit vector in the u direction. We have that the r component of Eq. (10), in the cylindrical coordinates introduced in Eq. (1) is (see for example Chap. 2 in Ref. [31])

$$\frac{1}{r}\partial_r(r\sigma_{rr}) - \frac{\sigma_{\theta\theta}}{r} = -F, \tag{11}$$

$$\Rightarrow \partial_r\sigma_{rr} = -\frac{\sigma_{uu}}{\xi} - \frac{\sigma_{rr}-\sigma_{\theta\theta}}{r}, \tag{12}$$

where we use Eqs. (5) and (7) to substitute for F in the last line. Since we already assume a Janssen approximation for the normal stress in the z direction, it is reasonable to also assume a similar linear relationship for the normal stress in the θ direction. Note that r and θ are the principal directions of the stress tensor, due to the symmetry of the annulus (see Fig. 3). Analogous to Eq. (4), we assume that

$$\sigma_{\theta\theta} = K_2\sigma_{rr}. \tag{13}$$

The principal stresses are thereby assumed to be linearly dependent on each other, but note that the K_1 parameter is used in a height averaged setting in Eq. (4), whereas K_2 relates σ_{rr} to $\sigma_{\theta\theta}$ everywhere in the (r,θ) plane. The assumption of a local linear relation between the principal stresses is also used to describe stress distributions in piles of granular material [32–34].

Using the linear dependence assumption in Eq. (13), we can rewrite Eq. (12) as

$$\partial_r \ln\sigma_{uu}(r) = -\frac{1}{\xi} - \frac{1-K_2}{r}. \tag{14}$$

Assume that the interface is positively curved, such that the interface is located at $r = R$, and the end of the front at $r = R + L$. Integrating this, with similar boundary conditions as before, $\sigma_{uu}(R+L) = \sigma_T$, and evaluating $\sigma_{rr}(r)$ at $r = R$, gives the yield stress, $\sigma_Y(L,\kappa)$. We have that

$$\sigma_Y(L,\kappa) = \sigma_T e^{L/\xi}(1+\kappa L)^{1-K_2}, \tag{15}$$

where we use $\kappa = 1/R$. One can verify that we obtain the same result if we instead consider a negatively curved section of the interface.

If we use the expression for the effective yield stress which incorporates the radial stress contribution [Eq. (15)] in the previous yield criterion [Eq. (2)], we finally have the new yield criterion,

$$p > \gamma\kappa + \sigma_T e^{L/\xi}(1+\kappa L)^{1-K_2}. \tag{16}$$

Note that if we only consider the correction to Eq. (8) in the radial direction, i.e., we disregard the $\sigma_{\theta\theta}$ contribution by setting $K_2 = 0$ in Eq. (15), the correction will always give a higher yield stress for positive curvature. If we set $K_2 = 1$, i.e., we consider isotropic stress in the (u,v) plane, we get the same stress law as in the one-dimensional model approximation in Eq. (8).

It is hard to estimate the value of K_2 in our experiments. Its local value may be very sensitive to how the beads are compacted, and may also vary along the interface. In the context of a silo geometry, Janssen coefficient less than 1 and greater than 1 have been reported, depending on the packing procedure [30]. Note that the yield stress changes qualitatively as K_2 grows beyond 1, as illustrated in Fig. 6, and that $K_2 > 1$ naturally describes arching mechanisms in the front for negatively curved segments. We will in the following assume that $K_2 < 1$ for straight segments ($\kappa \simeq 0$); this is in agreement with numerical estimates from discrete element method simulations, $K_2 \simeq 0.8 \pm 0.1$ [35]. We will further discuss K_2 in light of the subsequent stability analysis and how it may change with the curvature in Sec. III.

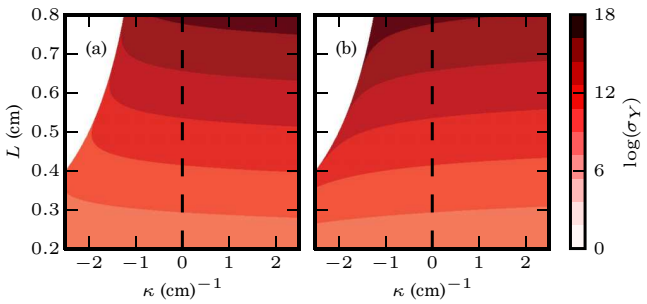

FIG. 6. (Color online) Effective yield stress, $\sigma_Y(\kappa,L)$, defined in Eq. (15), for values of K_2, less than and greater than 1. (a) $K_2 = 0.6$. (b) $K_2 = 1.4$. The contour lines are logarithmically spaced. The threshold increases as Eq. (8), along the dashed line ($\kappa = 0$). The white region in the top left corner corresponds to $\kappa L < -1$, and is not accounted for by the theory. The numerical values of the other parameters are presented in Table I.

C. Linear stability analysis of a straight front segment

We will in the following present a stability analysis by considering perturbations of a straight interface, with a constant front thickness L. Consider an infinitesimal perturbation $f_q(x)$, with wave number q, such that

$$f_q(x) = \epsilon[1+\cos(qx)]. \tag{17}$$

This perturbation is shown in Fig. 7. The perturbation amplitude ϵ is infinitesimal. Note that we only consider displacement towards the front, in the positive y direction, $f_q(x) \geqslant 0$.

A reasonable condition for growth of a perturbation can be based on the static properties of the front. We assume that the perturbation grows if the threshold at the peaks of the perturbations, i.e., at $\cos(qx) = 1$, is lower than the threshold

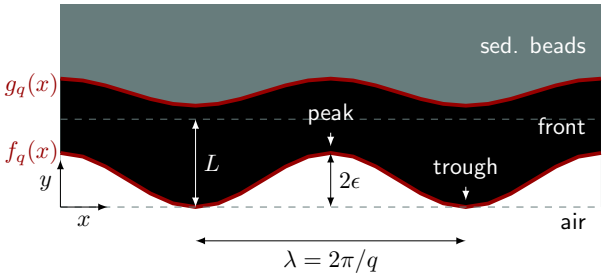

FIG. 7. (Color online) Illustration of the perturbation. The front is originally enclosed between the dashed lines. After the perturbation, it is enclosed between $g_q(x)$ and $f_q(x)$. A perturbation is considered unstable if the yield threshold at the peaks of the perturbations is lower than the threshold at the troughs, and otherwise stable.

at the troughs of the perturbation, i.e., at $\cos(qx) = -1$. Otherwise, the interface at the troughs will move before the peaks, and the perturbation will flatten out.

Let p_p and p_t be the pressure threshold of Eq. (16) (evaluated at equality), for the peaks and the troughs respectively. We introduce the stability criterion function

$$\Gamma(q) = \frac{p_p - p_t}{C}, \tag{18}$$

where C is a positive constant independent of q, which will be determined later. Γ is analogous to the negative of the growth rate of the perturbation, as used in linear stability analysis on systems where the dynamics are defined. The condition for the growth of the perturbation is now given by $\Gamma(q) < 0$, and the most unstable perturbation wave vector q^* is given by the minimum of $\Gamma(q)$, such that $\Gamma(q^*) \leqslant \Gamma(q)$.

We assume that the infinitesimal displacement results in infinitesimal pressure threshold variations, $p_p = p_0 + \delta p_p$ and $p_t = p_0 + \delta p_t$, where δp_p and δp_t are the changes of the threshold pressure induced by the perturbation at the peak and trough respectively, and p_0 is the threshold of the initial flat interface. We can therefore rewrite Eq. (18) as

$$\Gamma(q) = \frac{\delta p_p - \delta p_t}{C}. \tag{19}$$

The pressure variations can be written in terms of changes in the curvature $\delta\kappa$ and in the front length δL. We can expand Eq. (16), again evaluated at equality, to first order in $\delta\kappa$, and δL,

$$\begin{aligned}\delta p &= \frac{\partial p}{\partial \kappa}\delta\kappa + \frac{\partial p}{\partial L}\delta L \\ &= \left(\gamma + \sigma_T e^{L/\xi} L \frac{1-K_2}{(1+\kappa L)^{K_2}}\right)\delta\kappa \\ &\quad + \sigma_T e^{L/\xi}(1+\kappa L)^{1-K_2}\left(\frac{1}{\xi} + \kappa\frac{1-K_2}{1+\kappa L}\right)\delta L. \end{aligned} \tag{20}$$

Note that σ_T, which is the stress threshold at the separation between the front and the sedimented region, is assumed to be constant and independent of L and κ. Using this we have that Eq. (19) can be written as

$$\begin{aligned}\Gamma(q) = \frac{1}{C}&\left(\gamma + \sigma_T e^{L/\xi} L \frac{1-K_2}{(1+\kappa L)^{K_2}}\right)(\delta\kappa_p - \delta\kappa_t) \\ &+ \sigma_T e^{L/\xi}(1+\kappa L)^{1-K_2}\left(\frac{1}{\xi} + \kappa\frac{1-K_2}{1+\kappa L}\right) \\ &\times (\delta L_p - \delta L_t), \end{aligned} \tag{21}$$

where δL_p and δL_t are the changes in the front length at the peak and the trough respectively, and similarly for the changes in the curvature $\delta\kappa_p$ and $\delta\kappa_t$.

The curvature of the perturbation is given by the negative of the second derivative of $f_q(x)$, to first order in ϵ. The curvature is 0 for the straight segment, and after the perturbation,

$$\delta\kappa = -f_q''(x) + O(\epsilon^2) = \epsilon q^2 \cos(qx) + O(\epsilon^2). \tag{22}$$

The difference between the changes of the curvature at the peak $\delta\kappa_p$ and the changes at the trough $\delta\kappa_t$ is therefore

$$\delta\kappa_p - \delta\kappa_t = 2\epsilon q^2. \tag{23}$$

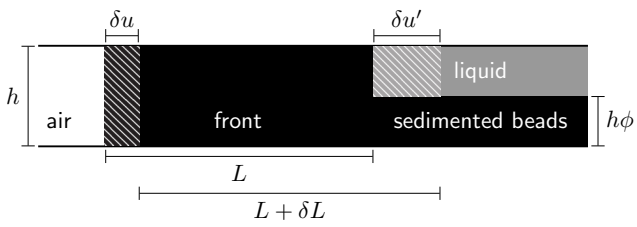

FIG. 8. Schematic representation of the cross section of the cell. The front is assumed to be incompressible. A volume associated to a displacement of a straight air-front interface ($\kappa = 0$), shown by the white striped pattern, is therefore coupled to an equal volume associated to the displacement of the front-liquid boundary (the outer boundary in Fig. 7). The regions which are marked as "liquid" and "sedimented beads" corresponds to the "sed. beads" in Fig. 7. The accumulation of the sedimented beads results in the increased displacement of the front-suspension boundary; $\delta u' = \delta u/(1-\phi)$ and $\delta L = \delta u\phi/(1-\phi)$.

We now need to express the difference of front length changes, between the peak and the trough, $\delta L_p - \delta L_t$. Let $g_q(x)$ be the path which separates the front from the sedimented layer of beads, as shown in Fig. 7, such that the front length after the perturbation is given by $g_q(x) - f_q(x)$. The perturbation gives rise to a displacement field of the front, $\vec{d}(x,y)$; we will use this displacement field to find $g_q(x)$. We assume for simplicity that the displacement field is irrotational, $\nabla \times \vec{d} = 0$, and incompressible, $\nabla \cdot \vec{d} = 0$. We can therefore write the displacement as the negative of the gradient of a harmonic field $\psi_q(x,y)$, i.e., we have $\nabla^2\psi_q = 0$, and $\vec{d} = -\nabla\psi_q$. We are only interested in displacements in the first order of ϵ, and we can limit ourselves to the y component of the deformation.

One can verify that the following field is harmonic:

$$\psi_q(x,y) = -\epsilon y + \frac{\epsilon}{q} e^{-qy}\cos xq. \tag{24}$$

Note also that the y component of the displacement corresponds to the perturbation when evaluated at $y = 0$,

$$-\frac{\partial}{\partial y}\psi_q\bigg|_{y=0} = f_q(x). \tag{25}$$

The separation path $g_q(x)$ between the front and the sedimented region, is given by the displacement field $\vec{d}(x,y)$ at $y = L$. As the separation path moves outwards it also accumulates new beads to the front. We can simply increase the displacement of the separation path between the front and the sedimented beads by a factor $1/(1-\phi)$ to account for the bead accumulation, as shown in Fig. 8. The separation path $g_q(x)$, given the perturbation at the air-front interface, is therefore

$$\begin{aligned} g_q(y) &= L - \frac{1}{1-\phi}\frac{\partial\psi_q}{\partial y}\bigg|_{y=L} + O(\epsilon^2) \\ &= L + \frac{\epsilon}{1-\phi}[1 + e^{-Lq}\cos(qx)] + O(\epsilon^2). \end{aligned} \tag{26}$$

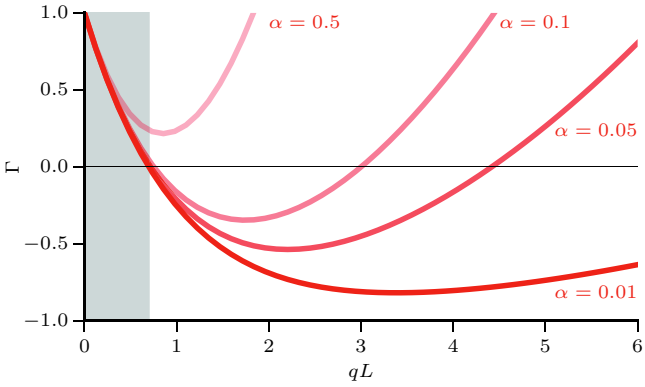

FIG. 9. (Color online) Stability criterion function Γ [Eq. (29)] versus the product of the wave number and the front length qL for various values of α. The normalized filling fraction is set to $\phi = 0.5$. The gray shaded region corresponds to $qL < -\ln(1-\phi)$, which is a stable region, independent of α [see Eq. (31)].

The change in front length along the perturbation is given by

$$\delta L = g_q(x) - f_q(x) - L + O(\epsilon^2)$$
$$= \epsilon\left[\frac{\phi}{1-\phi} + \left(\frac{e^{-Lq}}{1-\phi} - 1\right)\cos(qx)\right] + O(\epsilon^2). \quad (27)$$

The difference between the change of the front length at the peak δL_p and the changes at the trough δL_t is

$$\delta L_p - \delta L_t = 2\epsilon\left(\frac{e^{-Lq}}{1-\phi} - 1\right). \quad (28)$$

We can now rewrite Eq. (21). We choose $C = 2\epsilon\sigma_T e^{L/\xi}/\xi$, to make $\Gamma(q)$ dimensionless. By using Eqs. (23) and (28), we get

$$\Gamma(q) = \alpha(Lq)^2 + \frac{e^{-Lq}}{1-\phi} - 1, \quad (29)$$

where,

$$\alpha = \frac{\xi}{L}\left(\frac{\gamma/L}{\sigma_T e^{L/\xi}} + 1 - K_2\right). \quad (30)$$

The first term in the parentheses in Eq. (30), is of order $\sim 10^{-2}$, when we use the approximate value of $L = 3$ mm (see Fig. 2), and the values in Table I. This means that high values of qL are unconditionally unstable for $K_2 > 1 + 10^{-2} \simeq 1$, as α is negative. We will assume that $K_2 < 1$ for straight front segments, and therefore $\alpha > 0$, in the subsequent discussion. Plots of Γ versus qL, for different values of α, and $\phi = 0.5$, are shown in Fig. 9. Note that $\Gamma(q=0) = \phi/(1-\phi)$, and that variations of ϕ change the behavior in the range of low qL. Variations of ϕ are unimportant for larger qL, as $e^{-qL} \to 0$. Note also that the stability criterion function is always stable for low wave numbers; Γ is positive when

$$\frac{e^{-Lq}}{1-\phi} > 1 \Rightarrow -\ln(1-\phi) > qL. \quad (31)$$

This stable region is identified as the gray shaded region in Fig. 9. The stability in the low range of qL is imposed by the filling fraction ϕ, whereas the stability for high qL is imposed by the effective surface tension γ, through α [Eq. (30)].

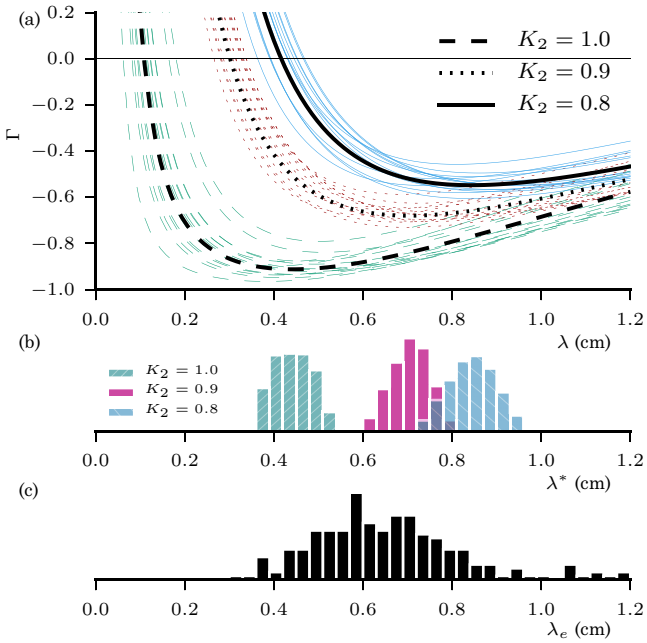

FIG. 10. (Color online) (a) Stability criterion function Γ, as defined in Eq. (29), vs the wavelength $\lambda = 2\pi/q$. A wavelength is unstable if $\Gamma(\lambda) < 0$. $\Gamma(\lambda)$ is drawn 15 times, to visualize the sensitivity to the parameters σ_T, ξ, γ, and L. For each realization, the parameters are drawn from uncorrelated uniform distributions on the interval defined by ±15% of the mean value, $L = 0.3$ cm, $\gamma = 60$ mN/m, $\xi = 0.06$ cm, and $\sigma_T = 10$ Pa in accordance with Table I. The filling fraction is fixed at $\phi = 0.5$, and $K_2 = 1.0$, 0.9, and 0.8, for the green dashed, red dotted, and blue solid lines respectively. The thick black dashed/dotted/solid lines correspond to the mean values of the parameters, for each value of K_2. (b) Histograms of the theoretically estimated wavelengths λ^*, which minimize Γ (i.e., the most unstable wavelength), based on 10^5 realizations similar to the one plotted in (a), and for the three values of K_2. (c) Experimental observations of the wavelength λ_e of the undulations. Estimated by measuring the linear peak to peak distance in the experimental pictures (see arrows in Fig. 2). This histogram is based on 214 measurements.

The wave number q^*, which minimizes Γ, can be written in terms of Lambert's W function [36], which is implicitly defined by $y = W(y)e^{W(y)}$. We have that

$$\Gamma'(q^*) = 2\alpha L^2 q^* - L\frac{e^{-Lq^*}}{1-\phi} = 0$$
$$\Rightarrow q^* = \frac{1}{L}W\left[\frac{1}{2\alpha(1-\phi)}\right]. \quad (32)$$

This wave number corresponds to the most unstable wavelength, defined by $\lambda^* = 2\pi/q^*$. Lambert's $W(y)$ function is monotonically increasing for growing positive arguments [36]. As the argument of W in Eq. (32) is increasing with increasing ϕ, higher ϕ generally corresponds to a smaller wavelength λ^*.

Different realizations of Γ [Eq. (29)] versus the wavelength $\lambda = 2\pi/q$ are plotted in Fig. 10(a), for different values of K_2. The plot illustrates also how Γ is sensitive to variations in the parameters, by superposing realizations with varying parameters ξ, L, σ_T, and γ. A histogram of the corresponding

most unstable wavelengths λ^* is shown in Fig. 10(b). These results are compared to a histogram of experimental estimates of the wavelengths of the undulations along the bubble interfaces λ_e in Fig. 10(c). The experimental estimate is based on the measured linear peak to peak distance; examples of these peaks are shown by the arrows in Fig. 2.

III. DISCUSSION

The linear stability analysis above has omitted a number of complicating factors. We have for example left out the effect of the initial curvature of the interface, by considering a straight segment. We have also ignored the complications of the intermittency, and the locality of the deformation, by assuming harmonic perturbations. Moreover, we have assumed that the parameters in Table I, the front length L, and K_2 all are constant along the interface, although they may very well be subject to systematic variations. For these reasons, the linear stability analysis is only expected to give a first order approximation. In light of the expected accuracy of the prediction, we conclude that the prediction of the linear analysis agrees well with the experimental results, for $0.8 < K_2 < 1.0$ (Fig. 10). We note that the most unstable wavelength increases with a decreasing K_2. An additional averaging over the range of K_2 will make the histograms of the theoretically estimated λ^* [Fig. 10(a)], closer to the histogram of the experimentally observed λ_e [Fig. 10(c)].

The range of plausible K_2 parameters, in agreement with the linear stability analysis (Fig. 10), is consistent with numerical estimates from discrete element method simulations [35], which estimated $K_2 = 0.8 \pm 0.1$ for a straight moving interface with a similar geometry. The values of K_2 may, however, change with the curvature of the front. This is analogous to variation of the Janssen parameter in silo experiments; the Janssen parameter is highly sensitive to the packing procedure [30]. The packing geometry of the beads in the front in our experiments may be a result of the curvature of the interface as it moves into the cell.

We conjecture that K_2 increase with decreasing curvatures, i.e., fronts adjacent to a convex interface [see Fig. 4(a)] develop a K_2 which is smaller than fronts adjacent to concave interface [see Fig. 4(b)]. This qualitative relation is suggested by the following two-dimensional simulation of the compaction of initially uniformly displaced discs inside an annulus shown in Fig. 11. The beads are either slowly compacted by the outward motion of the inner boundary [Fig. 11(a)], or by the inward motion of the outer boundary [Fig. 11(b)]. The simulation is made using the soft sphere discrete element method code MercuryDPM [37], assuming a damped linear spring interaction between particles in the normal direction, and damped linear spring sliders in the tangential direction. The walls are modelled as rough, i.e., particles cannot rotate while in contact with the boundary. Shaded connections in Fig. 11 indicate contacts with more than double the average contact force. The figure suggests that the force chains, indicated by consecutive black connections, tend to align with the radial direction when the inner boundary moves outwards, and orthoradially (tangentially to the circle), if the beads are compacted by the inward motion of the outer boundary. This suggests that the average effective normal stress is higher in the tangential direction (compared to the radial stress) when the outer boundary moves inwards ($K_2 > 1$), and that the radial average effective stress is higher when the inner boundary move outwards ($K_2 < 1$), if we assume that the bulk part of the stress is mediated by force chains. The simulations are not meant to be a faithful representation of the compaction of the front, as the front is three dimensional. In addition, gravity is likely to affect how the beads in our experiments settle down, so we cannot use estimated values from the two-dimensional simulations directly. We assume, however, that the general

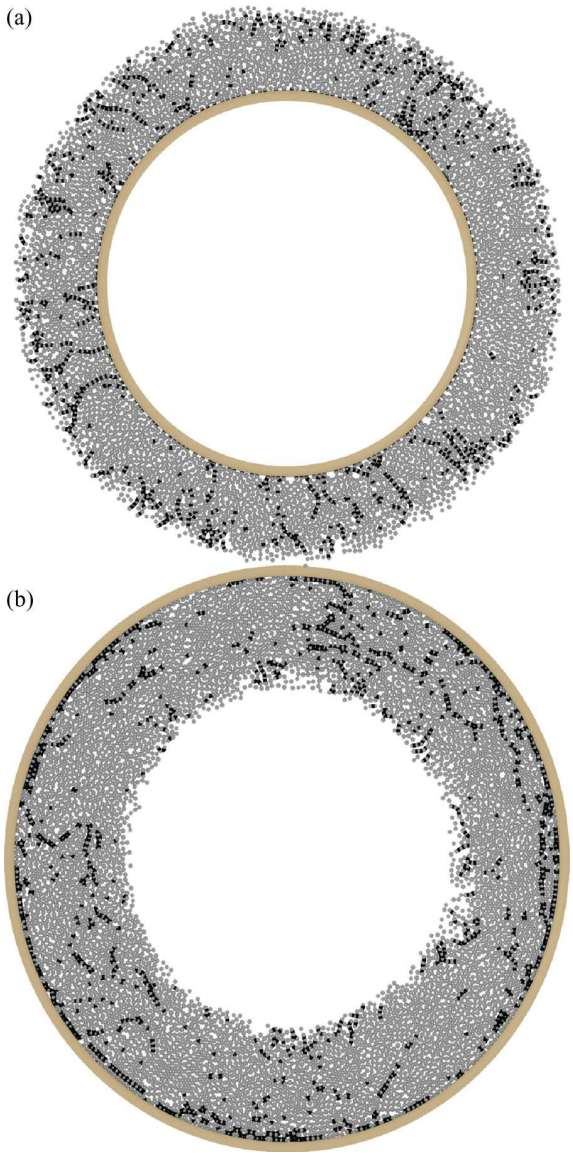

FIG. 11. (Color online) Compaction of beads in two dimensions. Black connections indicate contacts with more than double the average contact force. Contacts are overlaid for 50 consecutive time steps of the simulation. The beads are compacted as (a) the inner boundary moves outwards or as (b) the outer boundary slowly moves inwards. Note how the chains of contacts tend to orient radially in (a), which suggests that the average stress in the radial direction σ_{rr} is bigger than the stress in the orthoradial direction $\sigma_{\theta\theta}$, i.e., $K_2 < 1$. In contrast, the chains tend to orient orthoradially in (b), which suggests that $\sigma_{\theta\theta} > \sigma_{rr}$ and $K_2 > 1$.

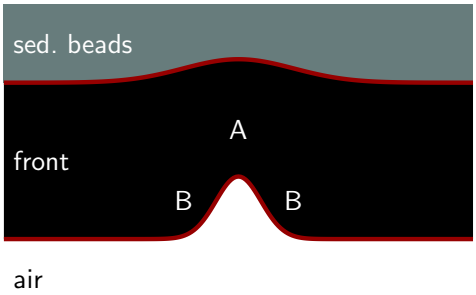

FIG. 12. (Color online) Schematic of the channeling of air through the front. Consider two regions of the front. A: The front adjacent to the tip of the channel is compacted as an interface segment of high curvature κ moves outwards (towards the sedimented beads). B: The front at the shoulders of the channel are compacted as the negatively curved interface moves outwards. Undulations along the interface are not shown in the figure.

direction of the force chains in the front, in the (r, θ) plane, is similar to that of the two-dimensional simulations (Fig. 11). We will therefore assume that K_2 is a decreasing function of κ.

This curvature dependence of K_2 may be of importance when the yield threshold [Eq. (16)] is applied to the interface of the channels which make their way through the front of a bubble, shown in Fig. 12. The channel configurations contain regions of high positive curvatures, region marked A in Fig. 12, and with low negative curvatures, region marked B in Fig. 12. If we assume that K_2 grows beyond 1 in the B region, and that K_2 takes a value below 1 in the A region, the yield stress of the front will behave qualitatively differently in the different regions, as shown in Fig. 6. The growing yield threshold for decreasing curvatures in region B [Fig. 6(b)] may therefore result in arching effects, and prevent the front from further deformation. Note that the channel growth is well beyond the presented linear stability analysis. It is hard to determine the experimental values of κ at interfaces which correspond to region B; it is possible that these configurations are mobile, and correspond to $\kappa L < -1$ (see Fig. 4). In that case, we may need to modify the theoretical framework further. We leave the details of these mechanisms for future work.

In summary, we have derived a natural extension to the yield stress model of bead fronts, used to simulate frictional finger structures [15,22]. The new expression for the yield pressure threshold [Eq. (16)] incorporates the tangential stress component, and the geometrical modifications due to the curvature of the front, by assuming a linear relationship between the radial and the tangential stress, $\sigma_{vv} = K_2\sigma_{uu}$ (or $\sigma_{\theta\theta} = K_2\sigma_{rr}$ in cylindrical coordinates). These modifications are important for the bubble dynamics shown in Fig. 1, as κL takes values which cannot be neglected, in particular at the channels between the bubbles.

We have also presented a linear stability analysis for a straight front segment, based on the threshold criterion in Eq. (16). This linear stability analysis gives a closed form expression for the most unstable wave numbers in Eq. (32). The numerical values of the wavelengths agree with the wavelengths of the undulations seen along the interface of bubbles in experiments, for reasonable choices of parameters. In particular, the results are consistent with $0.8 < K_2 < 1$ (Fig. 10).

The theoretical results we have presented will be of importance for future attempts to simulate the bubble formation. The discretization scheme presented in Ref. [38] provides a natural framework for such a simulation. Such simulations may also need to take into account the K_2 dependence of the curvature, to faithfully represent the channeling through the front around the bubbles (Fig. 12). We suggest that this dependence can be determined from a three-dimensional bead simulation based on the discrete element method, similar to the two-dimensional example in Fig. 11.

ACKNOWLEDGMENTS

We thank E. Flekkøy and K. J. Måløy for fruitful discussions. J.A.E. acknowledges support from the Research Council of Norway (NFR) through the NFR Project No. 200041/S60, and from Campus France through the Eiffel Grant. B.M. acknowledges support from NFR Grant No. 213462/F20. B.S. acknowledges support from EPSRC Grant No. EP/L013177/1. R.T. acknowledges support from The European Union SEVENTH FRAMEWORK PROGRAMME for research, technological development, and demonstration under Grant Agreement No. 316889 FlowTrans. R.T. acknowledges additional support from the University of Oslo and Université de Strasbourg.

[1] G. Varas, J.-C. Géminard, and V. Vidal, Granular Matter **15**, 801 (2013).
[2] I. B. Belien, K. V. Cashman, and A. W. Rempel, Earth Planet. Sci. Lett. **297**, 133 (2010).
[3] L. Cueto-Felgueroso and R. Juanes, Phys. Rev. E **79**, 036301 (2009).
[4] M. Sahimi, Rev. Mod. Phys. **65**, 1393 (1993).
[5] B. Koppelman, A. Walker, and E. Woods, Shale gas extraction in the UK: A review of hydraulic fracturing 2012, The Royal Society, The Royal Academy of Engineering (unpublished).
[6] A. J. Cavanagh and R. S. Haszeldine, Int. J. Greenhouse Gas Control **21**, 101 (2014).
[7] C. Chevalier, A. Lindner, and E. Clement, Phys. Rev. Lett. **99**, 174501 (2007).
[8] O. Johnsen, R. Toussaint, K. J. Måløy, and E. G. Flekkøy, Phys. Rev. E **74**, 011301 (2006).
[9] Ø. Johnsen, C. Chevalier, A. Lindner, R. Toussaint, E. Clément, K. Måløy, E. Flekkøy, and J. Schmittbuhl, Phys. Rev. E **78**, 051302 (2008).
[10] X. Cheng, L. Xu, A. Patterson, H. M. Jaeger, and S. R. Nagel, Nat. Phys. **4**, 234 (2008).
[11] X.-Z. Kong, W. Kinzelbach, and F. Stauffer, Chem. Eng. Sci. **65**, 4652 (2010).
[12] A. Debacker, S. Makarchuk, D. Lootens, and P. Hébraud, Phys. Rev. Lett. **113**, 028301 (2014).
[13] M. Niebling, R. Toussaint, E. G. Flekkøy, and K. J. Måløy, Phys. Rev. E **86**, 061315 (2012).

[14] R. Niebling, R. Toussaint, E. G. Flekkøy, and Måløy, Rev. Cub. Fis. **29**, 1E66 (2012).
[15] B. Sandnes, E. G. Flekkøy, H. A. Knudsen, K. J. Måløy, and H. See, Nat. Commun. **2**, 288 (2011).
[16] C. Chevalier, A. Lindner, M. Leroux, and E. Clement, J. Non-Newtonian Fluid Mech. **158**, 63 (2009).
[17] R. Holtzman, M. L. Szulczewski, and R. Juanes, Phys. Rev. Lett. **108**, 264504 (2012).
[18] A. Islam, S. Chevalier, I. B. Salem, Y. Bernabe, R. Juanes, and M. Sassi, Int. J. Multiphase Flow **58**, 279 (2014).
[19] H. Shin and J. C. Santamarina, Earth Planet. Sci. Lett. **299**, 180 (2010).
[20] B. Sandnes, E. G. Flekkøy, K. J. Måløy, and J. A. Eriksen, Rev. Cub. Fis. **29**, 1E23 (2012).
[21] B. Sandnes, H. A. Knudsen, K. J. Måløy, and E. G. Flekkøy, Phys. Rev. Lett. **99**, 038001 (2007).
[22] H. A. Knudsen, B. Sandnes, E. G. Flekkøy, and K. J. Måløy, Phys. Rev. E **77**, 021301 (2008).
[23] J. A. Eriksen, R. Toussaint, E. G. Flekkøy, K. J. Måløy, and B. Sandnes (unpublished).
[24] B. Sandnes, E. Flekkøy, and K. Måløy, Eur. Phys. J.: Spec. Top. **204**, 19 (2012).
[25] See Supplemental Material at http://link.aps.org/supplemental/10.1103/PhysRevE.91.052204 for videos of the bubble behavior.
[26] H. Janssen, Z VER DTSCH ING **39**, 1045 (1895).
[27] The Janssen parameter was denoted by κ in Refs. [21,22]. We use here κ for the curvature and K_1 for the Janssen parameter.
[28] R. M. Nedderman, *Statics and Kinematics of Granular Materials* (Cambridge University Press, Cambridge, England, 2005).
[29] P.-G. de Gennes, Rev. Mod. Phys. **71**, S374 (1999).
[30] G. Ovarlez, C. Fond, and E. Clément, Phys. Rev. E **67**, 060302 (2003).
[31] W. M. Lai, D. H. Rubin, D. Rubin, and E. Krempl, *Introduction to Continuum Mechanics, Forth edition*, (Butterworth-Heinemann, Burlington, MA, 2009).
[32] J.-P. Bouchaud, M. Cates, and P. Claudin, J. Phys. I **5**, 639 (1995).
[33] J. Wittmer, M. Cates, and P. Claudin, J. Phys. I **7**, 39 (1997).
[34] J. P. Wittmer, P. Claudin, M. E. Cates, and J.-P. Bouchaud, Nature (London) **382**, 336 (1996).
[35] B. Marks, B. Sandnes, G. Dumazer, J. A. Eriksen, and K. J. Måløy, arXiv:1505.04054.
[36] R. M. Corless, G. H. Gonnet, D. E. Hare, D. J. Jeffrey, and D. E. Knuth, Adv. Comput. Math. **5**, 329 (1996).
[37] A. Thornton, T. Weinhart, S. Luding, and O. Bokhove, Int. J. Mod. Phys. C **23**, 1240014 (2012).
[38] J. A. Eriksen, R. Toussaint, E. G. Flekkøy, K. J. Måløy, and B. Sandnes (unpublished).

Working paper:
Phase field approach to viscous fronts

Jon Alm Eriksen*[1], Luis Cueto-Felgueroso[2] and Ruben Juanes[3]

[1]Department of Physics, University of Oslo, P. O. Box 1048 Blindern, N-0316 Oslo, Norway

[2]Department of Civil Engineering: Hydraulics, Energy and the Environment, Universidad Politécnica de Madrid

[3]Department of Civil and Environmental Engineering, Massachusetts Institute of Technology

June 8, 2015

Abstract

When air displaces a suspension with a high solid fraction of sufficiently large particles, the particles tend to form a compacted but fluid region along the air/suspension interface: A viscous front. Moreover, the front grows as the air moves further into the suspension. As the effective viscosity of the suspension increases with the particle density, the viscous damping in the front dominates the energy dissipation in the system. What sets this system apart from conventional two-phase flow dynamics, in the context of the Saffman-Taylor instability, is that the viscous region (the front) is confined to a layer at the interface. The dynamics of this system are governed by the interplay between effective viscosity of the front, the growth of the front due to the accumulation of beads and the surface tension of the air/front interface. We propose here a simplified phase field model which allows for simulating the dynamics of the system.

This working paper introduces a phase field model which allows for numerical simulations of a growing viscous front. The current form of the paper does not contain a complete numerical study. A preliminary numerical simulation is, however, presented at the end. This simulation illustrates the feasibility of the model. We will introduce the system in Section 1 and gradually construct the numerical scheme in Section 2. The final phase field model equations are presented Section 2.3.

*jonaerik@fys.uio.no

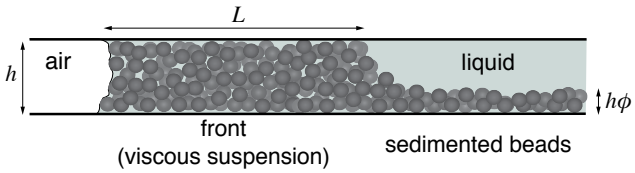

Figure 1: Side view of the Hele-Shaw cell. Air is forced in on the left, and beads accumulate along the air-liquid interface, forming a layer of beads adjacent to the interface referred to as the *front*. The front behaves effectively as a viscous suspension when the driving pressure is sufficiently high. The thickness of the front is denoted by L. The cell gap is h and ϕ is the initial fraction of sedimented beads relative to the cell gap.

1 Introduction

The Saffman-Taylor instability at the interface between immiscible fluids in a Hele-Shaw cell, and the formation of viscous fingers [1], have been studied extensively [2, 3, 4]. However, there is a growing interest in studying Hele-Shaw flow in settings where the fluids also interact with mobile particles. These systems have both industrial applications, as well as academical interests. A range of new flow morphologies have been observed, including destabilized viscous fingers [5], granular compaction and decompaction fingers [6, 7, 8], channeling [9, 10], irreversible poromechanical deformation [11] and various types of fracturing behavior [12, 13, 14, 15].

In particular, when air displaces a liquid phase which contains a layer of sedimented beads, a diverse set of dynamical modes have been identified [16]. This system is known to display labyrinth patterns of frictional fingers [17, 18] and intermittent bubble formations [16, 19, 20]. A common feature of these patterns is that the moving interface of the invading air bulldozes up the beads and forms a compacted layer of beads adjacent to the interface, which fills the whole cell gap (see Fig 1). This layer will in the following be referred to as the *front*. In the case of frictional fingers, and the intermittent bubbles, the beads in the front jam between the cell plates and the dynamics depend on static friction stresses [18, 20]. However, when the system is driven fast enough to prevent the beads from relaxing into a static configuration, a large but confined section of the front is fluidized and continuously evolving. During the evolution, the moving front behaves effectively as a viscous dense suspension. The high viscosity contrast between the air and the fluidized front allows for viscous fingers of air to penetrate the front. These structures are eventually frozen in the cell, when sections of the front settle down in a static configuration. This behavior is shown in the phase diagram presented in Fig. 5a in Ref. [16], under the label "viscous fronts". The dynamics of these structures motivate the study of viscous fingers into a confined layer which grows due to the accumulation of new beads.

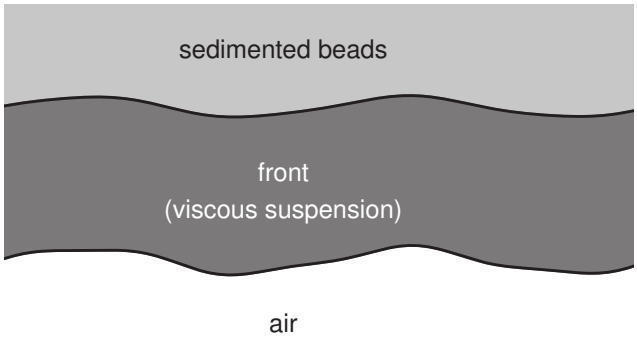

Figure 2: Schematic of the front as seen from above (compare to the side view in Fig. 1). The front moves upwards into the region of sedimented beads. It accumulates beads as it moves, i.e. the thickness of the front is growing in time. Surface forces act at the air/front interface, while there are no surface forces at the separation between the front and the sedimented region.

This paper aims to develop a numerical model for simulating the dynamics of a viscous front, i.e. the viscous layer in Fig. 1, as it is displaced by an air phase. A top view of the system in question is illustrated in Fig. 2. We will assume that the viscous dissipation is confined to the front, and ignore the pressure drop in the air phase, and in the liquid phase outside the front. We also assume that the interface stresses can be described by an effective surface tension parameter γ. This assumption is discussed in detail and validated elsewhere [18, 21]. The presence of an effective surface tension implies a surface stress which scales with the mean curvature of the interface. We will ignore the out-of-plane component of this mean curvature; the out-of-plane curvature is assumed to be constant along the in-plane direction of the interface, such that the associated surface stress is constant and unimportant for the dynamics. This assumption will leave out effects induced by variations in the wetting properties of the cell plates [2, 22]. We will here focus on the effects induced by the geometry of the front, and choose to keep the boundary conditions of the interface simple, in line with the original stability analysis of the Saffman-Taylor instability [1, 23].

The air/front interface is unstable as air is forced into the cell. The instability is similar to the original Saffman-Taylor instability [1] for a single interface, where the phases extend infinitely on both sides of the interface. The difference here is that the front is confined in a layer which grows due to the accumulation of new beads, as shown in Fig. 2. The growth rate of the front is dependent on the amount of beads in the sedimented layer. We will neglect variations in the packing fraction, and assume that the sedimented beads, and the suspension have roughly the same density of beads. We can therefore characterize the initial conditions of the cell by an effective normalized filling fraction of beads, ϕ, which is defined as the height of the sedimented beads relative to the height of the cell h, as show in Fig. 1. We will approximate the transition region between the

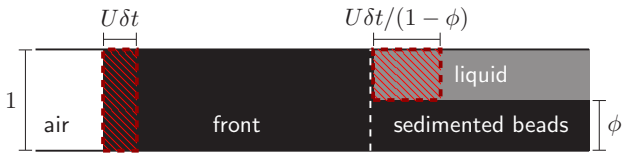

Figure 3: Schematic side view of the cell, compare this to Fig. 1. Mass conservation, for a flat interface, implies that the rectangles marked in red are equal in size. The initial fraction of sedimented beads relative to the cell gap is denoted by ϕ.

front and the sedimented region as a sharp boundary, as indicated with a white dashed line in Fig. 3. Note that if a flat interface moves a distance $U\delta t$ towards the suspension, the separation between the front and the region of sedimented beads moves $U\delta t/(1-\phi)$, as shown in Fig. 3. The rate of displacement of this outer boundary line is captured by a multiplicative factor $1/(1-\phi)$.

2 Towards a numerical method

Representing interfaces numerically is a common problem when dealing with multiple phases. One approach is to describe the different phases by indicator fields. That is, scalar fields $c(x)$, where x is a position vector, such that $c(x) = 1$ far from the interface where the phase is present, $c(x) = 0$ far from the interface where the phase is absent, and such that $c(x)$ transits smoothly between 0 and 1 at the interface. The interface can be identified as the transition region around the $c(x) = 0.5$ contour. This approach is therefore also referred to as a diffusive-interface method. An advantage of this method is that complex interfaces can be described by simulating a scalar field on a simple regular grid. This strategy is the starting point of a class of models–the phase field models–which proves to be especially suitable for describing two-phase Darcy flow, as described below.

We will in the following construct a simplified phase field model which builds on Refs. [24] and [25]; the approach taken here will, however, be considerably simpler. A detailed discussion of general phase field models can be found in Ref. [26]. An overview of the relevant literature for the application of phase field models in the context of Hele-Shaw flow, can be found in the introduction of Ref. [25].

The approach taken here, is to modify the Cahn-Hilliard equation [27], such that it also accounts for driving of the fluid due to a pressure field. It is therefore instructive to first review the Cahn-Hilliard equation and some of its properties. The material in the following subsection builds heavily on [26].

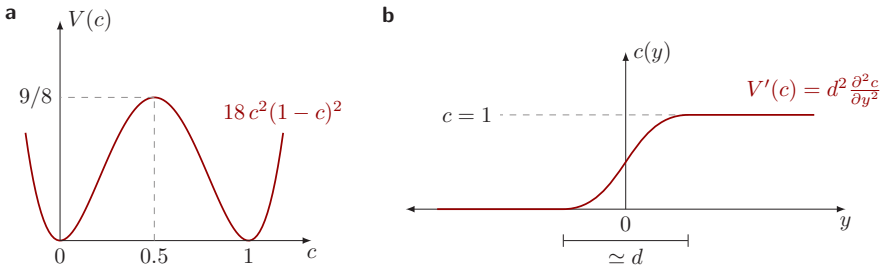

Figure 4: (a) The potential $V(c)$ defined in Eq. (2). (b) A schematic illustration of the steady state configuration $c = c(y)$. The configuration obeys Eq. (8).

2.1 Cahn-Hilliard equation

Let c be an indicator field for one of the phases and consider the following free energy functional[1],

$$F[c] = \epsilon \int \mathrm{d}\Omega \left(\frac{d^2}{2} |\nabla c|^2 + V(c) \right), \tag{1}$$

where the integral runs over the whole spacial domain, ϵ is a characteristic energy density and d is a length scale parameter. The function, $V(c)$, is here a non-dimensional double well potential taking its minima at $c = 0, 1$. We will consider a potential with the form,

$$V(c) = 18c^2(c-1)^2. \tag{2}$$

The shape of this potential is shown in Fig. 6a. The reason for the numerical value in the prefactor becomes apparent when we identify the surface tension bellow. Note that the uniform fields $c(x) = 1$ and $c(x) = 0$ are fields which minimize Eq. (1). When we look for a field configuration which is constrained by having a finite volume of $c(x)$ and minimize the free energy functional, we have to balance the gradient term, which penalizes sharp phase variations, to the potential energy term which penalizes the transition region at the interface. The free energy serves to construct a chemical potential, μ, by the functional derivative of the free energy,

$$\mu = -\frac{\delta F}{\delta c} = \nabla^2 c - \frac{\partial V}{\partial c}. \tag{3}$$

In deriving the Cahn-Hilliard equation, one assumes that this chemical potential drives a gradient flux,

$$J = -M\nabla\mu, \tag{4}$$

[1]We will in the following assume that the reader is familiar with functionals and functional derivatives; an introduction to those concepts can be found in any textbook dealing with Lagrangian mechanics, or in Ref. [28].

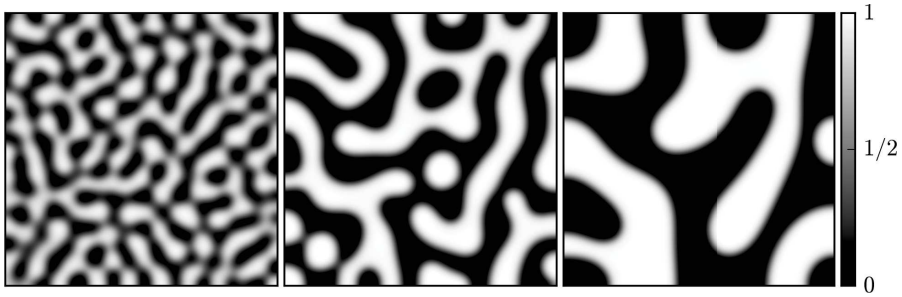

Figure 5: Time frames showing the qualitative behavior of a two-dimensional phase field, c, under the evolution of Cahn-Hilliard equation [Eq. (5)]. Time increases from left to right. The minimization of the free energy, which is confined to the transition region between the phases, is causing the coarsening of the domains, while conserving the total volume of the phases. The simulation is done on a 512×512 grid using the FiPy finite volume solver [29].

where M is a mobility. We will assume here that this mobility is constant in space. This will simplify the governing equations considerably, and will make them easier to solve numerically. Plugging the flux into the conservation equation for c, i.e. $\partial_t c + \nabla \cdot J = 0$, yields the Cahn-Hilliard equation,

$$\frac{\partial c}{\partial t} = M\nabla \cdot \left[\nabla \frac{\delta F}{\delta c}\right] = M\epsilon \left(\nabla \cdot [g(c)\nabla c] - d^2 \nabla^4 c\right), \tag{5}$$

where the last equality follows from our particular choice of double well potential [Eq. (2)], and,

$$g(c) = 36(1 - 6c(1 - c)). \tag{6}$$

The evolution of this equation is illustrated in Fig. 5.

We can show, using Eq. (5) and integration by parts, that the free energy functional is decreasing during the evolution,

$$\frac{\mathrm{d}F}{\mathrm{d}t} = \int \mathrm{d}\Omega \frac{\delta F}{\delta c}\frac{\partial c}{\partial t} = \int \mathrm{d}\Omega \frac{\delta F}{\delta c}\nabla \cdot \left[M\nabla \frac{\delta F}{\delta c}\right] = -\int \mathrm{d}\Omega M \left|\nabla \frac{\delta F}{\delta c}\right|^2 \leq 0, \tag{7}$$

where we assume that the chemical potential is zero along the boundary of the domain. The dynamics are driving the field configuration towards a lower free energy. Analogous to the concept of free energies in thermodynamics, this motivates why we called F a "free energy" in the first place.

We can also identify the surface tension, γ, in the model. Consider a steady state of a planar separation between the phases. Let y be a coordinate which runs perpendicular to this interface, such that the interface is located at $y = 0$, as shown in Fig. 6b. Let also $c \to 1$ as $y \to \infty$, and similarly $c \to 0$ as $y \to -\infty$.

We have that the steady state condition is $\delta F/\delta c = 0$ or $d^2\partial_y^2 c = V'(c)$, which upon integration yields,

$$V(c) = \frac{d^2}{2}\left(\frac{\partial c}{\partial y}\right)^2. \tag{8}$$

We can use this to derive an expression for the free energy per unit interface, i.e. the surface tension,

$$\begin{aligned}\gamma &= \epsilon\int_{-\infty}^{\infty}\mathrm{d}y\left[\frac{d^2}{2}\left(\frac{\partial c}{\partial y}\right)^2 + V(c)\right] \overset{*}{=} \epsilon d^2\int_{-\infty}^{\infty}\left(\frac{\partial c}{\partial y}\right)^2\mathrm{d}y \\ &= \epsilon d^2\int_0^1\frac{\partial c}{\partial y}\,\mathrm{d}c \overset{*}{=} \epsilon d\int_0^1\sqrt{2V(c)}\,\mathrm{d}c = \epsilon d\int_0^1 6c(1-c)\,\mathrm{d}c = \epsilon d.\end{aligned} \tag{9}$$

Eq. (8) is used after both equality signs marked with an asterix ($\overset{*}{=}$). The last integral yields 1, which is why we introduced the factor of 18 in Eq. (2). The derivation above tells us two things. First, the surface tension of an interface is simply $\gamma = \epsilon d$. This result is consistent with respect to units for two dimensional fluids, as the energy density takes the dimensions energy/length^2. Second, it also tells us that the characteristic width of the transition is of length d, which is useful to know when we want to discretize the system.

2.2 A phase field model for two-phase flow

The flow of a viscous incompressible fluid in a horizontally oriented Hele-Shaw cell is well described by Darcy's law,

$$U = -\lambda\nabla p, \tag{10}$$

together with the incompressibility condition,

$$0 = \nabla\cdot U, \tag{11}$$

where U is the height averaged fluid velocity, λ is the mobility and p is the pressure field. One can show that the mobility of the Hele-Shaw flow is given by $\lambda = h^2/(12\eta)$, where h is the gap of the Hele-Shaw cell and η is the viscosity (μ is reserved for the chemical potential). The two-phase flow we consider here has a viscosity contrast between the phases. The viscosity η, and the mobility λ, is therefore varying in space $\lambda = \lambda(x)$.

Equation (10) takes the same form as Eq. (4), i.e. they are both describing gradient flows. In the case of Eq. (4) the chemical potential is driving the flux which leads to the separation of the phases, whereas in the case of Eq. (10), the pressure acts as a potential which drives the flow.

This observation invites us to treat the pressure and the chemical potential on equal footing. Assume that the flux J of the indicator field c can be described

by the sum of two terms: an advective part cU given by the Darcy velocity U, and a diffusive part $M\nabla\mu$, which is driven by the chemical potential in Eq. (3) and regulates the interface. Using this in the conservation equation, yields,

$$\partial_t c = \nabla \cdot [c\lambda \nabla p] + M\nabla^2 \mu. \tag{12}$$

Note that, due to symmetry, the inverse field should evolve as,

$$\partial_t (1-c) = \nabla \cdot [(1-c)\lambda \nabla p] - M\nabla^2 \mu, \tag{13}$$

where the gradient of the chemical potential comes here with an opposite sign in comparison to Eq. (12). This can we verified by substituting $c \to 1-c$ in Eq. (3). Adding Eqs. (12) and (13) together gives the incompressibility condition,

$$0 = \nabla \cdot [\lambda \nabla p]\,. \tag{14}$$

Note also that the mobility λ should be a function of the indicator field $\lambda = \lambda(c)$. We will for now assume that c is the phase of low viscosity. The mobility is proportional to the reciprocal of the viscosity, $\lambda \sim 1/\eta$, i.e. c has the maximal mobility $\lambda_{\max}$. We will take the mobility to be given by

$$\lambda(c) = \lambda_{\min} e^{\ln(K)c}, \tag{15}$$

where K is the mobility ratio $\lambda_{\max}/\lambda_{\min}$. This function will be easy to handle numerically and agrees in the limiting values $\eta(1) = \lambda_{\max}$ and $\eta(0) = \lambda_{\min}$.

Taken together, we can write out the model for the two-phase flow of immiscible fluids, in a non-dimensional form,

$$\partial_t c = \nabla \cdot [c\lambda(c)\nabla p] + \frac{1}{\mathrm{Ca}}(\nabla \cdot [g(c)\nabla c] - d^2\nabla^4 c), \tag{16}$$

$$0 = \nabla \cdot [\lambda(c)\nabla p]\,, \tag{17}$$

$$\text{where} \quad g(c) = 36(1 - 6c(1-c)), \tag{18}$$

$$\text{and} \quad \lambda(c) = e^{\ln(K)c}. \tag{19}$$

We have implicitly here introduced the modified capillary number Ca. The two dimensionless numbers are given by,

$$\mathrm{Ca} = \frac{UW^2(\eta_{\min}^{-1} - \eta_{\max}^{-1})}{\gamma M}, \tag{20}$$

$$K = \frac{\eta_{\max}}{\eta_{\min}}, \tag{21}$$

where W is the characteristic width of the system, and U the characteristic speed. It is not obvious how to compare the modified capillary number to an experimental setup, as we do not know the mobility M. A way to overcome this problem is to calibrate the system, for the specific experimental setup in question.

2.3 A model for the viscous front

We need only to slightly modify the model described in the previous section, to account for dynamics of the viscous front. The front is confined between two interfaces, the air/suspension interface and the approximate interface between the front and the sedimented beads. We will represent the front by combining two indicator fields c_1 and c_2, as shown in Fig. 6. The phase indicated by c_1 corresponds to the air phase, while c_2 corresponds to air and the front. We can therefore identify the front as $\Delta = c_2(1-c_1)$. Both fields are driven by a pressure gradient. The separation between the front and the sedimented region moves at an increased rate due to the accumulation of new beads. This increased rate is captured by a multiplicative factor $1/(1-\phi)$ in the flux of the c_2 field, where ϕ is the height of the sedimented layer relative to the cell gap. The air/front interface is subject to surface tension, which is described by a surface flux, as described in the previous subsections. There is no such surface tension at the separation between the front and the sedimented beads, and consequently no such flux in the conservation equation for c_2.

We can finally write the governing equations which couples the evolution of c_1, c_2 and p, as

$$\partial_t c_1 = \nabla \cdot [c_1 \lambda(\Delta) \nabla p] + \frac{1}{\mathrm{Ca}} (\nabla \cdot [g(c_1) \nabla c_1] - d^2 \nabla^4 c_1), \tag{22}$$

$$\partial_t c_2 = \frac{1}{1-\phi} \nabla \cdot [c_2 \lambda(\Delta) \nabla p] \tag{23}$$

$$0 = \nabla \cdot [\lambda(\Delta) \nabla p] \,, \tag{24}$$

where,

$$g(c) = 36(1 - 6c(1-c)), \tag{25}$$

$$\lambda(\Delta) = \exp[\ln(K)(1-\Delta)], \tag{26}$$

$$\text{and} \quad \Delta = c_2(1-c_1). \tag{27}$$

A preliminary numerical simulation of these equations is shown in Fig. 7. The figure demonstrates the feasibility of the model. The fields c_1, c_1 and p, are discretized on a regular grid (256×768). A subset of the grid points along the x coordinates are shown in Fig. 7. A mirror image of the phases are included in the simulation (not shown in Fig. 7), in order to construct periodic boundary conditions. We can therefore utilize the discrete Fourier transformation to effectively calculate the spacial derivatives. The pressure field is solved by a finite volume scheme with a two-point flux, and the time integration is done by a third-order explicit Runge-Kutta scheme. A thorough numerical study, which investigates this numerical scheme for the range of relevant parameters, will be left for future work.

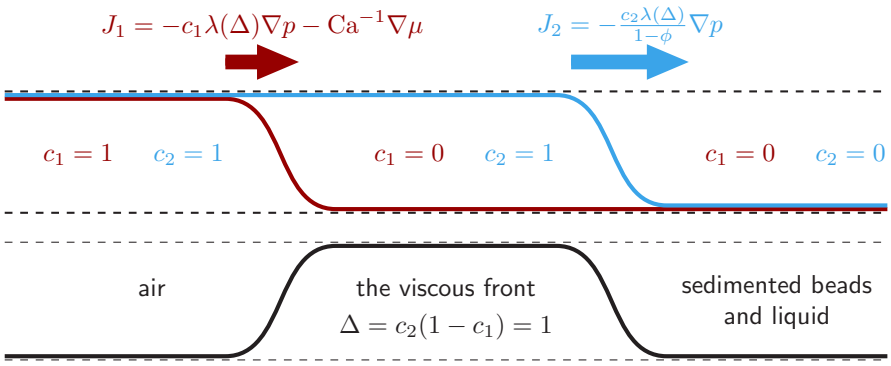

Figure 6: Schematic illustration of how the difference between the indicator fields, c_2 and c_1, represent the viscous region in a cross section of the front. We neglect the viscosity in the air phase, and in the region of the sedimented beads and the liquid. The front, which acts as a dense suspension, is dominating in terms of viscosity, i.e. this region has the lowest mobility, $\eta_{\min}$. Both the air phase and the region of liquid/sedimented beads are approximated by $\lambda_{\max}$.

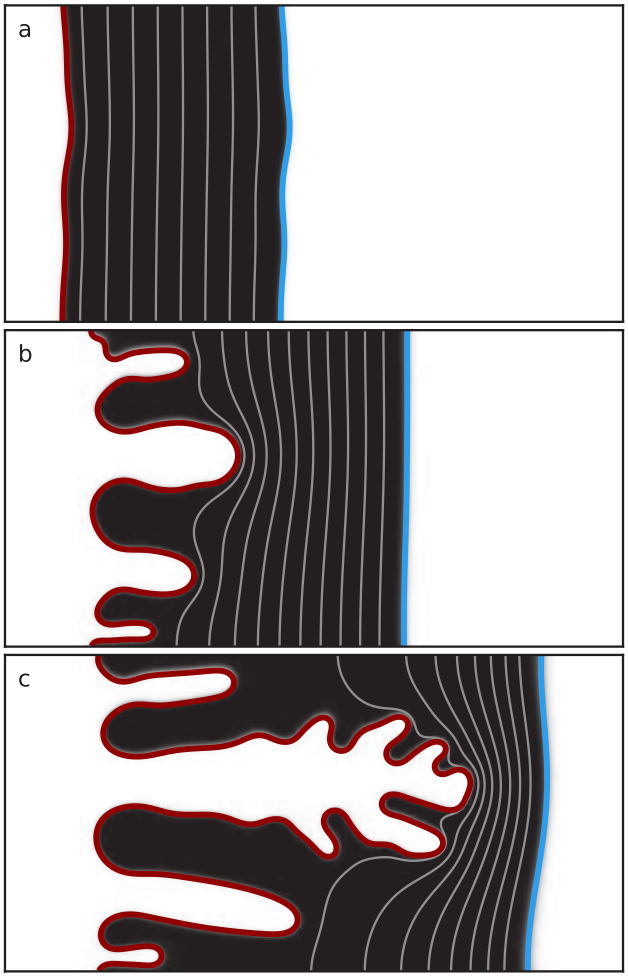

Figure 7: Time frames of a simulation of Eqs. (22)–(27). The red and blue lines correspond to 1/2 contour of c_1 and c_2 respectively. The black region corresponds to the viscous front, $\Delta = (1 - c_1)c_2$ (compare with Fig. 6). The frames correspond to initial configurations (a), intermediate time after 1000 time steps (b), and final time after 2100 time steps (c); each step lasts for $\delta t = 2.5 \times 10^{-3}$ time units. The height of each frame (in the y direction) takes 10 units of length. The thin gray lines correspond to contours of the pressure field and are decreasing from left to right. The white region on the left and the right correspond to air and fluid/sedimented beads respectively. Other parameters are $d = 0.36$, $\mathrm{Ca} = 300$, $K = 400$ and $\phi = 0.25$.

References

[1] P. G. Saffman and G. Taylor, "The penetration of a fluid into a porous medium or hele-shaw cell containing a more viscous liquid," *Proceedings of the Royal Society of London. Series A, Mathematical and Physical Sciences*, vol. 245, no. 1242, pp. pp. 312–329, 1958.

[2] D. Bensimon, L. P. Kadanoff, S. Liang, B. I. Shraiman, and C. Tang, "Viscous flows in two dimensions," *Rev. Mod. Phys.*, vol. 58, pp. 977–999, Oct 1986.

[3] G. M. Homsy, "Viscous fingering in porous media," *Annual Review of Fluid Mechanics*, vol. 19, no. 1, pp. 271–311, 1987.

[4] J. Casademunt, "Viscous fingering as a paradigm of interfacial pattern formation: Recent results and new challenges," *Chaos: An Interdisciplinary Journal of Nonlinear Science*, vol. 14, no. 3, pp. 809–824, 2004.

[5] C. Chevalier, A. Lindner, and E. Clement, "Destabilization of a Saffman–Taylor fingerlike pattern in a granular suspension," *Physical review letters*, vol. 99, no. 17, p. 174501, 2007.

[6] X. Cheng, L. Xu, A. Patterson, H. M. Jaeger, and S. R. Nagel, "Towards the zero-surface-tension limit in granular fingering instability," *Nature Physics*, vol. 4, no. 3, pp. 234–237, 2008.

[7] Ø. Johnsen, R. Toussaint, K. J. Måløy, and E. G. Flekkøy, "Pattern formation during air injection into granular materials confined in a circular hele-shaw cell," *Phys. Rev. E*, vol. 74, p. 011301, Jul 2006.

[8] Ø. Johnsen, C. Chevalier, A. Lindner, R. Toussaint, E. Clément, K. Måløy, E. Flekkøy, and J. Schmittbuhl, "Decompaction and fluidization of a saturated and confined granular medium by injection of a viscous liquid or gas," *Physical Review E*, vol. 78, no. 5, p. 051302, 2008.

[9] G. Varas, J.-C. Géminard, and V. Vidal, "Air invasion in a granular layer immersed in a fluid: Morphology and dynamics," *Granular Matter*, vol. 15, no. 6, pp. 801–810, 2013.

[10] X.-Z. Kong, W. Kinzelbach, and F. Stauffer, "Morphodynamics during air injection into water-saturated movable spherical granulates," *Chemical Engineering Science*, vol. 65, no. 16, pp. 4652–4660, 2010.

[11] C. W. MacMinn, E. R. Dufresne, and J. S. Wettlaufer, "Fluid-driven deformation of a soft granular material," *Phys. Rev. X*, vol. 5, p. 011020, Feb 2015.

[12] C. Chevalier, A. Lindner, M. Leroux, and E. Clement, "Morphodynamics during air injection into a confined granular suspension," *Journal of Non-Newtonian Fluid Mechanics*, vol. 158, no. 1, pp. 63–72, 2009.

[13] M. J. Niebling, R. Toussaint, E. G. Flekkøy, and K. J. Måløy, "Dynamic aerofracture of dense granular packings," *Physical Review E*, vol. 86, p. 061315, 2012.

[14] A. Islam, S. Chevalier, I. B. Salem, Y. Bernabe, R. Juanes, and M. Sassi, "Characterization of the crossover from capillary invasion to viscous fingering to fracturing during drainage in a vertical 2d porous medium," *International Journal of Multiphase Flow*, vol. 58, pp. 279–291, 2014.

[15] R. Holtzman, M. L. Szulczewski, and R. Juanes, "Capillary fracturing in granular media," *Phys. Rev. Lett.*, vol. 108, p. 264504, Jun 2012.

[16] B. Sandnes, E. G. Flekkøy, H. A. Knudsen, K. J. Måløy, and H. See, "Patterns and flow in frictional fluid dynamics," *Nat. Commun.*, vol. 2, p. 288, 2011.

[17] B. Sandnes, H. A. Knudsen, K. J. Måløy, and E. G. Flekkøy, "Labyrinth patterns in confined granular-fluid systems," *Phys. Rev. Lett.*, vol. 99, p. 038001, Jul 2007.

[18] H. A. Knudsen, B. Sandnes, E. G. Flekkøy, and K. J. Måløy, "Granular labyrinth structures in confined geometries," *Phys. Rev. E*, vol. 77, p. 021301, Feb 2008.

[19] B. Sandnes, E. Flekkøy, and K. Måløy, "Stick slip displacement of confined granular mixtures: Bubble expansion," *The European Physical Journal Special Topics*, vol. 204, no. 1, pp. 19–25, 2012.

[20] J. A. Eriksen, R. Toussaint, E. G. Flekkøy, K. J. Måløy, and B. Sandnes, "Model of finger formation at the tip of propagating dykes," *in preparation*, vol. 0, p. 0, 2015.

[21] J. A. Eriksen, R. Toussaint, E. G. Flekkøy, K. J. Måløy, and B. Sandnes, "Simulating frictional fingers," *in preparation*, vol. 0, p. 0, 2015.

[22] T. Maxworthy, "Experimental study of interface instability in a hele-shaw cell," *Physical Review A*, vol. 39, no. 11, p. 5863, 1989.

[23] L. Paterson, "Radial fingering in a hele shaw cell," *Journal of Fluid Mechanics*, vol. 113, pp. 513–529, 1981.

[24] L. Cueto-Felgueroso and R. Juanes, "Macroscopic phase-field model of partial wetting: Bubbles in a capillary tube," *Phys. Rev. Lett.*, vol. 108, p. 144502, Apr 2012.

[25] L. Cueto-Felgueroso and R. Juanes, "A phase-field model of two-phase hele-shaw flow," *Journal of Fluid Mechanics*, vol. 758, pp. 522–552, 2014.

[26] A. J. Bray, "Theory of phase-ordering kinetics," *Advances in Physics*, vol. 51, no. 2, pp. 481–587, 2002.

[27] J. W. Cahn and J. E. Hilliard, "Free energy of a nonuniform system. i. interfacial free energy," *The Journal of Chemical Physics*, vol. 28, no. 2, pp. 258–267, 1958.

[28] I. M. Gel'fand and S. V. Fomin, *Calculus of variations*. Courier Corporation, 2000.

[29] J. E. Guyer, D. Wheeler, and J. A. Warren, "FiPy: Partial Differential Equations with Python," *Computing in Science & Engineering*, vol. 11, no. 3, pp. 6–15, 2009.